Aus dem Institut für Anatomie und Zellbiologie

der Universität Würzburg

Vorstand: Professor Dr. med. Süleyman Ergün

Ultrastructural analysis of biogenesis and release of endothelial extracellular vesicles

Inauguraldissertation

zur Erlangung der Doktorwürde der

Medizinischen Fakultät

der

Julius-Maximilians-Universität Würzburg

vorgelegt von

Clara Dorothea Elsner

aus Passau

Würzburg, Dezember 2021

This document is licensed under the Creative Commons Attribution-NoDerivatives 4.0 International License (CC BY-ND 4.0):
http://creativecommons.org/licenses/by-nd/4.0 This CC license does not apply to third party material (attributed to another source) in this publication.

Referentin:	**Priv.-Doz. Dr. Nicole Wagner**
Korreferent:	**Univ.-Prof. Dr. rer. nat. Andreas Friebe**
Dekan:	**Prof. Dr. Matthias Frosch**

Tag der mündlichen Prüfung: **30.09.2022**

Die Promovendin ist Ärztin.

Contents

1. Introduction

1.1 Cardiovascular disease and its connection to extracellular vesicles

1.1.1 Epidemiology and aetiology of CVD

Cardiovascular disease (CVD) represents the leading cause of mortality worldwide. As announced by the German Federal Statistics Office, in 2017, about 37% of all deaths in Germany (approximately 344.500) were due to cardiovascular diseases like chronic ischemic heart disease, acute myocardial infarction or stroke. Furthermore, CVDs lead to considerable consequences for the individual and represent the biggest contributor to medical expenses in society. The German Federal Statistics Office published that in 2015, 46,4 billion euros or approximately 13,7% of the overall medical expenses amounting to 338,2 billion euros were caused by this group of disease [1, 2].

The major cause of CVD is atherosclerosis, a chronic inflammatory condition that can be converted into an acute clinical event by plaque rupture and thrombosis [3]. It is initiated and driven by a continuous damage of the vascular endothelium leading to the development of endothelial dysfunction [4]. Endothelial cell dysfunction encompasses disruptions in several functions of the vascular endothelium [5].

In physiological conditions, the barrier function of arterial endothelium is strictly regulated, and vascular permeability is limited. In pathological conditions such as atherosclerosis, the barrier function is weakened while the vascular permeability is significantly increased [6]. This is due to pathological structural changes in intercellular junctions between endothelial cells as well as loss of the proper regulation of the barrier function [6].

Atherosclerosis is also associated with a reduced bioavailability of nitric oxide (NO) produced from endothelial NO synthase [7]. Endothelial-derived NO is critical for the relaxation of vascular smooth muscle and the inhibition of platelet adhesion or aggregation. It further inhibits leukocyte adhesion to the endothelium

as well as smooth muscle cell migration and proliferation [8]. Therefore, a reduced availability of NO – amongst other things – leads to the pathophysiological manifestations of endothelial cell dysfunction.

Hypercholesterolemia and hypertension, two major risk factors for atherosclerosis, cause endothelial activation. Once a specific plasma level of cholesterol-rich very low-density lipoprotein (VLDL) and LDL is reached, the capacity for their elimination is exceeded and the lipoproteins are retained in the artery wall. They are subsequently modified either through enzymatic attack or non-enzymatic oxidation in the intima layer, leading to the release of bioactive phospholipids. This presents a proinflammatory step that activates endothelial cells [9].

As a result, expression of adhesion molecules like vascular cell adhesion molecule-1 (VCAM-1) is induced followed by subsequent destabilization of the endothelial barrier. This attracts leukocytes (including T-lymphocytes and monocytes) and increases their attachment to the endothelium [9]. They subsequently penetrate the endothelial layer to infiltrate the arterial intima, where they initiate proatherogenic inflammation. In addition to leukocytes, platelets also adhere to activated endothelial cells [9]. Monocytes differentiate into macrophages and internalize modified lipoproteins to become foam cells, which are a sure symbol of fatty streaks (lesions that precede the atherosclerotic plaques). Various chemokines and growth factors emitted by activated endothelium and macrophages then induce the proliferation of smooth muscle cells and the production of extracellular matrix components within the intima leading to the development of a fibromuscular plaque [10]. The initial lesion develops into so called atheromas or atherosclerotic plaques. They consist of a cap of smooth muscle cells and a collagen-rich matrix and a lipid-rich, necrotic core made of oxidized lipoproteins, cholesterol crystals and cellular debris [10]. Inflammatory cells such as activated macrophages and T-cells infiltrate throughout the lesion and further modulate the endothelial proinflammatory phenotype [9].

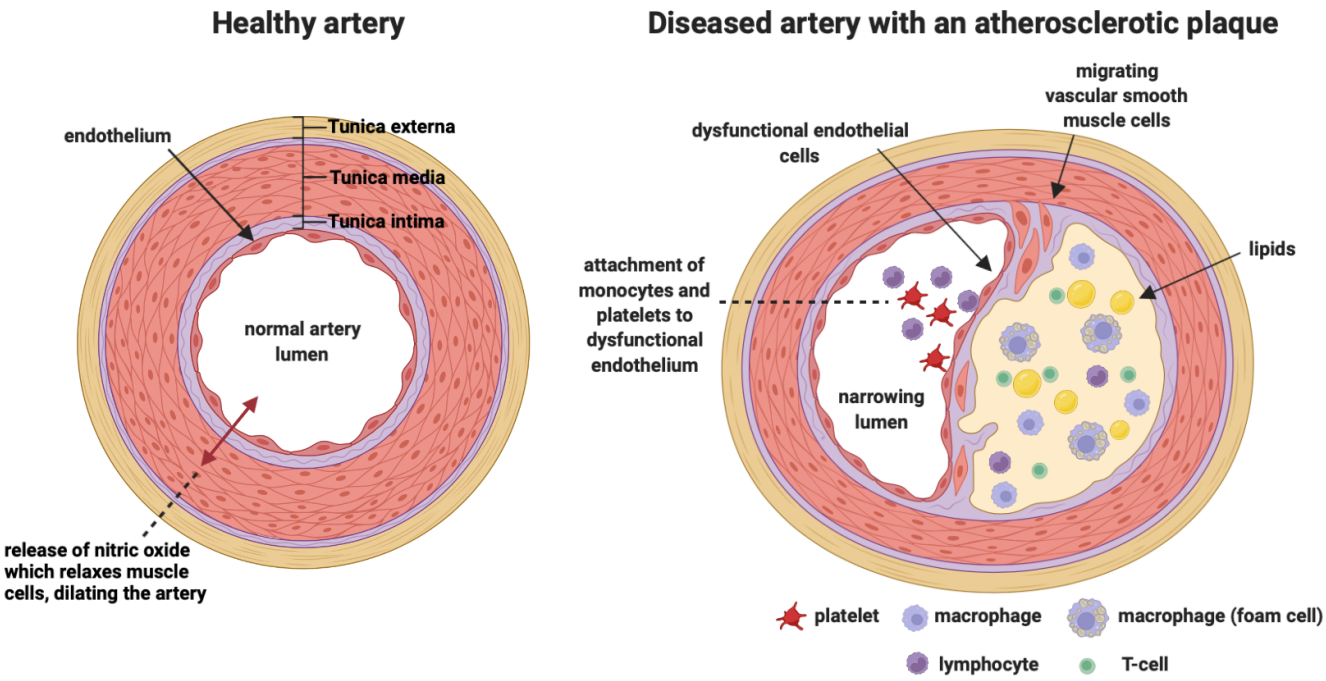

Fig. 1 Schematic representation of the contrast between a healthy artery and an artery with atherosclerotic modifications in cross-section. Image created with BioRender.com [9].

Given its important role throughout this complex series of events, endothelial cell dysfunction represents an essential condition for atherosclerotic cardiovascular disease.

1.1.2 Extracellular vesicles – biomarkers and contributors to the development of CVD

Extracellular vesicles (EVs) are diverse types of phospholipid bilayer-enclosed vesicles which are secreted into the extracellular environment by several cell types under physiological as well as pathological conditions [10]. EVs can be found in all observed extracellular fluids including blood, urine, saliva, breast milk, ascites or cerebrospinal fluid [11-13].

They have been shown to contain not only surface receptors, membrane proteins and lipids originated from the plasma membrane, but also nucleic acids (DNA and RNA) including mRNAs, microRNAs (miRNAs), small-interfering RNAs (siRNAs), small nucleolar RNA and long non-coding RNAs (lncRNAs) from the

intracellular environment [14]. These functional contents depend on the cellular origin and the particular (patho)physiological condition at the time of EV packaging and secretion [15]. As the EVs can carry and transfer a multitude of bioactive molecules, surface receptors, and genetic information, their role as important players in intercellular communication, signal transduction, and immune regulation – locally and over long distances – is now widely acknowledged [15, 16]. There are three main types of EVs that have been characterized based on their different biogenesis and mechanisms of release: Microvesicles (MVs), exosomes and apoptic bodies [17].

Patients with CVDs associated with a systemic endothelial damage, such as atherosclerosis, show significantly increased levels of circulating endothelial cell-derived EVs as well as different molecular compositions of EVs in their bloodstream [18, 19]. A large 2014 cohort study of 844 patients with a history of CVD revealed a positive correlation between circulating endothelial MV levels and the presence of cardiometabolic risk factors such as triglyceride levels, hypertension and metabolic syndrome [20]. This suggests that EVs can be utilized to identify or detect pathological conditions during the development of CVD as well as monitor them, thus presenting potential diagnostic and prognostic biomarkers for CVDs and cardiovascular mortality [21, 22].

However, recent studies have shown that EVs are not only just a marker of vascular integrity but function as relevant contributors to the development of atherosclerosis and subsequent complications [23]. They do so by promoting initial lesion formation, intravascular calcifications, plaque progression, and thrombus formation after rupture [24]. Especially endothelial EVs seem to have a significant impact on inflammatory processes and endothelial homeostasis [25]. Endothelial EVs have been found to accumulate in atherosclerotic plaques, where they affect major biological pathways, including inflammation, proliferation, thrombosis, calcification, and vasoactive responses [26].

To further highlight the important role of endothelial EVs in CVD, some examples of the underlying mechanism of their contribution to the disease development are given in the following.

1.1.3 Examples for the contribution of endothelial EVs to CVD

Rautou et al. stated in 2011 that circulating endothelial and leukocyte MVs induce endothelial dysfunction via an impaired endothelial NO bioavailability. They do so by inhibiting the endothelial NO synthase and therefore decreasing NO synthesis or by stimulating free radical generation [24].

Furthermore, endothelial MVs promote the expression of different adhesion molecules on endothelial cells and therefore, a subsequent destabilization of the endothelial barrier. They for instance contain the intercellular adhesion molecule (ICAM)-1 and transfer it to the endothelial cell membrane, enabling the recruitment of monocytes into the atherosclerotic plaques [24].

At last, MVs also play a role in plaque rupture and the following thrombus formation - a dangerous event, which can cause ischemia and infarction. Locally released plaque MVs expose phosphatidylserine (PS) and tissue factor at their surface, awarding the MVs a high procoagulant activity [24].

Moreover, it is known that endothelial dysfunction can be activated by an increase of oxidized LDL (the main atherogenic class of lipoprotein) and homocysteine serum levels, two factors some authors call “the most important risk factors for atherosclerosis” [27]. Zhan et al. published in 2009 that heightened oxidized-LDL and homocystein levels induce the release of HSP70 (Heat Shock Protein 70)-containing exosomes from cultured aortic endothelial cells. The high level of extracellular HSP70 activates monocytes, leading to their subsequent adhesion to endothelial cells – a pro-inflammatory and proatherogenic procedure in the early steps of atherosclerosis [28].

Furthermore, Zakharova et al. could show in 2007 that activated T-lymphocytes emit exosomes, whose outer membrane leaflets exhibit cholesterol and phosphatidylserine (PS). Monocytes can internalize these exosomes and, in the following, increase the production of tumor necrosis factor (TNF)-α, a proinflammatory cytokine. The T-cell derived exosomes also induce cholesterol accumulation and therefore atherogenesis within an atherosclerotic plaque [29].

Finally, Gao et al. demonstrated in 2016 that dendritic cells release exosomes, which activate endothelial cells via the TNF-α-mediated NF-κB pathway and therefore accelerate endothelial inflammation and the progression of atherosclerosis [30].

1.2 Classification of EVs

Microvesicles (MVs) (elsewhere in the literature also referred to as microparticles, ectosomes or shedding vesicles) are surrounded by a phospholipid bilayer and produced by the direct outward budding and subsequent shedding of the plasma membrane. The MVs' size typically ranges from 100 nanometers (nm) to 1 micrometer (µm) [31]. Therefore, they are usually larger than exosomes, but vesicle size alone is not a certain distinguishing feature.

The primary distinction between MVs and exosomes is the mechanism of biogenesis and their respective composition [16]. As they originate from the plasma membrane, MVs tend to be enriched in proteins such as integrins, glycoprotein Ib, selectins, flotillin-2, metalloproteinases and lipids (phosphatidylserine, cholesterol) [32, 33]. Typical for MVs is the abundant expression of phosphatidylserine on the outer membrane leaflet and antigens representative of their parent cells [34].

Exosomes are nanovesicles also surrounded by a phospholipid bilayer and of 30–100 nm in size [35]. Exosomes are a product of the endocytic pathway as they are formed from endosomal compartments called multivesicular bodies (MVBs) [36]. To generate exosomes, the membrane of MVBs invaginates inward to form so called intraluminal vesicles (ILVs) [33]. Through fusion of the MVBs with the plasma membrane, the ILVs are released into the extracellular environment and are given the name exosomes [35].

Besides their characteristic morphology, they can be identified through their unique protein and lipid composition. As the exosomes derive from endosomes, they all contain membrane transport and fusion proteins (Rab, GTPases, Annexins, flotillin), tetraspanins (including CD9, CD63, CD81, CD82), heat shock

proteins (Hsc70, Hsp90) and proteins that are involved in MVB biogenesis, for example the components of the endosomal sorting complex required for transport (ESCRT) complex ALIX or tumor susceptibility gene 101 [37, 38]. Lipids typically found in exosomes include cholesterol, ceramide and other sphingolipids, and phosphoglycerides (e.g. phosphatidylinositol, phosphatidylserine, phosphatidyl choline, phosphatidylethanolamine) [39].

Apoptotic bodies are EVs released specifically by cells undergoing apoptosis and arise from indiscriminate surface blebbing [40]. A major difference to other cell-derived vesicles is their size, which ranges from 50 nm–2 µm [31]. This class of EV will not be focused on in this thesis.

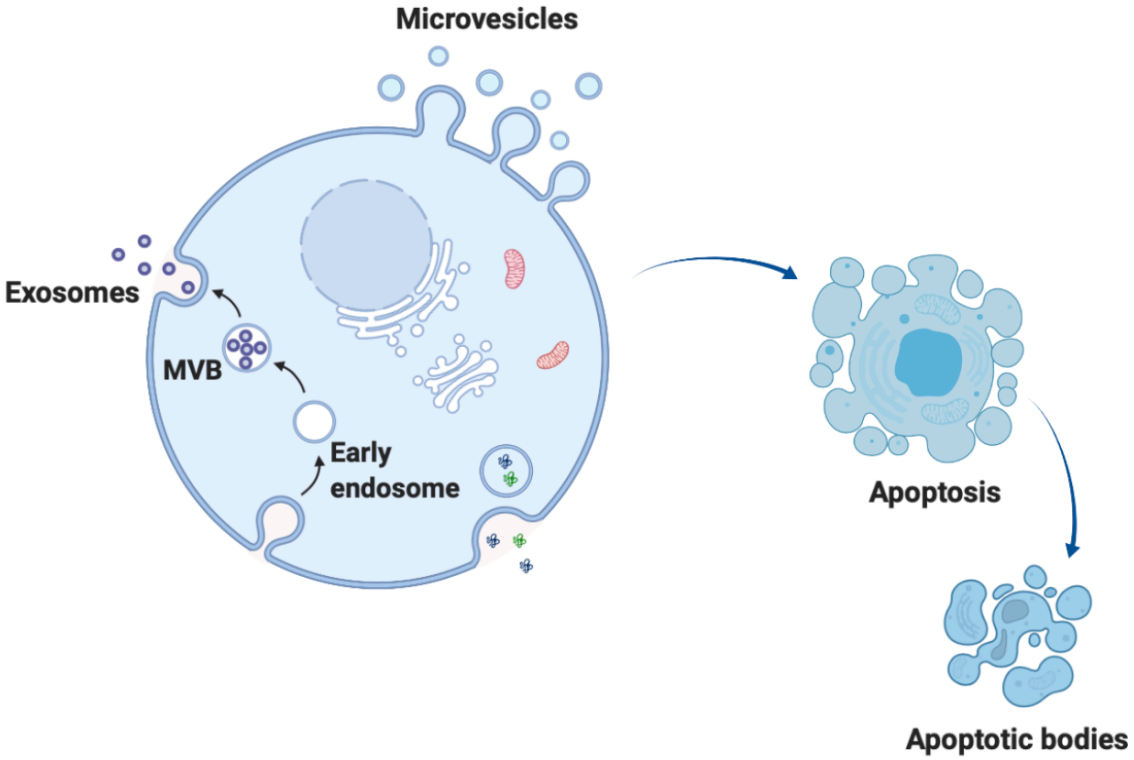

Fig. 2 Schematic representation of the different EV classes and their biogenesis. Image created with BioRender.com [9].

1.3 Microvesicles

1.3.1 Discovery and naming

In 1946, cell-derived vesicles were first discovered by Chargaff and West. They determined clotting times of plasma after centrifugation at different speeds, and could show that prolonged high-speed centrifugation significantly extended the clotting time of the supernatant [41]. Therefore, it was concluded that human plasma possesses a coagulation component that sediments into a small pellet during high-speed centrifugation. When this pellet containing “the clotting factor of which the plasma is deprived” was added to plasma, the clotting times shortened, indicating that cell-free plasma contains a subcellular factor that promotes the clotting of blood [41, 42]. Clarification came later in 1967 by Peter Wolf, who conducted ultracentrifugation, separation and coagulation tests on blood samples as well as electron microscopic analyses of plasma, serum, and other blood fractions. He identified the subcellular fraction as small vesicles with

a diameter between 20 and 50 nm and a density of 1.020 to 1.025 g/ml that were present in both plasma and serum, rich in phospholipids, and originated from platelets [43]. Wolf termed them “platelet dust” [43]. This name was subsequently replaced by the term microvesicles – however, throughout the scientific literature, other terms such as microparticles, shedding vesicles, oncosomes or ectosomes are also used [40, 44].

1.3.2 Microvesicle-producing cells

MVs have been predominantly characterized as products of platelets, red blood cells and endothelial cells [17] but it is now known that they are released from most cell types, including epithelial, fibroblast, hematopoietic, immune, tumor, placental and stem cells [45]. MVs could also be isolated from blood, ascites, pleural fluid, cerebrospinal fluid, postoperative drainage fluid and chyloid fluid [13].

1.3.3 Biogenesis

MVs originate through direct outward budding and fission of the plasma membrane [16]. The first step of MV formation is vertical trafficking of molecular cargo to the plasma membrane [40]. To allow outward budding, the plasma membrane undergoes several structural and molecular rearrangements at the site of MV origin. These are for instance an alteration in membrane curvature and rigidity – caused by a redistribution of proteins and phospholipids –, the disruption of cytoskeleton proteins organization or loss of the normal membrane phospholipid asymmetry [46]. The latter is regulated by aminophospholipid translocases which transfer phospholipids from one leaflet of the plasma membrane to the other [47]. Membrane budding and vesicle formation is induced by translocation of phosphatidylserine from the inner to the outer-membrane leaflet which causes physical bending of the membrane and restructuring of the underlying actin cytoskeleton [16, 48].

The completion of the budding process and the subsequent release of the MVs relies on the ATP-dependent contraction of cytoskeletal structures (actin-myosin interactions) [16].

Cargo contained within the MVs can be released into the extracellular milieu with various consequences for the surrounding environment. MVs can also interact with target cells via endocytosis, fusion, or activation of signaling pathways through receptor interactions [40, 49]. In general, the MV cargo consists of various proteins, lipids, and nucleic acids, but its exact composition depends largely on the specific biogenesis, cell type, and physiologic conditions from which the MVs originate [50].

1.3.4 Inducers of MV production

The production of MVs is modulated by various stimuli such as ligand encounter or cellular stress conditions, depending on the cell type. A common way of creating cellular stress in vitro is serum starvation [51]. Serum starvation is achieved by depleting the basal cultivation medium of all or most fetal bovine serum (FBS). FBS contains certain nutritional and macromolecular growth factors [51].

The various stimuli ultimately lead to increased intracellular calcium levels, inducing cytoskeleton reorganization, plasma membrane remodeling and vesicle shedding [52].

Cultured endothelial cells can release endothelial MVs after activation by a variety of mostly pro-inflammatory stimuli. Combes et al. first described the generation of MVs from human umbilical endothelial cells stimulated by TNF-α [53]. Inflammatory cytokines, bacterial lipopolysaccharides, reactive oxygen species, plasminogen activator inhibitor, thrombin, camptothecin, C-reactive protein and uremic toxins have also been shown to be able to induce endothelial MV generation in vitro [34, 54-57].

More recent studies have focused on in vivo mechanisms of MV release and have depicted sustained atheroprone low shear stress as an important stimulant [58].

Other known stimuli for MV release include the activation of P2X7 receptor (purinergic receptor P2X = ligand-gated ion channel 7) by ATP on monocytes and neutrophils, the thrombin receptor and Toll-like receptor 4 by lipopolysaccharide (LPS) on dendritic cells [55, 59, 60].

1.4 Exosomes

1.4.1 Discovery and naming

The term exosomes was first used in 1981 by Trams et al., who examined exfoliated vesicles from various normal and neoplastic cell lines that showed ecto-enzyme activity [61]. Further studies were conducted on vesicles isolated from rat reticulocytes [62] and sheep reticulocytes [63]. The authors followed the fate of the endocytosed transferrin receptor during its trafficking in the cell and subsequent externalization. They observed that the isolated vesicles contained the transferrin receptor, whereas cytosolic enzyme activities were not detectable. The authors deducted that “vesicle externalization could be a mechanism for shedding of specific membrane functions, which are known to diminish during maturation of reticulocytes to erythrocytes” [64]. It was then discovered that these vesicles are formed within MVBs and are being released when membranes of MVBs fuse with the plasma membrane. This was visualized by electron microscopy in 1985 [65]. The term exosome was then reinforced by Dr Rose Johnstone in 1987 because “the process seemed to be akin to reverse endocytosis, with internal vesicular contents released in contrast to external molecules internalized in membrane-bound structures” [66].

1.4.2 Exosome-producing cells

Exosomes can be secreted by numerous cell types, including stem cells, immune cells, hematopoietic cells, neuronal cells, cardiovascular cells and tumor cell lines [35, 37]. In addition, a significant number of exosomes was also found in most body fluids including blood, urine and ascites [11, 12].

1.4.3 Biogenesis

Exosomes are a product of the endocytic pathway [36]. First, endocytic vesicles form at the plasma membrane and fuse to form early endosomes, which then mature to late endosomes [67]. During this transformation, endocytic cargo fated to be exported is sorted into vesicles 30–100 nm in size, so called ILVs, that are formed by inward invagination of the endosomal membranes [36]. Given the presence of these multiple small vesicles, the late endosomes are also known as multi-vesicular bodies (MVBs) [37]. MVBs are present ubiquitously in all eukaryotic cells. They have first been described as such by Sotelo and Porter in 1959 [68].

Ubiquitination (the addition of the small protein ubiquitin to lysine residues of target proteins) seems to be the principal signal for cargo to be directed into the MVB pathway and sorted into ILVs [69]. Proteins that are sorted to the ILVs have three distinct fates.

The first possibility is the fusion of the MVB with lysosomes if the proteins are destined for degradation. The ILVs containing the proteins are delivered to the proteolytic lysosomal interior where they are degraded [70].

A second possibility is that proteins may be stored in MVBs temporarily. This was observed by Kleijmeer et al. in 2001 for major histocompatibility complex (MHC) class II proteins in immature dendritic cells (DCs). Upon pathogen-stimulation the MHC class II carrying internal vesicles were transferred to the MVB limiting membrane where they fused back with the membrane, thereby allowing subsequent transfer to the plasma membrane [71].

The third potential fate of vesicles within MVBs is the fusion of the MVB-limiting membrane with the plasma membrane resulting in the release of the ILVs into the extracellular environment as exosomes [70]. In the following, the latter option, which represents the biogenesis of exosomes, is presented in detail.

Sorting of EV cargo into the forming ILVs is a critical step in the biogenesis of MVBs. It is carried out by the endosomal sorting complexes required for transport (ESCRT), a multisubunit machinery [72]. Four distinct ESCRT protein complexes composed of approximately thirty proteins have been identified: ESCRT-0, -I, -II and -III; each fulfilling a clear task in MVB vesicle formation [73].

The ESCRT-0 complex initiates the MVB pathway by binding to ubiquitinated cargo and recruiting the ESCRT-I complex [74]. Each of the three early ESCRT complexes (ESCRT-0, -I, and -II) can interact with ubiquitinated cargo, and it can be concluded that they cooperate to sort the ubiquitinated proteins into the MVBs [74]. While cargo is collected, ESCRT-I together with ESCRT-II is responsible for membrane deformation into buds with sorted cargo [75]. The ESCRT-III complex is tasked with deubiquitinating cargo within the site of MVB vesicle formation, membrane budding and finally driving the vesicle scission [74].

However, several other ESCRT-independent pathways of MVB formation have been described: The tetraspanin CD63, which is crucial in the sorting process, accumulates in ILVs even in the absence of ESCRT function [76]. Other examples are the lipid metabolism enzymes neutral sphingomyelinase (nSMase) and phospholipase D2 that generate the lipids ceramide and phosphatidic acid, which then induce inward budding and formation of ILVs [77, 78].

The secretory MVBs now travel to the plasma membrane and fuse with the plasma membrane. The ILVs are then released into the extracellular space as exosomes [35].

1.4.4 Inducers of exosome release

Exosomes are released both constitutively and upon induction, depending on the cell type [75]. The secretion is regulated by various environmental changes, such as ligand encounter or stress conditions, and could be one of the means used by tissues to adapt to these changes [79]. Reticulocytes, T-cells, mastocytes and resting B-cells secrete detectable levels of exosomes only following the activation of a cell surface receptor [65, 80-82]. By contrast, Epstein-Barr virus-transformed B-cells, DCs, macrophages as well as most tumor cell lines constitutively secrete exosomes in vitro [83-85]. The activation of the p53 transcription factor as well as several intracellular proteins, such as diacylglycerol kinase α, have been proposed to have a role in the secretion of exosomes or exosome-like vesicles [86, 87]. However, these molecules are also involved in more general physiological processes.

1.5 Objective of this thesis

Establishing standardized and reproducible techniques for the in vitro study of EVs

Extracellular vesicles have been attracting widespread interest due to their role as potential biomarkers as well as therapeutic targets in cardiovascular disease. The last decades have seen a huge growth in the number of publications in this field and the cellular machinery controlling EV formation as well as the molecular composition of EVs have been extensively studied.

However, a crucial issue arising with this increasing number of publications is that the methods of EV generation, examination and isolation vary greatly between each work, which results in confusion regarding the interpretation and validity of the data. It is therefore essential to establish standardised and reproducible techniques for the in vitro study of EVs. To do so, we compared different study methods and give recommendations concerning their validity and usefulness – especially focusing on three topics: the microscopic approach for cell and vesicle

examination, the conditions of cell cultivation and the best approach to generate EVs with a high quantity and quality for further functional studies.

The following questions were of interest:

1. Which microscopic approach – light or different kinds of electron microscopic methods should be used for EV characterization? What are the advantages and possibilities / disadvantages and limitations of each method?

2. In which way does the commonly used stimulus serum starvation influence the cultivated cells? How does it affect their condition over time? Do they (morphologically) change and if so, how?

3. Which effect does serum starvation have on the quality and quantity of produced EVs?

4. How does the production of EVs change over time, regarding the number of produced vesicles and the fraction of different EV classes in comparison?

5. What is the best approach to generate as many EVs as possible for functional studies – while at the same time making sure they are of good quality?

Detailed ultrastructural analysis of the biogenesis and release of endothelial EVs

Even though the number of publications about EVs is constantly on the rise, there are still very few studies concerning the morphological processes underlying EV formation and release. But only when the procedure of EV formation and its effects on the producing cell are precisely understood, their function can be further examined. With this study, we therefore provide a detailed ultrastructural analysis of the biogenesis and release of endothelial EVs using light and electron microscopy.

Lastly, it is of great interest how cultivation under inflammatory stimulation influences EV production and composition. Results could lead the way to a better understanding of the role of EVs in intercellular communication in inflammatory diseases such as atherosclerosis. The following aspects were focused on:

1. Does EV production change when cells are subjected to inflammatory stimuli? If so, how?

2. Does this stimulation induce the expression of cell surface proteins known to be exposed during inflammatory processes in atherosclerosis?

3. If so, are these proteins being transferred to the EVs?

For this study, we cultured Myocardial Endothelial (MyEnd) and Aortic Endothelial (AoEnd) cells and subjected them to different stimuli: serum starvation and the inflammatory stimulus TNF-α.

A detailed morphological analysis of the endothelial cells and the EVs over time was then conducted applying and comparing different high-resolution microscopic methods such as Confocal Laser Scanning Microscopy (CLSM), Transmission Electron Microscopy (TEM), Scanning Electron Microscopy (SEM), Serial Block Face Scanning Electron Microscopy (SBF-SEM) and immunoelectron microscopic approaches.

The data presented in this thesis will serve as a fundamental prerequisite for a further understanding of EV biogenesis and possibly the development of new methods to manipulate EV formation, composition and secretion in the (patho)physiological context.

2. Materials and Methods

2.1 Materials

2.1.1 Cell culture

Immortalized MyEnd and AoEnd cell lines were generated from Wild-Type (WT) mice as previously described by Golenhofen et al. [88]. The cell lines used were as follows: MyEnds (generated from WT C57BL/6 mice; Charles River Laboratories, Wilmington, MA, USA) and AoEnds (generated from WT C57BL/6J mice; Charles River Laboratories, Wilmington, MA, USA).

2.1.2 Culture medium

500 ml Dulbecco's Modified Eagle Medium (DMEM)	Thermo Fisher Scientific, Waltham, MA, USA
50 ml fetal bovine serum (FBS)	Biochrom, Cambridge, United Kingdom
2,5 ml Penicillin/Streptomycin:	
Penicillin G sodium salt, 1477 U/mg	Sigma-Aldrich Chemie GmbH, St. Louis, MO, USA
Streptomycin sulfate salt, 720 U/mg	Sigma-Aldrich Chemie GmbH, St. Louis, MO, USA

2.1.3 Cultivation of MyEnd and AoEnd cells

MyEnd and AoEnd cells were cultivated on coverslips in an incubator (Heracell 240; Thermo Fisher Scientific, Waltham, MA, USA) at a constant 37°C and a 5% CO_2-content of the air in the previously described medium.

Experiments were commenced once the cells had reached the state of confluency. They were left to grow for an additional 7 days and then, the medium

was depleted of FBS, therefore exposing the MyEnd and AoEnd cells to serum starvation. The cells were cultivated in this serum-free medium for a total of 72 hours and samples were taken after 0 hours, 24 hours, 48 hours and 72 hours of cultivation.

For certain analyses, cells were simultaneously stimulated with recombinant human TNF-α (50 ng/ml; Thermo Fisher Scientific, Waltham, MA, USA), or Lipopolysaccharides (LPS L3129) from Escherichia coli O127:B8 (20 ng/ml; Sigma-Aldrich Chemie GmbH, St. Louis, MO, USA), which was added to the medium at the start of cell cultivation.

2.1.4 Materials for immunohistochemical staining

2.1.4.1 Buffers

1 X phosphate buffered saline (PBS) (preparation of 1 L adapted from Sambrook, Fritsch, and Maniatis [89]) pH 7,4	800 ml ddH_2O 8 g NaCl 0.2 g KCl 1.42 g Na_2HPO_4 0.24 g KH_2PO_4 HCl to adjust pH to 7,4

2.1.4.2 Fixation and contrasting reagents

4% paraformaldehyde (PFA) fixation solution	8 g paraformaldehyde solute in 150 ml at 58 °C a few drops 2 N NaOH till solution becomes clear 40 ml 10 x PBS diethylpyrocarbonate-treated-(DEPC-)H_2O ad 200 ml, adjust pH to 7.4, filter solution

2.1.4.3 Blocking reagents

0,5% bovine serum albumin (BSA)	Sigma-Aldrich Chemie GmbH, St. Louis, MO, USA

2.1.4.4 Antibodies

Tab.1 Overview of the primary and secondary antibodies used for immunohistochemical staining

primary antibody	manufacturer	dilution	secondary antibody	manufacturer	dilution
ICAM-1 (mouse)	abcam (Cambridge, UK)	1:100	Cy2-conjugated Goat Anti-Mouse IgG	dianova (Hamburg, Germany)	1:1000
VCAM-1 (rabbit)	Santa Cruz Biotechnology, Inc. (Dallas, TX, USA)	1:100	Cy2-conjugated Goat Anti-Rabbit IgG	dianova	1:1000
CD44 (rat)	BioLegend (San Diego, CA, USA)	1:100	Cy2-conjugated Goat Anti-Rat IgG	dianova	1:1000

2.1.4.5 Fluorescent stains

Wheat Germ Agglutinin, Texas Red-X conjugate	Thermo Fisher Scientific, Waltham, MA, USA
DAPI	F. Hoffmann-La Roche Ltd, Basel, Switzerland

2.1.5 Materials for Transmission Electron Microscopy (TEM)

All solutions needed for tissue-embedding for electron microscopic analyses were set up freshly before each experiment.

2.1.5.1 Buffers

1X phosphate buffered saline (PBS) (preparation of 1L adapted from Sambrook, Fritsch, and Maniatis [89]) pH 7,4	800 ml ddH_2O 8 g NaCl 0.2 g KCl 1.42 g Na_2HPO_4 0.24 g KH_2PO_4 HCl to adjust pH to 7,4

2.1.5.2 Fixation and contrasting reagents

2,5% glutaraldehyde fixation solution pH 7.2	2.5 % glutaraldehyde 50 mM cacodylate buffer 50 mM KCl 2.5 mM $MgCl_2$ dH_2O
1% osmium tetroxide (OsO4)	4% OsO4 (Electron Microscopy Sciences, Hatfield, PA, USA) 0,2 M cacodylate buffer ddH_2O
2% uranyl acetate (UA)	2% UA in 70% ethanol
0,2% lead citrate solution (prepared after Reynolds [90]) pH 12	1,33 g $Pb(NO_3)_2$ (lead nitrate) + 1,76 g sodium citrate x 2 H_2O dissolved in 30 ml ddH_2O

	8 ml 1 N NaOH volume filled up to 50 ml with ddH_2O

2.1.5.3 Dehydrating agents

ethanol	Sigma-Aldrich Chemie GmbH, St. Louis, MO, USA

2.1.5.4 Embedding media

propylene oxide	Electron Microscopy Sciences, Hatfield, PA, USA
Epon component A	24,3 g Epon 812 (glycidyl ether) 32,7 g Dodecenylsuccinic anhydride
Epon component B	22.5 g Epon 812 20.3 g Methyl nadic anhydride
Epon “hard”	3 parts Epon component A 7 parts Epon component B 1.5 Vol-% DMP-30
	All materials from Serva Electrophoresis GmbH, Heidelberg, Germany.

2.1.6 Materials for Immunoperoxidase (DAB) staining

2.1.6.1 Buffers

0,1 M PB pH 7,4	0.075 M Na_2HPO_4 0.025 M NaH_2PO_4
0,1 M Tris-Saline-Buffer (TSB) pH 7,6	0,01 M Trizma® base ($NH_2C(CH_2OH)_3$) (Sigma-Aldrich Chemie GmbH, St. Louis, MO, USA) 0,1 M NaCl ddH_2O
0,01 M PB pH 7,4	0.0075 M Na_2HPO_4 0.0025 M NaH_2PO_4

2.1.6.2 Fixation and contrasting reagents

4% paraformaldehyde (PFA) fixation solution	as described under 2.1.4.2
2% OsO_4 contrasting solution	500 µl 4% OsO_4 250 µl 2 M cacodylate buffer 250 µl ddH_2O

2.1.6.3 Blocking reagents

0,5% bovine serum albumin (BSA) in 0,1 M TSB	0,5 g 0,5% BSA 100 ml 0,1 M TSB
0,1% bovine serum albumin (BSA) in 0,1 M TSB	0,1 g 0,1% BSA 100 ml 0,1 M TSB

2.1.6.4 Antibodies

Tab.2 Overview of the primary and secondary antibody used for DAB staining

primary antibody	manufacturer	dilution	secondary antibody	manufacturer	dilution
CD44 (rat)	BioLegend (San Diego, CA)	1:500	biotinylated Goat Anti-Rat IgG	Linaris Biologische Produkte GmbH (Wertheim, Germany)	1:400

2.1.6.5 Immunoperoxidase detection system

Avidin-biotin (AB) complex	VECTASTAIN® ABC Kit (Vector Laboratories, Inc., Burlingame, CA, USA)

2.1.6.6 DAB staining

3,3′-Diaminobenzidinetetrahydrochloride (DAB) stock solution	0.075% in ddH_2O
DAB substrate working solution (adds up to 10 ml)	1665 µl 0,01 M PBS 3335 µl DAB stock solution 4960 µl ammonium chloride (8 mg/10 ml stock solution) 40 µl glucose oxidase (1 mg/ml in ddH_2O)
Ammonium nickel(II) sulfate stock solution (0,05 M in H_2O)	20 µl Serva Feinbiochemica GmbH & Co., Heidelberg, Germany

α-D-Glucose (13,3% in H_2O)	20 µl Serva Feinbiochemica GmbH & Co.

2.1.7 Materials for Scanning Electron Microscopy (SEM)

2.1.7.1 Buffers

Sörensen phosphate buffer pH 7,2	0,133 M KH_2PO_4 0,133 M Na_2HPO_4 ddH_2O

2.1.7.2 Fixation and contrasting reagents

6,25% GA solution	6,25% GA in 50 mM PB

2.1.7.3 Dehydrating agents

anhydrous acetone	Carl Roth GmbH, Karlsruhe, Germany

2.1.8 Materials for Serial Block-Face Scanning Electron Microscopy (SBF-SEM)

2.1.8.1 Buffers for preparation

0,15 M cacodylate buffer pH 7,4	50 mM cacodylate 50 mM KCl 2,5 mM $MgCl_2$ 2 mM $CaCl_2$

2.1.8.2 Fixation and contrasting reagents

2,5% GA immersion fixation	2,5% GA 2% PFA 2 mM $CaCl_2$ 0,15 M cacodylate buffer
1,5% potassium ferrocyanide solution	1,5 % potassium ferrocyanide 2% OsO_4 2 mM $CaCl_2$ 0,15 M cacodylate buffer
1% thiocarbohydrazide (TCH) solution	$(NH_2NH)_2CS$ (TCH) CO_2-free ddH_2O
2% OsO_4 solution	as described under 2.1.4.2
1% UA solution	1% UA in CO_2-free ddH_2O
0,6% lead aspartate solution (prepared after Walton [91])	0,03 M aspartic acid 0,02 M $Pb(NO_3)_2$ (lead nitrate) 1 M KOH

2.1.8.3 Dehydrating agents

ethanol	Sigma-Aldrich Chemie GmbH, St. Louis, MO, USA
acetone	Carl Roth GmbH, Karlsruhe, Germany

2.2 Methods

2.2.1 Immunohistochemistry

2.2.1.1 Standard fixation and staining procedure

Cells grown on coverslips were taken out of their culture medium, dipped in PBS a few times to wash off the medium and then immediately fixed with 4% PFA for 30 minutes. Specimens were washed in PBS for 3x5 minutes and incubated with WGA Texas Red-X conjugate (diluted 1:200 in PBS) for 30 minutes to visualize cell boundaries and EVs by binding to their glycocalyx. The second fluorescence stain DAPI (diluted 1:5000 in PBS) was added for 15 minutes to visualize cell nuclei by binding to their DNA. Afterwards, specimens were washed in PBS for 3x5 minutes. Cells had to be embedded in a medium without any auto-fluorescent ingredients and were therefore mounted on objective slides with the mounting medium Vectashield® (Linaris Biologische Produkte GmbH, Wertheim, Germany).

2.2.1.2 Use of specific cell surface markers

As described above, cells grown on coverslips were shortly dipped in PBS, then fixed with 4% PFA for 30 minutes and afterwards washed in PBS for 3x5 minutes. Next, the blocking reagent (0,5% BSA in PBS) was applied for 15 minutes. Subsequently, specimens were incubated with the primary antibodies ICAM-1 (mouse), VCAM-1 (rabbit) and CD44 (rat) diluted 1:100 in 0,5% BSA/PBS at 4 °C overnight. The next day, specimens were washed in PBS for 3x5 minutes, hereafter the fluorescence-labelled secondary antibodies Cy2-conjugated goat anti-mouse, Cy2-conjugated goat anti-rabbit and Cy2-conjugated goat anti-rat diluted 1:1000 in 0,5% BSA/PBS were applied for 60 minutes to detect antigen-antibody complexes. Finally, the fluorescence stains WGA Texas Red-X conjugate (diluted 1:200 in PBS) and DAPI (diluted 1:5000 in PBS) were applied for 30 minutes. Specimens were washed in PBS for 3x5 minutes and embedded on objective slides as described above.

2.2.2 Transmission Electron Microscopy (TEM)

All solutions were set up freshly before each experiment. Fixation and contrasting procedures as well as solution exchanges were performed under the vent and in closable glass vials due to toxicity of the reagents.

2.2.2.1 Fixation and contrasting procedures

The following steps of fixation and contrasting were performed at 4°C unless otherwise stated.

Cells grown on coverslips were taken out of their culture medium, dipped in PBS a few times to wash off the medium and immediately fixed with 0,15 M cacodylate buffer (pH 7,4) containing 2,5% glutaraldehyde and 2% formaldehyde at 4°C overnight. Next, they were washed with 0,01 M PBS for 4x10 minutes. For further fixation and staining of lipids, 1% OsO_4 (buffered with PBS) was applied for 60 minutes. Specimens were washed in PBS for 10 minutes, in double distilled water (ddH_2O) for another 3x10 minutes and then dehydrated in an ascending ethanol series of 30%, 50% and 70% for 10 minutes each. To enhance the contrast of lipids and proteins, specimens were incubated in a 2% UA solution for 60 minutes. This step must take place in a dark environment to avoid precipitation. Next, further dehydration took place with an ascending ethanol series of 70%, 80%, 90%, 96% and two times 100% ethanol solutions for 10 minutes each. The removal of water was terminated with an incubation with propylene oxide (PO) for 2x30 minutes.

To start the embedding procedure, the cell probes were incubated in a mixture of PO and Epon812 (1:1) for two hours followed by a second incubation step overnight. To allow the propylene oxide to evaporate over this time, the probes were left in an open glass container. The following day, the Epon-PO mixture was substituted with pure Epon812 and the specimens were incubated for 4 hours with an exchange of Epon812 after 2 hours. Cells were now embedded in gelatine BEEM®-cups filled with fresh epon. Special attention must be paid to this step,

as cells must face downwards to the capsule bottom and bubbles in the medium should be avoided. The cups are left open at room temperature for one hour, then closed with a gelatine cap and kept at 60°C for 48 hours to allow the epon to polymerise.

2.2.2.2 Ultrathin sections and contrasting

After epon polymerisation, part of the gelatine BEEM®-cups were removed, thus liberating the polymerized epon with the enclosed tissue. Ultrathin sections were cut with an ultramicrotome (Ultracut E, Reichert Jung, Germany) and collected on nickel grids (Plano GmbH, Wetzlar, Germany). The sections were now contrasted again with 2% UA and 0,2% lead citrate. First, both solutions were centrifuged at 13000U for 5 minutes before usage. Then, a piece of parafilm was put on a dark glass plate and one drop of 2% UA for each grid dripped on it. The grids with the ultrathin sections facing down were placed into the UA drops and covered up for 20 minutes. The grids were shortly washed; twice in 70% ethanol and three times in double distilled water. Next, the grids were incubated with a 0,2% lead citrate solution for 7 minutes. Lead citrate naturally reacts with CO_2 in the atmosphere to form lead carbonate precipitate, which appears as electron dense deposits on the grid [92]. Therefore, CO_2 contamination should be avoided. To absorb CO_2 from the air and keep the atmospheric CO_2 concentration to a minimum, fresh NaOH pellets (AppliChem GmbH, Darmstadt, Germany) were placed next to the grids and everything was covered with a lid. After this step, the grids were shortly washed in double distilled water. Finally, the grids were left to dry thoroughly and afterwards sorted into a grid box.

2.2.2.3 Immunoperoxidase (DAB) staining

For primary tissue fixation the specimens were immersed in freshly prepared 4% PFA fixation solution for 30 minutes at room temperature and washed with 0,1 M phosphate buffer (PB) for 3x10 minutes. Afterwards, they were washed in 0.1 M TSB for 2x10 minutes and blocked with 0.5 % BSA in 0,1 M TSB for 30 min at

room temperature. Specimens were washed in 0,1 M TSB for 2x10 minutes. At this point, one sample probe was taken away and put aside to act as a negative control. The remaining probes were then incubated with the primary antibody CD44 (rat) diluted 1:500 in 0,1% BSA/TSB overnight at 4°C and washed in 0,1 M TSB for 3x10 minutes the next day. Now the corresponding secondary antibody biotinylated goat anti-rat diluted 1:400 in 0,1% BSA/TSB was applied to all probes (including the negative control) for 90 minutes at room temperature. Meanwhile, the Avidin-biotin (AB) complex was prepared by mixing substance A and substance B from the VECTASTAIN® ABC Kit together 1:1 and adding 5 ml of 0,1 M TSB. The AB complex was then stored at room temperature in a dark environment for (at least) 30 minutes. Then, specimens were washed in 0,1 M TSB for 3x10 minutes and incubated with the prepared AB complex for 30 minutes. Afterwards, they were washed in 0,1 M TSB for 10 minutes and in 0,01 M PBS for 2x10 minutes.

The glucose oxidase-diaminobenzidine method described by Zaborsky and Heimer (1989, [93]) was carried out to reveal immunolabeling. The DAB substrate working solution was made up as follows: To 1665 µl of 0,01 M PB, 3335 µl of DAB stock solution (0.075% in ddH_2O), 4960 µl of ammonium chloride in PB (8 mg/10 ml stock solution) and 40 µl GOD (glucose oxidase, 1 mg/ml in ddH_2O) were added to a final volume of 10 ml and mixed. 20 µl of Ammonium nickel sulfate (0,05 M stock solution in ddH_2O) was added just prior to use, and specimens were incubated with the substrate working solution for 5 minutes at room temperature. To start the DAB-reaction, 20 µl D-Glucose (13.3% stock solution in ddH_2O) was added. The optimal length of DAB staining varies depending on the used tissue, so the development of the reaction was closely monitored to avoid overstaining. When staining was satisfactory (in this case after 7 minutes), the DAB reaction was stopped by replacing the substrate working solution with 0,01 M PB. Specimens were washed in PBS for 2x10 minutes and in 0,1 M PB for 10 minutes. Subsequently, they were fixed with 2% OsO_4 (buffered with 0,1 M PBS) for 60 minutes and afterwards shortly immersed in 0,1 M PB. The specimens were then put into fresh 0,1 M PB and stored at 4°C overnight. The next day, they were washed in fresh 0,1 M PB again for 5 minutes

and dehydrated in an ascending ethanol series using 30%, 50%, 70%, 90%, 96% and 2x100% ethanol solutions for 5 minutes each. Next, the probes were incubated with propylene oxide for 2x15 minutes. To start the embedding procedure, the cell probes were incubated in a mixture of PO and Epon812 (1:1) for two hours followed by a second incubation step overnight in an open glass container. The following day, the Epon-PO mixture was substituted with pure Epon812 and the specimens were incubated for 4 hours with an exchange of Epon812 after 2 hours. At last, the cells were embedded in Epon812 as previously described and kept at 60°C for 48 hours.

2.2.3 Scanning Electron Microscopy (SEM)

The preparation of the cell probes that were analysed with a scanning electron microscope consisted of fixation, dehydration, critical point drying and sputtering.

2.2.3.1 Fixation and dehydration

To ensure proper fixation, the probes were incubated with a 6,5% GA solution at 4°C overnight and the next day washed in Sörensen phosphate buffer for 5x5 minutes. Next, they were dehydrated in an ascending acetone series using 30%, 50%, 70%, 90% and 5x100% (the last two times anhydrous acetone is used) acetone solutions for 10 minutes each.

2.2.3.2 Surface rendering

To reduce artefacts that occur during the air drying of biological structures, specimens were dried with a critical point dryer (CPD 030, Bal-Tec AG, Balzers, Liechtenstein).

The drying procedure was conducted as indicated by the manufacturer. The pressure chamber of the critical point dryer was filled up to ¾ with 100% anhydrous acetone. The fixated and dehydrated specimens were transferred to

drying cages, which were placed into the acetone, making sure the acetone reached the upper edge of the cages. The pressure chamber was closed and cooled down to approximately 10 °C. Once that temperature was reached, CO_2 as a transition agent was administered. Step by step, all acetone was replaced by liquid CO_2. Once the exchange was complete, the chamber was heated to the critical point (at this specific temperature and pressure the gas and liquid phases of the transition agent are indistinguishable [94]), which is approximately 31.1 °C and 73 atmospheres for CO_2 [94]. Now, the transition agent could slowly be released as a gas, and the artefacts associated with air drying were minimized.

Lastly, the dried specimens were processed with a high-vacuum sputter coating device (SCD 005, Bal-Tec AG). This procedure minimizes damage to specimens by electron ”bombarding” and improves topographical contrast for improved imaging by SEM [94]. The specimens were secured on the scanning electron microscope stages and inserted centrally into the sputter coater. The device then coated them with a 20 nm thick layer of gold. The preparations for SEM were therefore completed and the specimens were stored in a desiccator until being examined.

2.2.4 Serial Block-Face Scanning Electron Microscopy (SBF-SEM)

All ddH_2O used in the following steps was boiled freshly right before the start of the procedures to get rid of CO_2 and then left to cool down to room temperature. The fixating and contrasting solutions were set up freshly as well.

Specimens were fixed with a 2,5% GA immersion fixation for 3 hours on ice and afterwards washed for 5x3 minutes in 0,15 M cacodylate buffer, also on ice. Subsequently, the specimens were incubated in 1,5% potassium ferrocyanide solution on ice for 60 minutes and afterwards washed with ddH_2O at room temperature for 5x5 minutes. Next, they were incubated in 1% TCH solution for 25 minutes at room temperature and afterwards washed with ddH_2O for 5x5 minutes at room temperature. Subsequently, the specimens were incubated in 2% osmium tetroxide in ddH_2O for 30 minutes at room temperature and

afterwards washed in ddH_2O for 5x5 minutes at room temperature. Lastly, they were incubated in 1% aqueous UA at 4° overnight. The next day, the specimens were first washed for 3x3 minutes in ddH_2O at room temperature and then for 2x3 minutes in ddH_2O, this time at 60°C, to prepare the tissue for the lead aspartate. Now the specimens were incubated in *en bloc* Walton's lead aspartate staining solution (Walton, 1979 [91]) and placed in a 60°C oven for 30 minutes. Afterwards, they were left to cool down to room temperature (20-23°C) for about 5 minutes. Next, the specimens were washed in ddH_2O for 5x5 minutes at room temperature and then dehydrated using ice-cold solutions of freshly prepared 30%, 50%, 70%, 90%, 100%, 100% ethanol (anhydrous), 100% acetone (anhydrous) for 10 minutes each. Subsequently, they were submerged in ice-cold 100% acetone for 2x10 minutes, then left for 10 minutes at room temperature. During this time, Epon812 was prepared and the resin was mixed thoroughly. The embedding process was started by placing the specimens into 25% Epon:acetone for 2 hours, then into 50% Epon:acetone for 2 hours and lastly 75% Epon:acetone for 2 hours. Subsequently, they were placed in 100% Epon overnight. The next day, specimens were placed into fresh Epon for 2 hours before finally being embedded as previously described and kept at 60°C for 48 hours for resin polymerization. The resin embedded cell probes were then mounted on aluminium pins (Gatan Inc., Pleasanton, CA, USA). The blocks were precision trimmed with a glass knife to expose the cells. Silver paint (Gatan Inc.) was used to coat the edges of the tissue block to reduce charging during imaging using the variable pressure mode.

2.2.5 Image Acquisition

2.2.5.1 Confocal microscopy

Specimens with immunohistochemical staining were analysed with the inverted confocal microscope Nikon Eclipse Ti-E (Nikon GmbH, Düsseldorf, Germany) and acquired images were assessed with the associated software NIS-Elements, Version 4.10.04 (Nikon GmbH, Düsseldorf, Germany).

2.2.5.2 Transmission electron microscopy

Ultrastructural images were gathered with the electron microscope „LEO 912 AB OMEGA“ (Carl Zeiss Microscopy GmbH, Jena, Germany) and assessed with the software Image SP, version 1.2.3.46 (x64) (SYSPROG & TRS, Moorenweis, Germany).

2.2.5.3 Scanning electron microscopy

Images were acquired with the field emission scanning electron microscope Sigma300VP (Carl Zeiss Microscopy GmbH, Jena, Germany) using the detectors InLens and SE2. Images were assessed with the associated software SmartSEM, version 6.01 (Carl Zeiss Microscopy GmbH).

2.2.5.4 Serial block-face scanning electron microscopy (SBF-SEM)

Images were obtained using the field emission scanning electron microscope (Sigma300VP FE-SEM; Carl Zeiss Microscopy GmbH, Jena, Germany) equipped with an automated ultramicrotome inside the vacuum chamber (3View2XP System; Gatan Inc., Pleasanton, CA, USA). The ultramicrotome cut successive sections at a thickness of 30 nm. After each section, the sample block-face was scanned. The microscope, the stage and the ultramicrotome were controlled using DigitalMicrograph® software Gatan Microscopy Suite® (GMS), version 3.22.1461.0 (Gatan Inc). The SEM was operated in variable pressure mode (VP-Mode). The sample was scanned in VP-Mode to reduce artefacts arising from sample charging with a chamber pressure of 15 Pa and a landing energy of 3,5 kV.

2.2.6 Image Processing

2.2.6.1 Processing of confocal data

CLSM images were processed with the free software Image J MBF (NIH, Bethesda, USA). The software includes plugins especially designed for the handling of microscopic images.

2.2.6.2 Processing of electron microscopic data

For the processing of electron microscopic images (adjustment of contrast / brightness, arrangement etc.) the software Adobe Photoshop CS4 (Adobe Systems, Tokyo, Japan) was used.

Alignment of SBF-SEM images was performed using the DigitalMicrograph® scripting of the software Gatan Microscopy Suite® (GMS), version 3.22.1461.0 (Gatan Inc, Pleasanton, CA, USA). Segmentation was performed using the TrakEM2 plug-in of the open-source image processing framework Fiji [95] and subsequent visualization was carried out with the open-source software platform Tomviz, version 1.8.0.

2.2.7 Statistical analysis

Data were analysed by nonparametric statistics because the data for most groups were not normally distributed (shown in the Shapiro-Wilk test [7]). Therefore, Mann-Whitney U tests and the Kruskal-Wallis H-Test for one-way Analysis of Variance (ANOVA) were used for pairwise and global between-group comparisons, respectively. When multiple tests of one kind were performed within a single experiment, we corrected the observed p-values by a Bonferroni post hoc test. Data are reported as bar graphs including a standard error bar. P levels are indicated as *P<0.05, **P<0.01, or ***P<0.001. A value of P<0.05 was considered as statistically significant.
Statistical analyses were performed using the software Prism 5 (GraphPad Software, San Diego, CA, USA).

3. Results

3.1 Detailed examination of MV biogenesis using light and transmission electron microscopy in comparison

To determine which microscopic approach was the most suitable for studying EV release, we cultivated MyEnd and later AoEnd cells under serum starvation and conducted a detailed morphological analysis of EV biogenesis using Confocal Laser Scanning Microscopy (CLSM) and Transmission Electron Microscopy (TEM). Both methods were subsequently compared.

We first analysed EV biogenesis using CLSM, as preparation for this microscopic approach required relatively little time, effort, and materials. To enable 3D-reconstruction of the endothelial cell plasma membrane, endothelial glycocalyx was labelled using the fluorescent dye WGATxRed-X which exhibited bright, red fluorescence (excitation/emission maxima ~ 595/615 nm). Nucleic acids and therefore cell nuclei were visualized using the fluorescent dye DAPI which exhibited blue fluorescence (excitation/emission maxima ~ 358/461 nm). CLSM was very effective in providing a first impression and overview of the cells' morphological condition and a first assessment of a possible production of EVs.

3.1.1 Light microscopic analysis of MyEnd cells under serum starvation

0 hours under serum starvation

EV release was analysed in confluent MyEnd cells using WGATxRed-X and DAPI staining using CLSM. Individual cells showed small vesicular structures at the cell surface in a random distribution (Fig. 3). These vesicular structures could be interpreted as membrane-bound EVs that had pinched off from the MyEnds' plasma membrane, but likewise as simple cellular membrane protrusions that would also emit the red fluorescence signal. Due to the very limited resolution of the CLSM (~ 200 nm in XY; 500 nm in Z), the exact nature of these vesicular structures on the cell surface could not be determined with full certainty. The exact size, shape and morphology of the EVs remained unclear and a possible

classification was not possible using this light microscopic approach. If they were indeed EVs, determining their exact class was not possible.

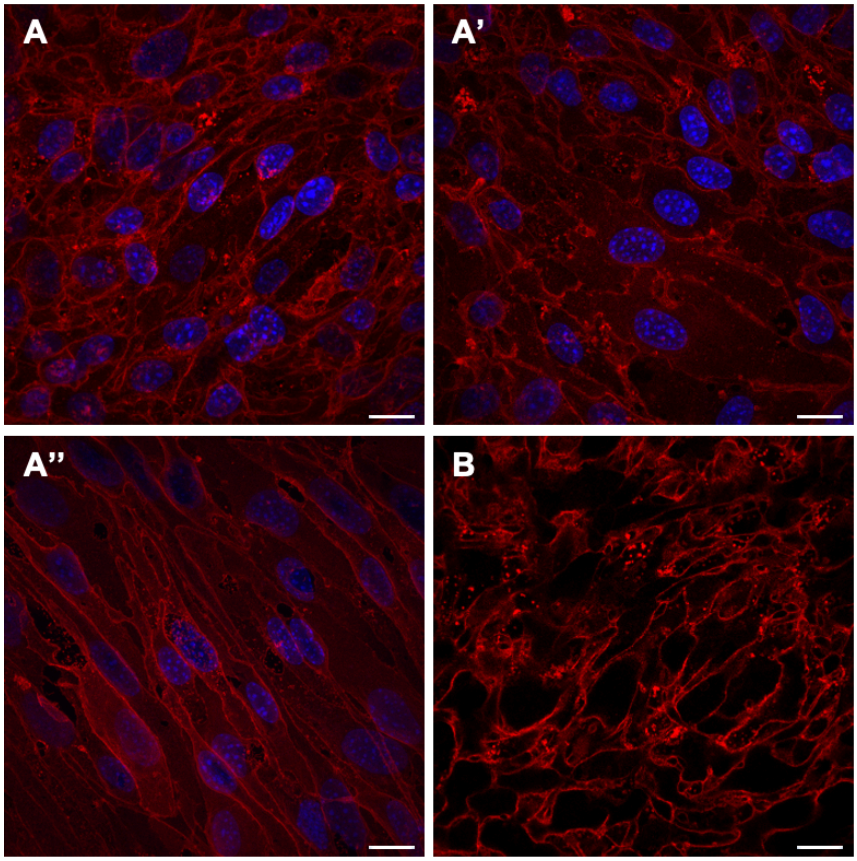

Fig. 3 MyEnd cells after 0 hours of starvation. Representative confocal images of MyEnd cells labelled with WGA-TxRed (red) and DAPI (blue). A'-A'': Maximum Intensity Projection, B: WGATxRed-X staining. **Scale bar:** 10 µm.

24 hours under serum starvation

After 24 hours under serum starvation, the number of MyEnd cells showing the red fluorescent vesicular structures on their surface as well as its mere number had significantly increased (Fig. 4). EVs were randomly distributed over the cells. While the number of EV-producing MyEnd cells increased, a fraction of cells, which we thereafter describe as "inactive", did not show any EVs on their surface. However, the CLSM images did not allow for a statistical analysis of this fraction in comparison to the fraction of active cells in relation to the time under starvation.

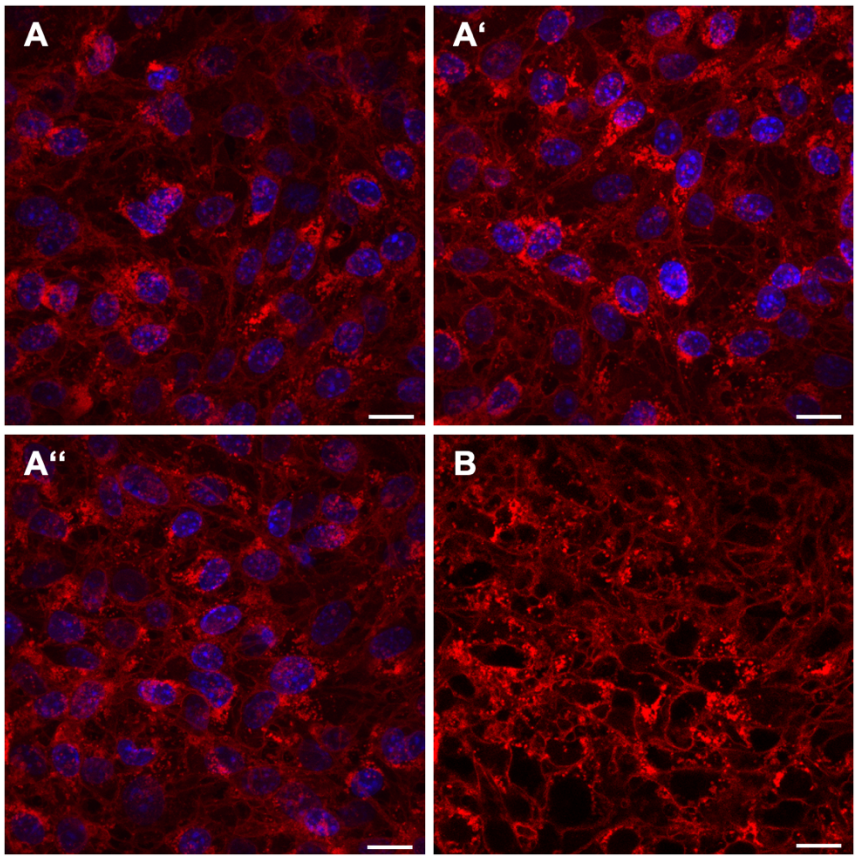

Fig. 4 MyEnd cells after 24 hours of starvation. Representative confocal images of MyEnd cells labelled with WGA-TxRed (red) and DAPI (blue). A’-A’’: Maximum Intensity Projection, B: WGATxRed-X staining. **Scale bar:** 10 µm.

48 hours under serum starvation

After 48 hours under serum starvation, the condition of the endothelial cells notably changed: The cells began to look frail and damaged, some showed gaping holes in their cytoplasm. While the WGA-TxRed staining was straight-lined in MyEnd cells after 24 hours of starvation (Fig. 4), WGA-TxRed staining was meandering with gaps in MyEnd cells after 48 hours of starvation (Fig. 5, arrows) indicating that the cell-cell contacts had started to diminish.

The fraction of cells showing the red fluorescent vesicular structures on their surface as well as the number of these structures was comparable to MyEnd cells after 24 hours of starvation.

The most striking observation was the presence of a large number of apoptotic bodies that pinched off from the endothelial cell surface (Fig. 5, arrowheads). They were visible as round vesicles, recognizable by their typical large size of up to 5000 nm. Per definition, apoptotic bodies are released specifically by cells undergoing apoptosis [40], which fit the morphological observation of the cells' condition stated above.

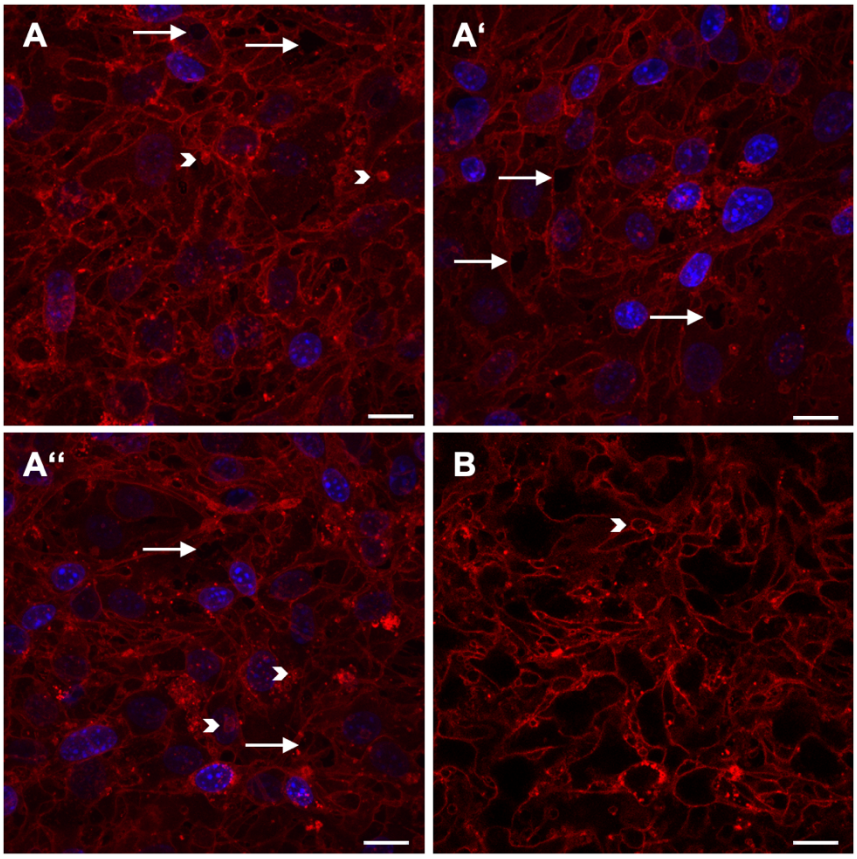

Fig. 5 MyEnd cells after 48 hours of starvation. Representative confocal images of MyEnd cells labelled with WGA-TxRed (red) and DAPI (blue). A'-A'': Maximum Intensity Projection, B: WGATxRed-X staining. **Scale bar:** 10 µm**. Arrows:** Diminishing cell-cell contacts **Arrowheads:** Apoptotic bodies.

72 hours under serum starvation

While the number of cells showing EV production (excluding apoptotic bodies) and the number of EVs did not increase after further serum starvation, cells were deteriorating and completely losing their cell-cell-contacts. Gaping holes in between the cells and in the cells' cytoplasm were clearly visible with some cells only still being connected via thin threads. (Fig. 6, arrows). The number of cells producing apoptotic bodies increased after 72 hours under serum starvation (Fig. 6).

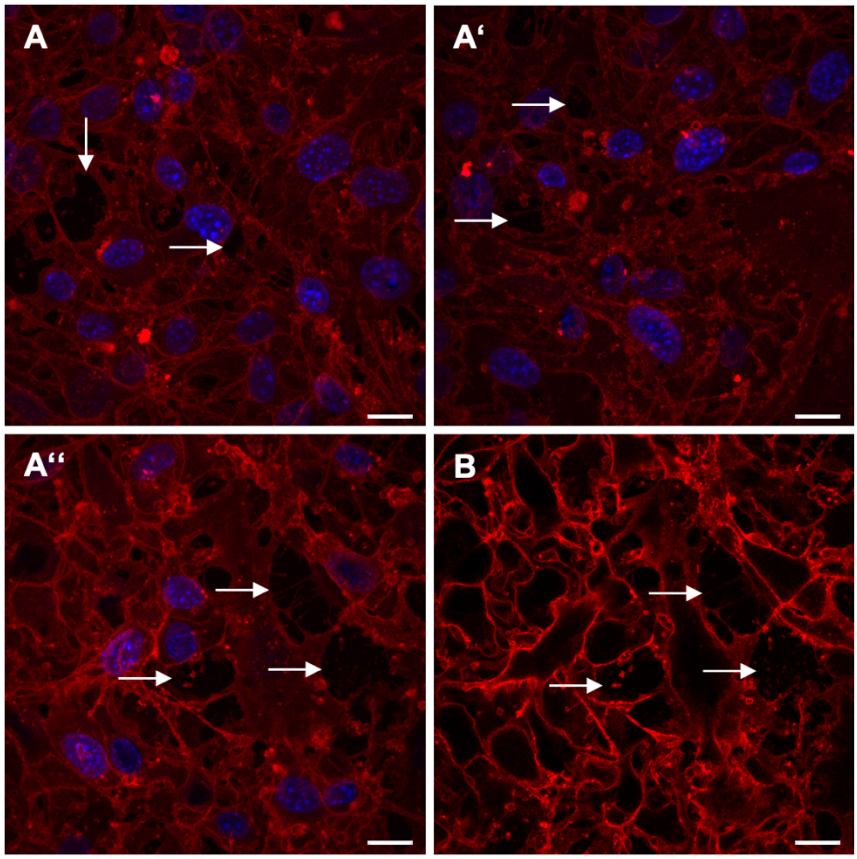

Fig. 6 MyEnd cells after 72 hours of starvation. Representative confocal images of MyEnd cells labelled with WGA-TxRed (red) and DAPI (blue). A'-A'': Maximum Intensity Projection, B: WGATxRed-X staining. **Scale bar:** 10 µm. **Arrows**: Gaping holes in between the cells and in the cells' cytoplasm.

3.1.2 Transmission electron microscopic analysis of MV and exosome biogenesis by MyEnd cells under serum starvation

After gaining a first impression of the effect of serum starvation on cultured MyEnd cells' morphology and EV production over time, we turned to a high-resolution microscopic transmission electron microscopic approach using TEM to analyse EV biogenesis on an ultrastructural level. As the resolution in TEM is below 50 picometres, this method allowed a detailed analysis of cellular and subcellular components. Composition and organization of the cell content (cytoplasm, cytoskeleton, cell organelles) could be visualized at the ultrastructural level. In addition, processes occurring on the plasma membrane including EV release could be visualized as such and the vesicles could subsequently be allocated to their EV class by their typical size, morphology and biogenesis (Fig. 7).

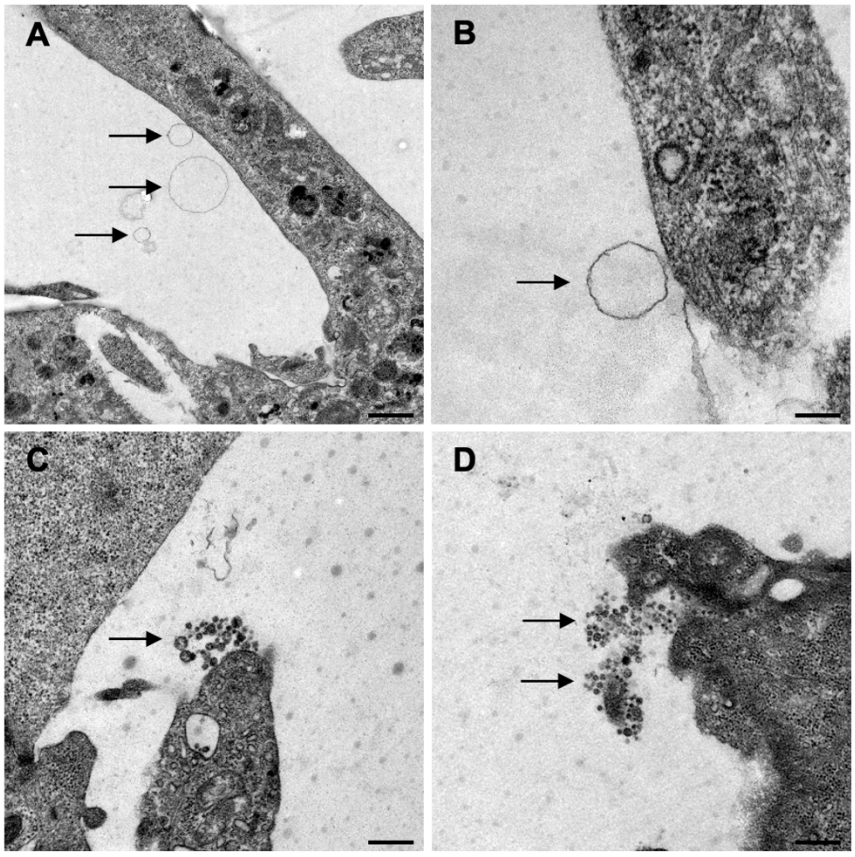

Fig. 7 Depiction of the two examined EV classes. Transmission electron micrographs of MyEnd cells producing MVs, (upper row, arrows) and exosomes (lower row, arrows). Scale bars: A: 1000 nm, B: 800 nm, C-D: 250 nm.

MVs produced by MyEnd cells under serum starvation had an average size of 50–2,000 nm and were membrane-enclosed (Fig. 7, upper row). They could be depicted in the extracellular environment, usually as a single vesicle, but at times together with a handful of other MVs, or during their budding process on the plasma membrane. Exosomes produced by MyEnd cells under serum starvation had an average size of 30–100 nm and were usually found densely concentrated in groups and close to the plasma membrane (Fig. 7, lower row).

We first focused on analysing the different steps of MV biogenesis in detail: the direct outward budding and subsequent fission of the plasma membrane and finally, MV release into the extracellular space [49].

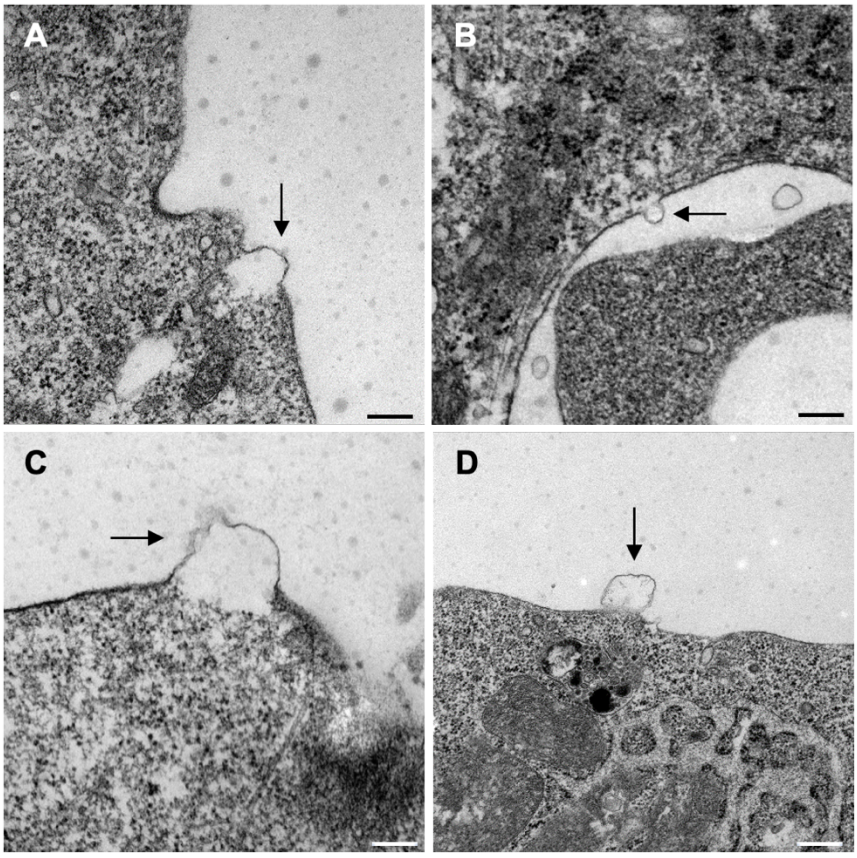

Fig. 8 Transmission electron micrographs of different steps of MV biogenesis: 1) Direct outward budding of the plasma membrane. Pictured is the initial formation of MVs through direct outward budding of the plasma membrane (arrows) on different areas of the MyEnd cells' surface. **Scale bars:** A-B: 250 nm, C: 100 nm, D: 1000 nm.

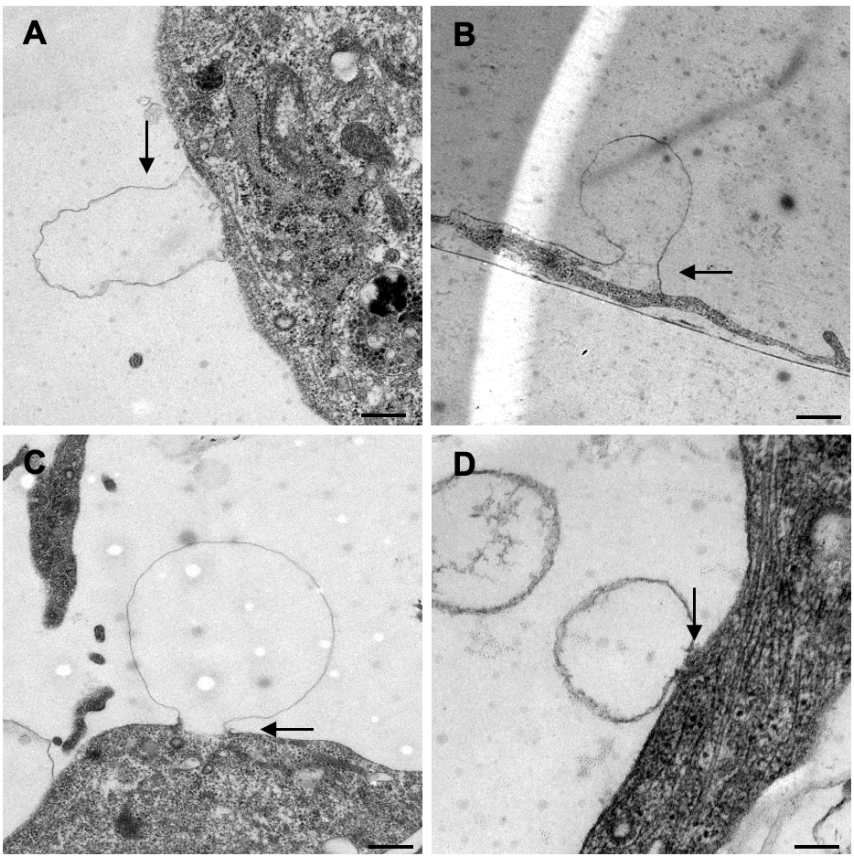

Fig. 9 Transmission electron micrographs of different steps of MV biogenesis: 2) Progressive outward budding and narrowing of the vesicles' neck. Pictured is the progressive outward budding of the plasma membrane (A-B, arrows) and – once the vesicles had reached their final size – the formation of a neck in preparation for scission (C-D, arrows). **Scale bars**: A: 250 nm, B-D: 1000 nm.

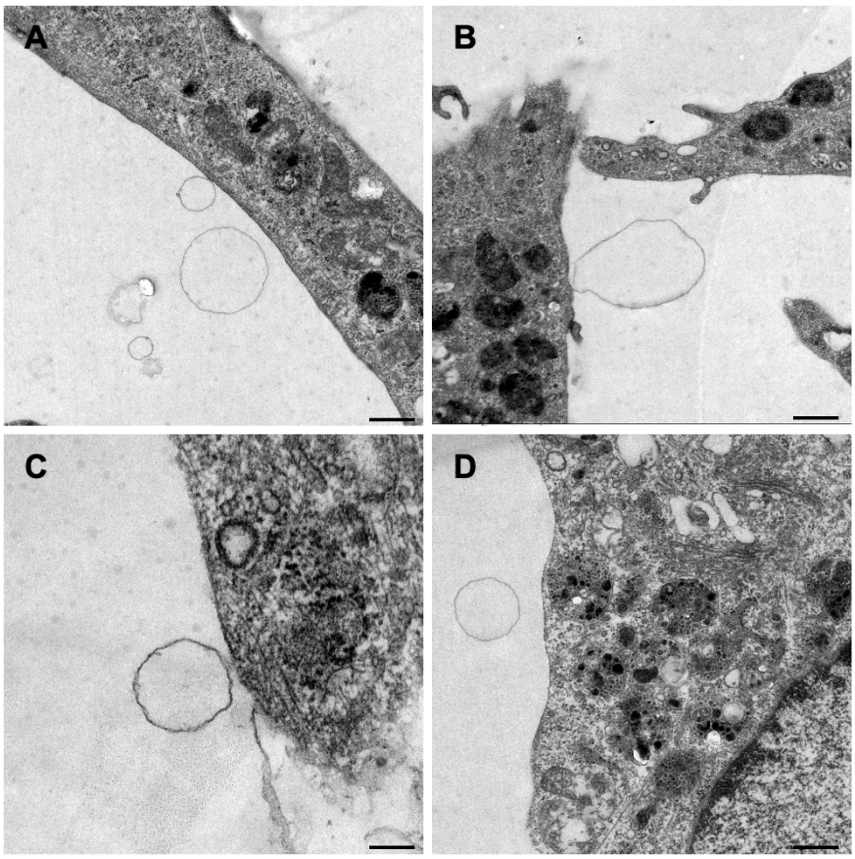

Fig. 10 Transmission electron micrographs of different steps of MV biogenesis: 3) Detachment of the MVs. Pictured is the completion of the budding process and the detachment of the MVs from the plasma membrane. The MVs are released into the extracellular environment. **Scale bars:** A-B: 1000 nm, C: 100 nm, D: 250 nm.

MV formation in serum-starved MyEnd cells was initiated by direct outward budding of the luminal plasma membrane (Fig. 8). This process could be observed all over the cells' surface; no preferred location of MV biogenesis could be detected. One striking observation was the clear delamination of the plasma membrane from the cortical cytoskeleton during the process of outward budding. The emerging MVs presented a lucent content and did not include any electron-dense cellular organelles. After the continuous narrowing of the vesicles' neck (Fig. 9), the round shaped MVs pinched off from the cells' plasma membrane and were released into the extracellular environment (Fig. 10).

Next, we studied the biogenesis of exosomes in detail (Fig. 11).

Exosomes are of endosomal origin as they arise from endosomal compartments called multivesicular bodies (MVBs) [35].

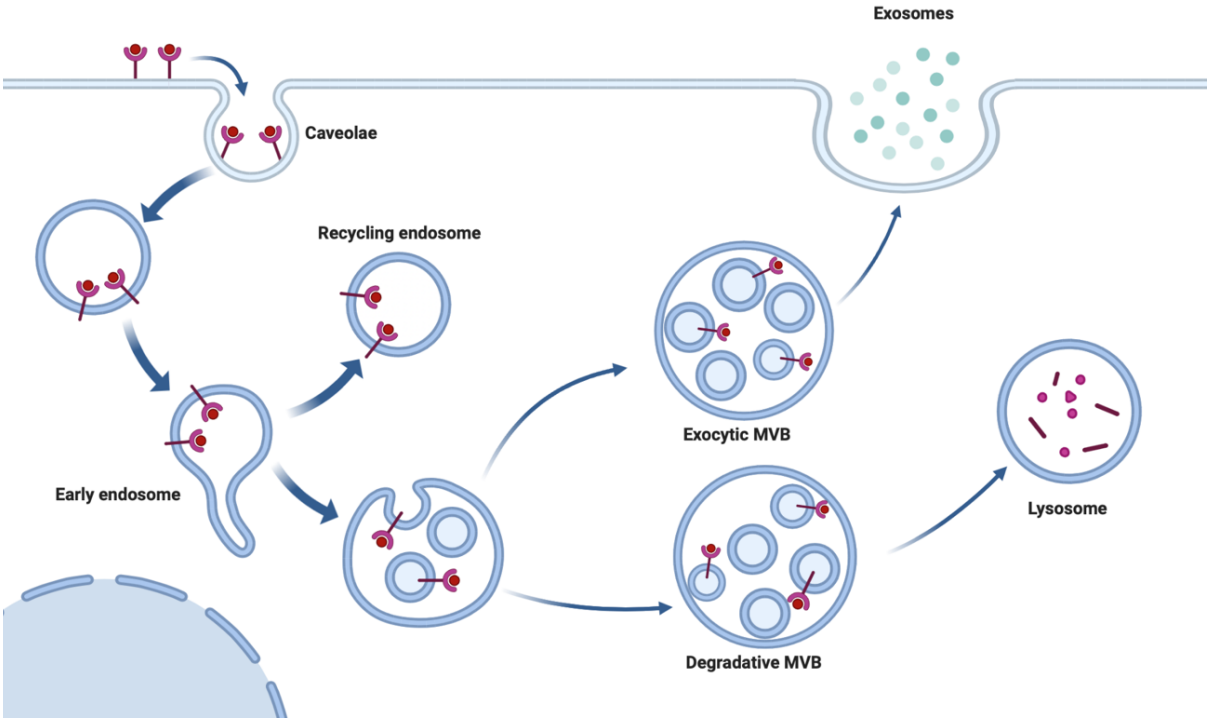

Fig. 11 Schematic model of the generation of exosomes. Image created with BioRender.com [9].

We depicted the exosome biogenesis in serum-starved MyEnd cells step by step starting at the beginning of the endosomal pathway, the endocytosis. Clathrin-mediated endocytosis occurs through the formation of clathrin-coated pits (CCPs) [96]. Their formation can be divided into four stages: initiation, stabilization, maturation, and membrane fission. In subsequent steps, the released clathrin-coated vesicles (CCVs) are rapidly uncoated, undergo multiple homotypic fusion events, and ultimately deliver their cargo to early endosomes [96]. The different stages of endocytosis could be observed in serum-starved MyEnd cells (Fig. 12).

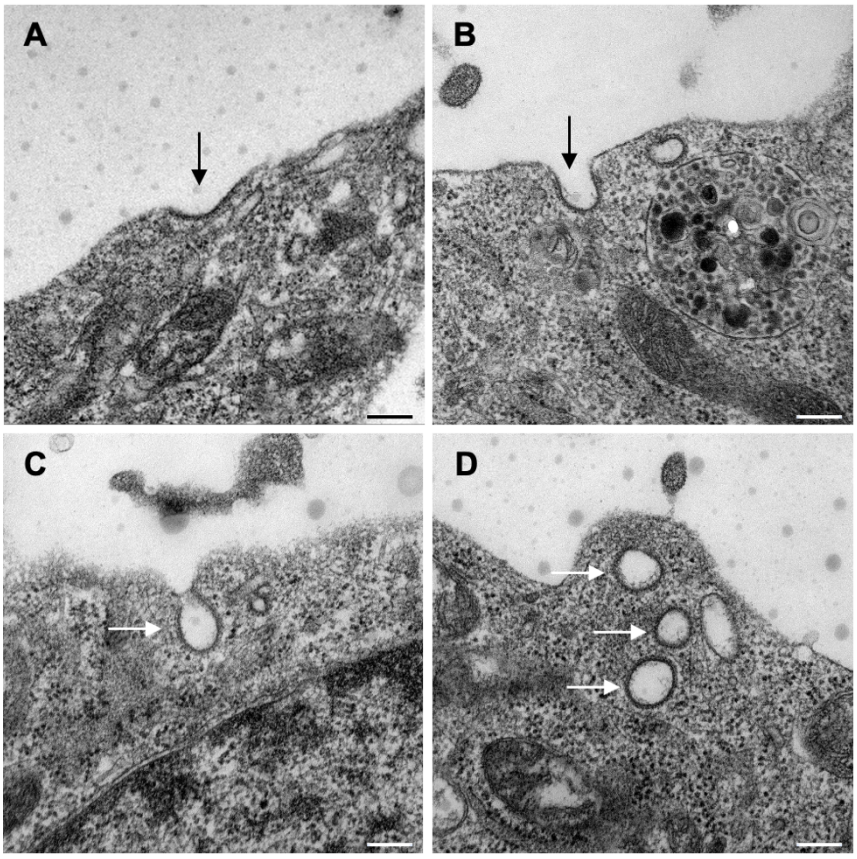

Fig. 12 Transmission electron micrographs of different steps of endocytosis in serum-starved MyEnd cells: Formation of CCPs and CCVs. Pictured in A and B is the initiation and stabilization of a CCP (arrows). The CCP deepens and matures (pictured in C, arrow) and is finally released inward into the cell as a CCV through scission from the plasma membrane (pictured in D, arrows). **Scale bars:** A-D: 100 nm.

The early endosomes then mature into late endosomes – also known as MVBs [97] – a process which we also observed in serum-starved MyEnd cells: The endosomal membrane invaginates inward to generate ILVs in the lumen of the organelles (Fig. 13, A-D). This gives the MVBs their characteristic (and name-giving) multivesicular morphology (Fig. 13, E-F).

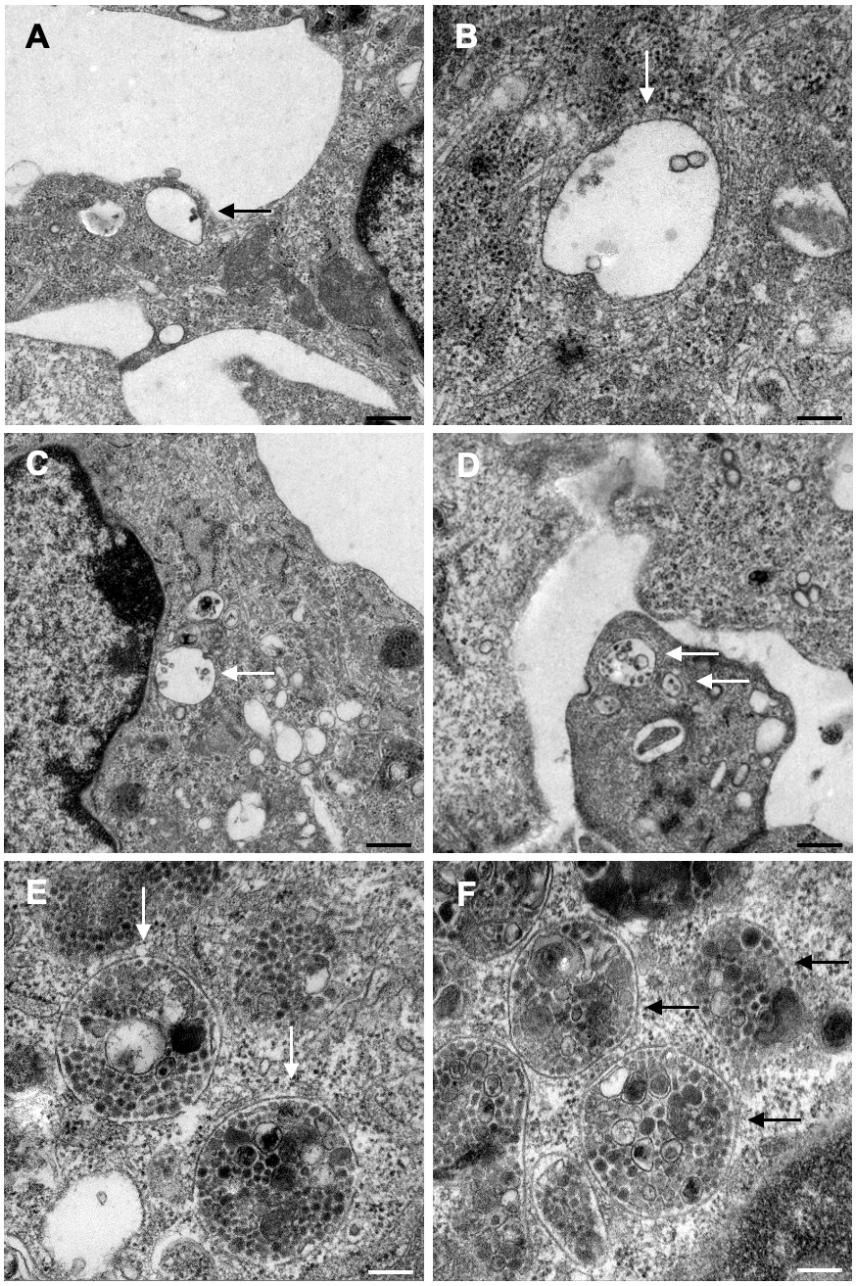

Fig. 13 Transmission electron micrographs of early endosome maturation to late endosomes/MVBs in serum-starved MyEnd cells. Pictured is the process of endosome maturation through ILV generation (A-D, arrows) and the generation of large MVBs (E-F, arrows). **Scale bars:** A: 800 nm, B: 100 nm, C: 800 nm, D: 1000 nm, E-F: 100 nm.

It has been described in literature that during the last steps of exosome biogenesis, MVBs travel to the surface, fuse with the plasma membrane and release the ILVs into the extracellular environment as exosomes (described and

pictured in Akers et al., 2013 [16]). While screening the TEM-sections for those morphological correlates, we discovered the following occurrence.

We did not find any morphological evidence of MVBs' direct fusion with the plasma membrane. Instead, we found morphological evidence that in serum-starved MyEnd cells, MVBs were incorporated into a new distinct cellular compartment first (Fig. 14). There, the MVB membrane dissolved and the exosomes were released within this compartment. The content of the compartments was inhomogeneous and consisted of the former MVBs – some still possessing their endosomal membrane – and the ILVs within as well as various other particles (Fig. 14). The most striking observation was that the fraction of the cell membrane at the apical end of this compartment facing the extracellular compartment did not show the typical continuous endothelium, but instead consisted of fenestrated endothelium (Fig. 14 arrowheads). We could observe the characteristic properties of fenestrated endothelium: 60–80 nm diameter transcellular pores spanned by fenestral diaphragms (FDs) (Fig. 14, 15) [98].

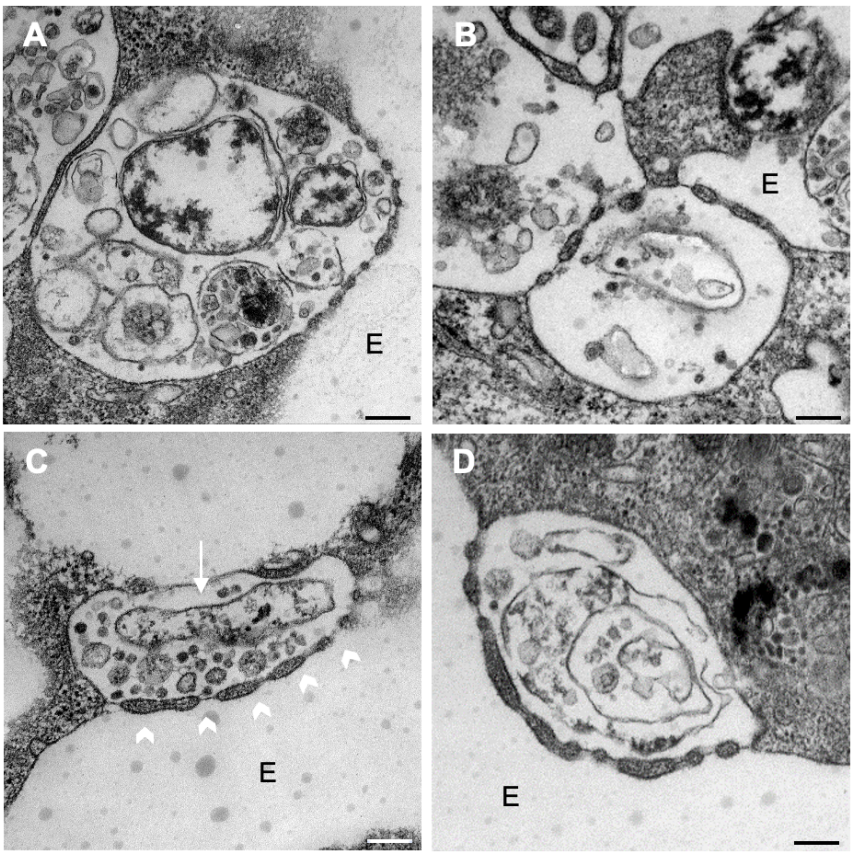

Fig. 14 Transmission electron micrographs of MVBs and exosomes in a "new cellular compartment". Pictured are the "new cellular compartments" containing the MVBs and their respective content, now free within this section. Also clearly visible is the fenestral endothelium with transcellular pores spanned by fenestral diagrams. **Arrow:** "new cellular department". **Arrowheads:** fenestral endothelium. **E:** extracellular department **Scale bars:** A: 250 nm, B-D: 100 nm.

Below the FDs can be seen "en face" to reveal their characteristic radial diaphragm fibrils and a central knob (Fig. 15, A-D).

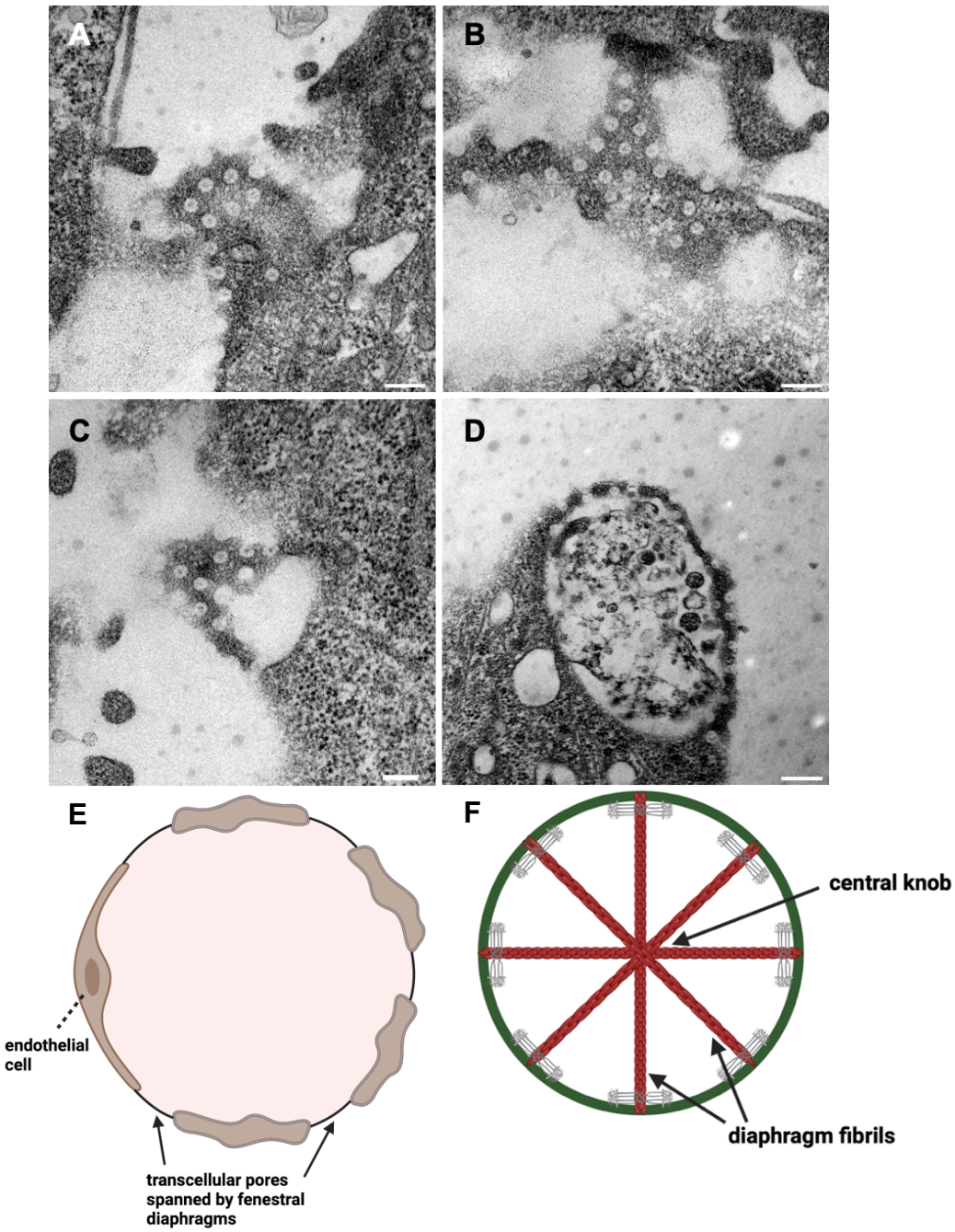

Fig. 15 Endothelial fenestrations. Transmission electron micrographs of endothelial fenestrations (A-D), pictured are endothelial fenestrations in a frontal plane. Schematic model of an endothelial cell with transcellular pores (E), created with BioRender.com [9]. Schematic model of the endothelial diaphragm structure (F), created with BioRender.com [9]. **Scale bars:** A-C: 100 nm, D: 250 nm.

We could depict these new “cellular compartments” containing MVBs and exosomes in all investigated MyEnd and later AoEnd cell lines whether they were

subjected to serum starvation only or to both starvation and additional TNF-α stimulation in the subsequent experiments. The content of the compartments always consisted of the former MVBs and the ILVs within as well as various other particles. In some sections, we could identify the afore-described compartments lacking the apical membrane, possibly depicting the last step of exosome release (Fig. 16).

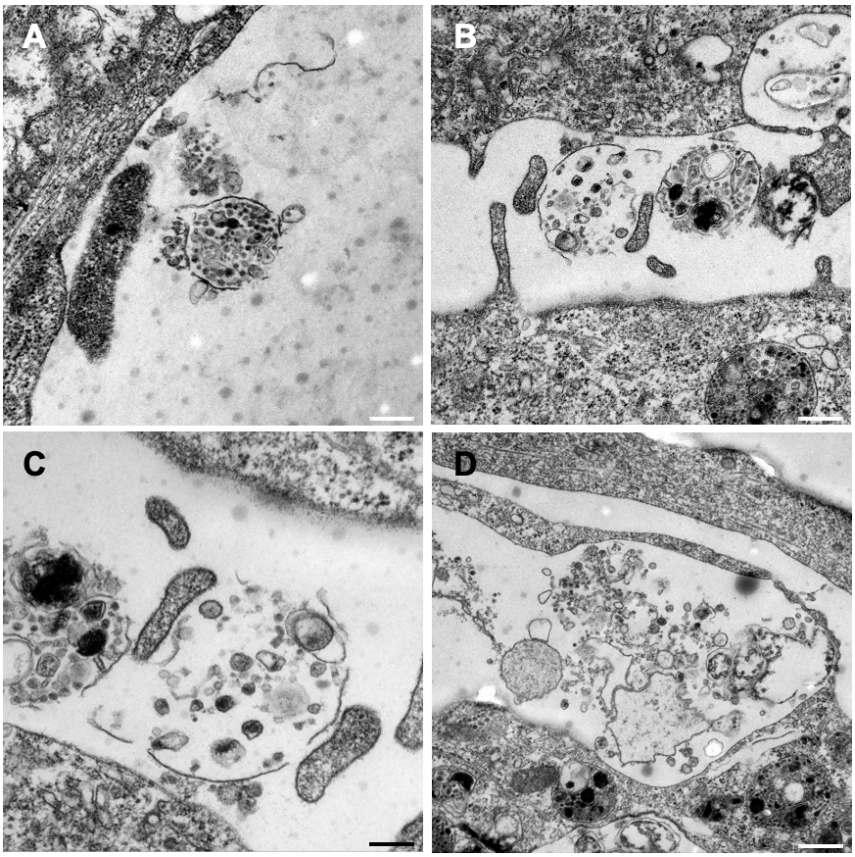

Fig. 16 Transmission electron micrographs of endothelial "compartments" and exosome release. Scale bars: A-B: 250 nm, C: 100 nm, D: 250 nm.

We were not able to follow the fate of these new compartments in more detail. However, from our observations we conclude that these compartments represent an important step of MVB maturation and exosome release.

3.1.3 Transmission electron microscopic analysis of the influence of serum starvation on MyEnd cell morphology

The light microscopic analysis of MyEnd cells under serum starvation had shown that after 48 hours under serum starvation, the cells had begun to deteriorate, lose their cell-cell-contacts and produce high amounts of apoptotic bodies (Fig. 5, 6). We therefore decided to conduct a detailed TEM analysis of cultured MyEnd cells over time, with the aim of depicting the cells' ultrastructural condition.

Of special interest was the examination of the cells' condition after 72 hours of serum starvation – as this is, according to literature, the common time point to extract EVs for studies and functional tests.

0 hours under serum starvation

The MyEnd cells were in a physiological, healthy condition. The composition and organization of the cell content (cytoplasm, cytoskeleton, cell organelles) was normal and the cell membrane was not disrupted. No morphological abnormalities could be detected (Fig. 17).

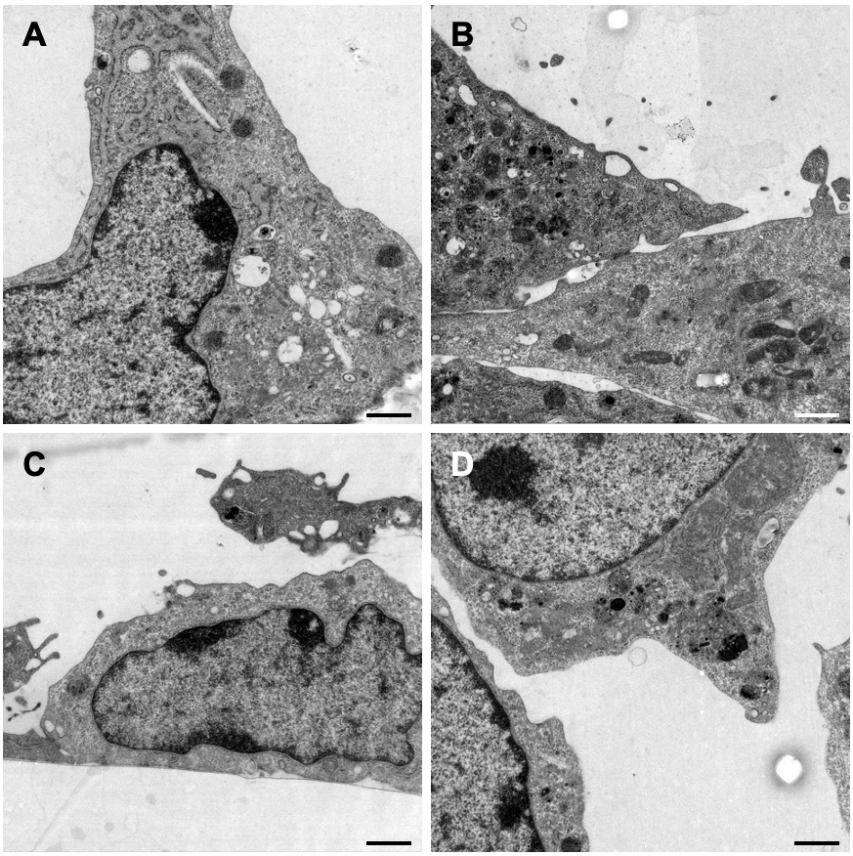

Fig. 17 Transmission electron micrographs of MyEnd cells after 0 hours of starvation. Scale bars: A-D: 1000 nm.

24 hours under serum starvation

The morphological state of the cells had not changed significantly after 24 hours under serum starvation. The MyEnd cells were still in a physiological, healthy condition, just as described above (Fig. 18).

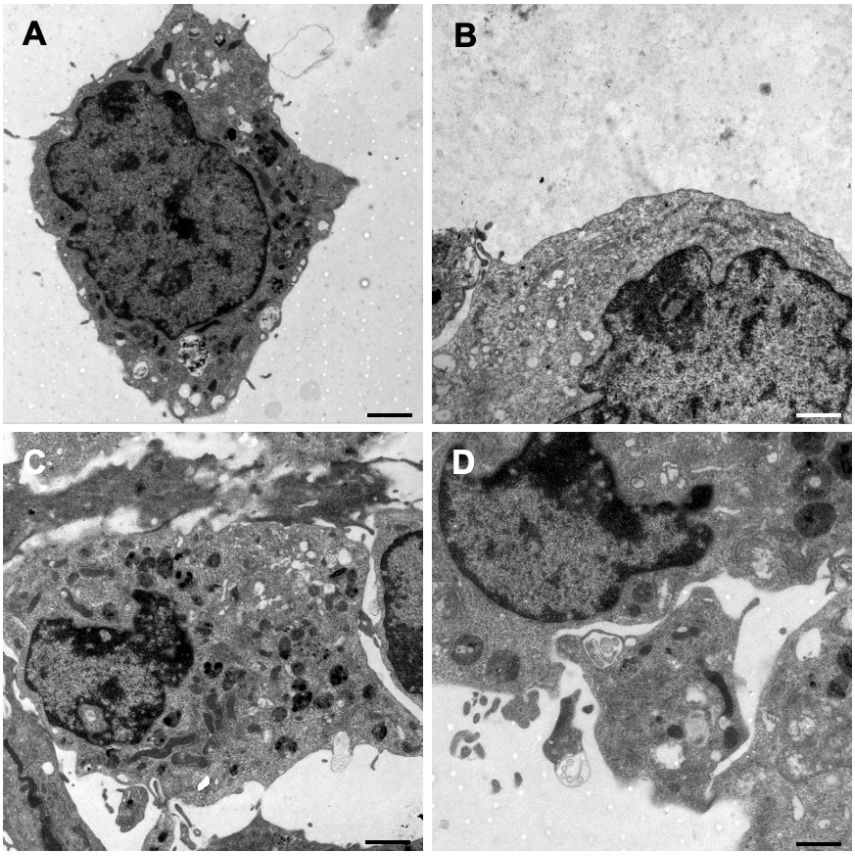

Fig. 18 Transmission electron micrographs of MyEnd cells after 24 hours of starvation. Scale bars: A-D: 1000 nm.

48 hours under serum starvation

The observations with the CLSM had shown that after at least 48 hours of cultivation under serum starvation, the MyEnd cells had slowly begun to look frail and damaged. This observation could be corroborated with the electron microscopic images. In some cells, the cytoplasm showed holes (Fig. 19, arrowheads). Also noticeable was a rapidly increasing amount of MVBs (Fig. 19, arrows).

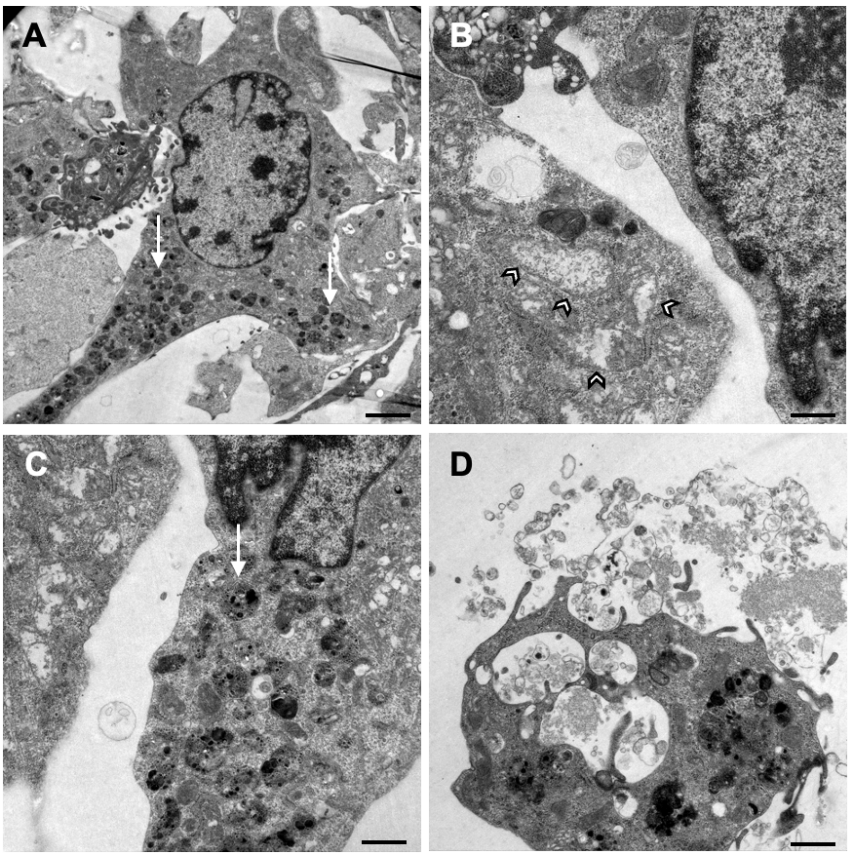

Fig. 19 Transmission electron micrographs of MyEnd cells after 48 hours of starvation. MyEnd cells show a significant increase in the amount of MVBs (A, C, arrows) and intracellular holes (B, arrowheads). **Scale bars**: A: 2500 nm, B, C, D: 1000 nm.

72 hours under serum starvation

After 72 hours of cultivation under serum starvation, the MyEnd cells were visibly deteriorating – the morphological change in the cells' condition compared to the start of the cultivation was striking (Fig. 20).

Firstly, the cells showed a great abundance of big MVBs. They occupied most of the cells' cytoplasm. Apart from that, the MyEnd cells displayed a lot of unusually large cisterns of the rough endoplasmatic reticulum (rER), their size sometimes overtaking the size of the nucleus.

Both observations could be indicators of an impaired endosomal-lysosomal degradation pathway.

Additionally, in most cells, the cytoplasm displayed gaping holes and the cell content had lost its physiological composition and organization.

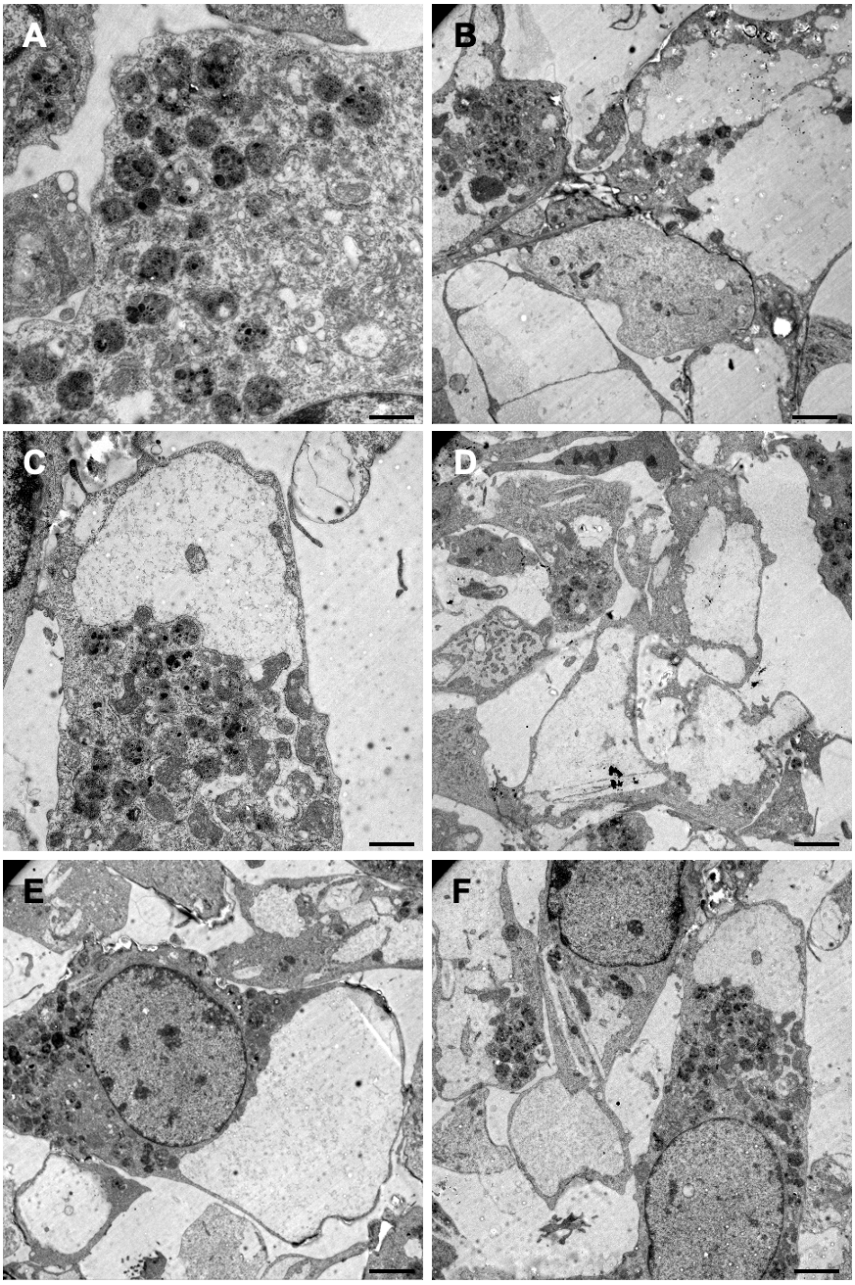

Fig. 20 Transmission electron micrographs of MyEnd cells after 72 hours of starvation. Scale bars: A: 1000 nm, B: 2500 nm, C: 1000 nm, D-F: 2500 nm.

Furthermore, we couldn't detect any caveolae on the cell's luminal surface after 72 hours of starvation compared to MyEnd cells 24 hours after starvation (Fig. 21). Caveolae are spherical invaginations of the plasma membrane and involved

in many cellular functions such as transcytosis or signal transduction [99]. As endothelial cells are among the richest in caveolae, a lack thereof was a striking find adding to the appearance of a cell losing its physiological function.

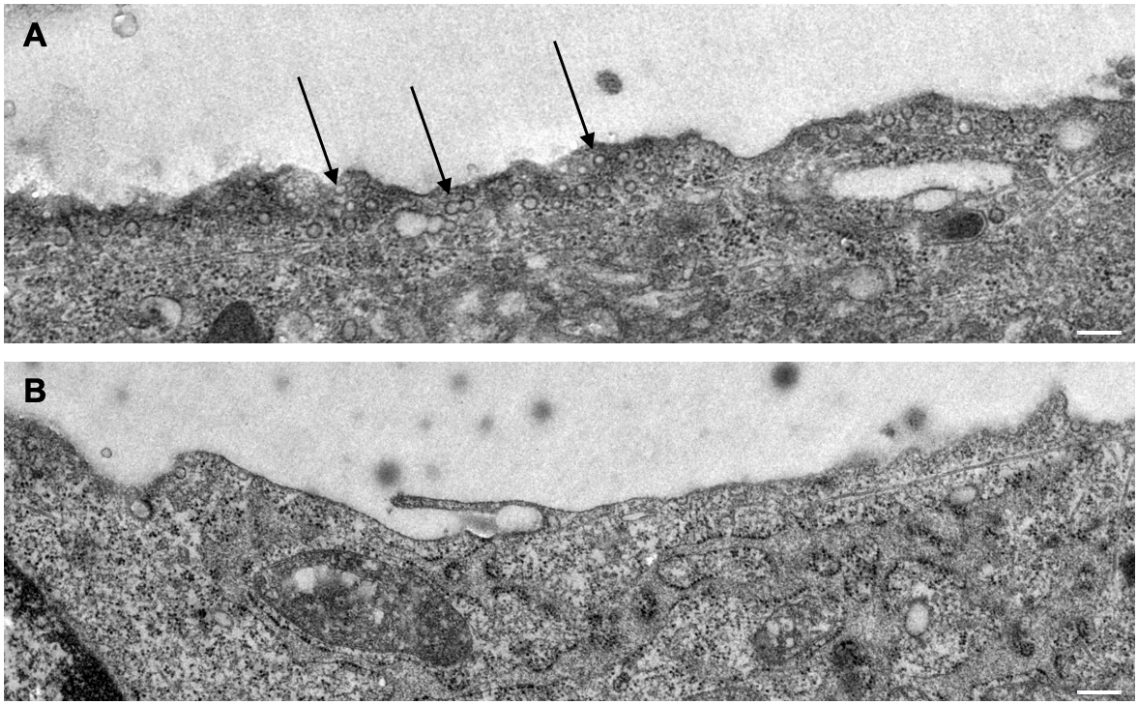

Fig. 21 Transmission electron micrographs of MyEnd cells after 24 versus 72 hours of starvation. A: Abundance of caveolae in MyEnd cells after 24 hours of starvation (arrows), B: Missing caveolae in MyEnd cells after 72 hours of starvation **Scale bars**: A-B: 1000 nm.

3.1.4 Light microscopic analysis of AoEnd cells under serum starvation

After reviewing the results from the examination of MyEnd cells cultured under serum starvation, we performed the exact same tests again, but this time using AoEnd cells instead.

This had several reasons: Firstly, the MyEnd cells stem from the microvascular system – however, atherosclerosis is a disease of the macrovascular system. Therefore, we used AoEnd cells – that stem from the macrovascular system – to allow us to make more precise statements regarding a possible relation of our results to the mechanisms of atherosclerosis. Secondly, we wanted to compare

the two cell lines regarding MV and exosome biogenesis. Lastly, it was of interest whether the AoEnd cells would show the same morphological changes as the MyEnd cells after cultivation under serum starvation.

0 hours under serum starvation

EV release was analysed in confluent AoEnd cells using WGATxRed-X and DAPI staining using CLSM. Similar to MyEnd cells, individual AoEnd cells showed small vesicular structures at the cell surface in a random distribution (Fig. 22). Again, these vesicular structures could be interpreted as membrane-bound EVs or likewise as simple cellular membrane protrusions that would also emit the red fluorescence signal.

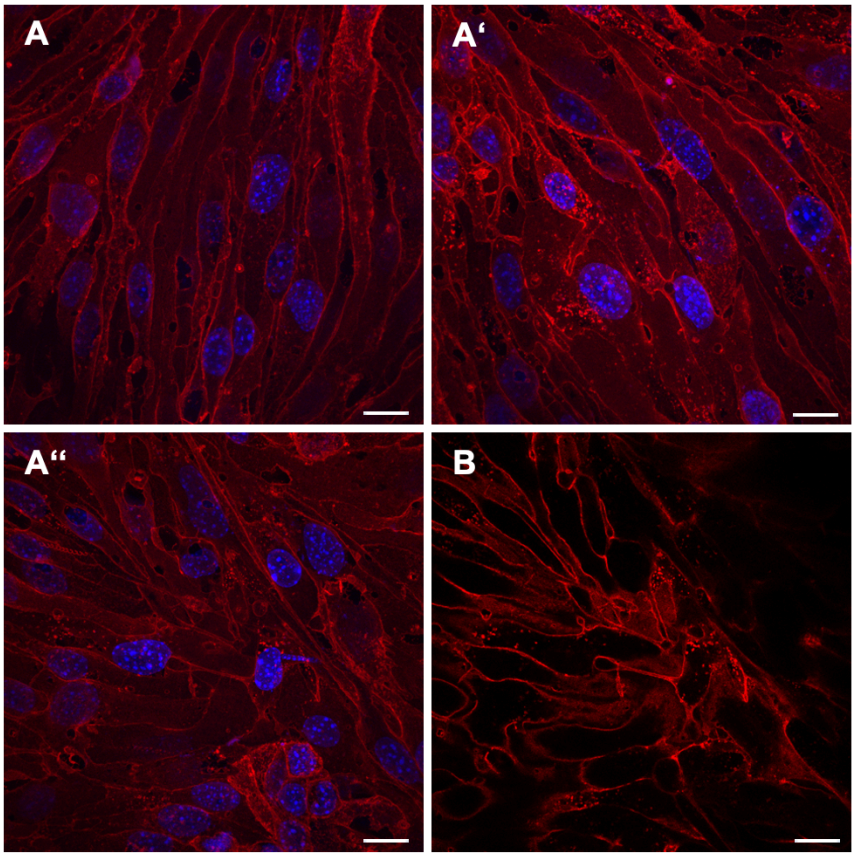

Fig. 22 AoEnd cells after 0 hours of starvation. Representative confocal images of AoEnd cells labelled with WGA-TxRed (red) and DAPI (blue). A’-A’’: Maximum Intensity Projection, B: WGATxRed-X staining. **Scale bar:** 10 µm.

24 hours under serum starvation

After 24 hours under serum starvation, the number of AoEnd cells showing the red fluorescent vesicular structures on their surface as well as its mere number had significantly increased (Fig. 23). EVs were randomly distributed over the cells. While the number of EV-producing AoEnd cells increased, a fraction of cells remained “inactive" and did not show any EVs on their surface. However, the CLSM images did not allow for a statistical analysis of this fraction in comparison to the fraction of active cells in relation to the time under starvation.

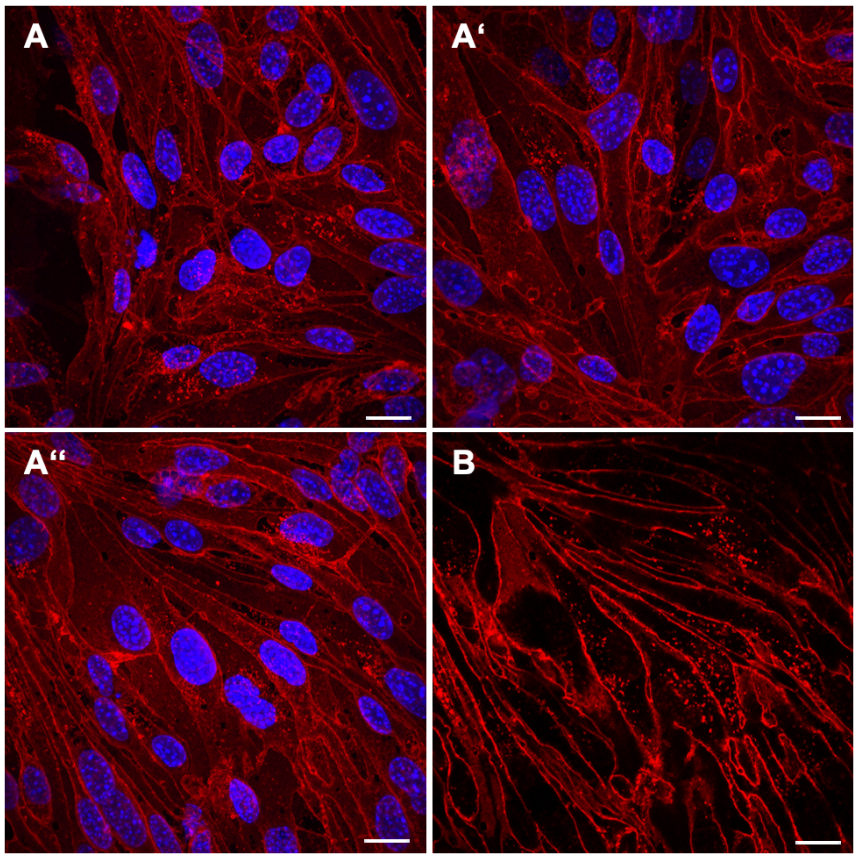

Fig. 23 AoEnd cells after 24 hours of starvation. Representative confocal images of AoEnd cells labelled with WGA-TxRed (red) and DAPI (blue). A’-A’’: Maximum Intensity Projection, B: WGATxRed-X staining. **Scale bar:** 10 µm.

48 hours under serum starvation

After 48 hours under serum starvation, the condition of the MyEnd cells had notably changed for the worse: They had begun to look frail and damaged, some

had shown gaping holes in their cytoplasm (Fig. 5, 6). However, this was not the case for the AoEnd cells. The WGA-TxRed staining was still straight-lined throughout the sample and no gaps in the cell-cell-contacts could be observed (Fig. 24).

The fraction of cells showing the red fluorescent vesicular structures on their surface as well as the number of these structures was comparable to AoEnd cells after 24 hours of starvation and had not increased any further.

In comparison to the MyEnd cells, there were also almost no apoptotic bodies to be found. All these findings indicated that the AoEnd cells were still in a physiological and healthy state.

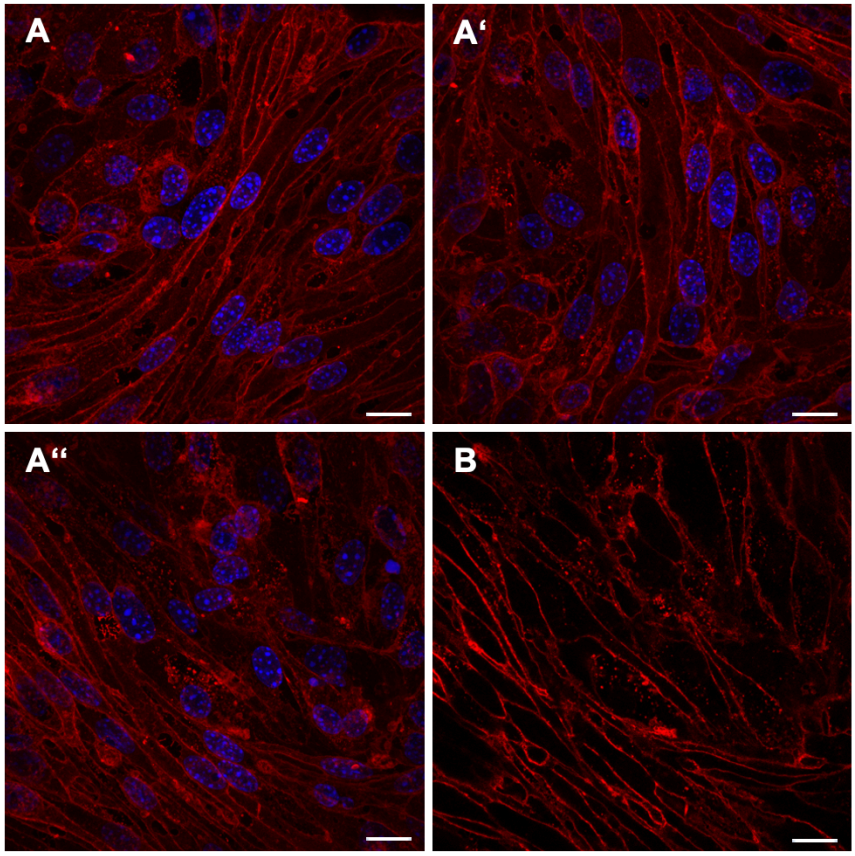

Fig. 24 AoEnd cells after 48 hours of starvation. Representative confocal images of AoEnd cells labelled with WGA-TxRed (red) and DAPI (blue). A’-A’’: Maximum Intensity Projection, B: WGATxRed-X staining. **Scale bar:** 10 µm.

3.1.5 Transmission electron microscopic analysis of MV and exosome biogenesis by AoEnd cells under serum starvation

We used Transmission Electron Microscopy (TEM) as a high-resolution microscopic approach to analyse MV and exosome biogenesis in AoEnd cells on an ultrastructural level.

The MVs produced by AoEnd cells under serum starvation had an average size of 50–2,000 nm and were membrane-enclosed. They could be depicted in the extracellular environment, usually as a single vesicle, but at times together with a handful of other MVs, or during their budding process on the plasma membrane. Exosomes produced by AoEnd cells under serum starvation had an average size of 30–100 nm and were usually found densely concentrated in groups and close to the plasma membrane.

We first focused on analysing the different steps of MV biogenesis in detail: the direct outward budding and subsequent fission of the plasma membrane and finally, MV release into the extracellular space [49].

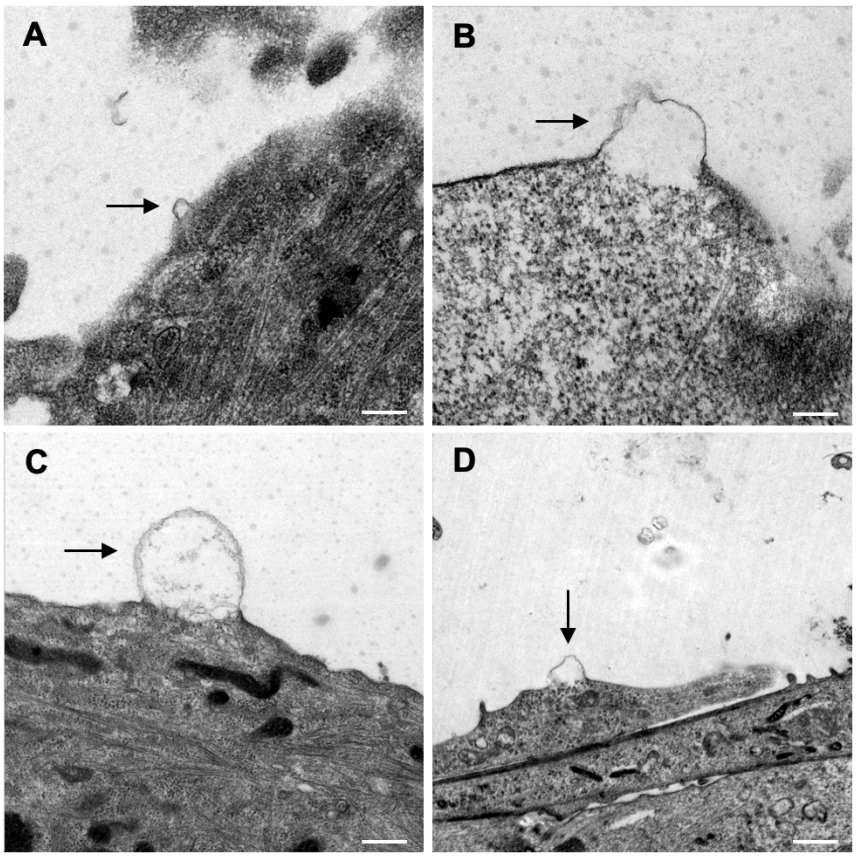

Fig. 25 Transmission electron micrographs of different steps of MV biogenesis: 1) Direct outward budding of the plasma membrane. Pictured is the initial formation of MVs through direct outward budding of the plasma membrane (arrows) on different areas of the AoEnd cells' surface. **Scale bars:** A: 250 nm, B: 100 nm, C: 250 nm, D: 1000 nm.

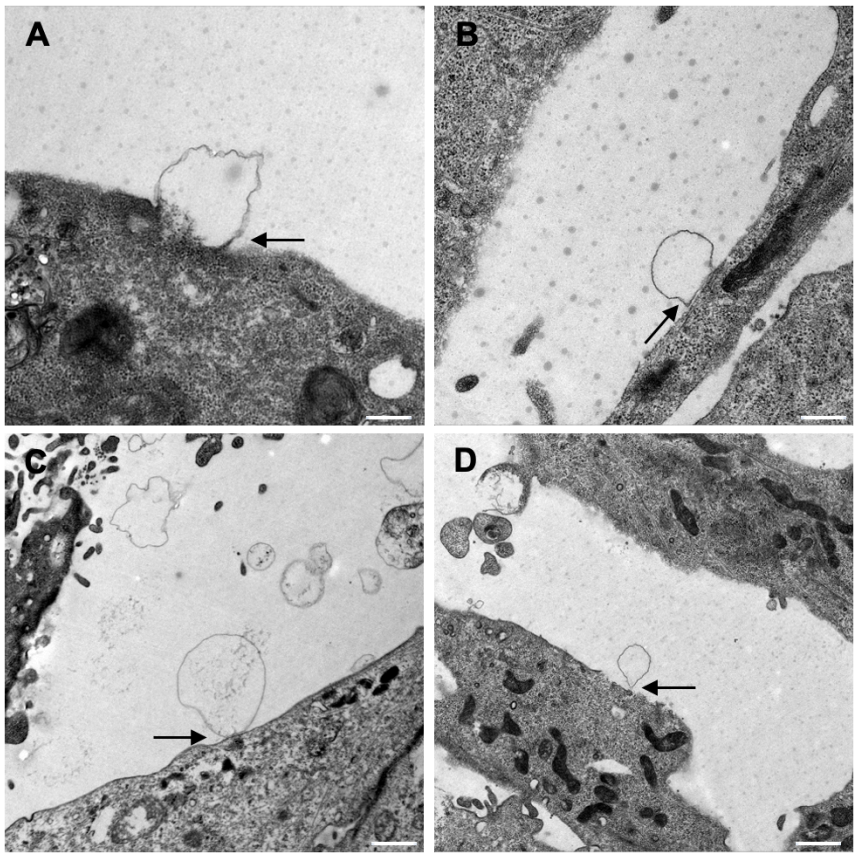

Fig. 26 Transmission electron micrographs of different steps of MV biogenesis: 2) Progressive outward budding and narrowing of the vesicles' neck. Pictured is the progressive outward budding of the plasma membrane (A-B, arrows) and – once the vesicles had reached their final size – the formation of a neck (C-D, arrows) in preparation for scission. **Scale bars**: A-B: 250 nm, C-D: 1000 nm.

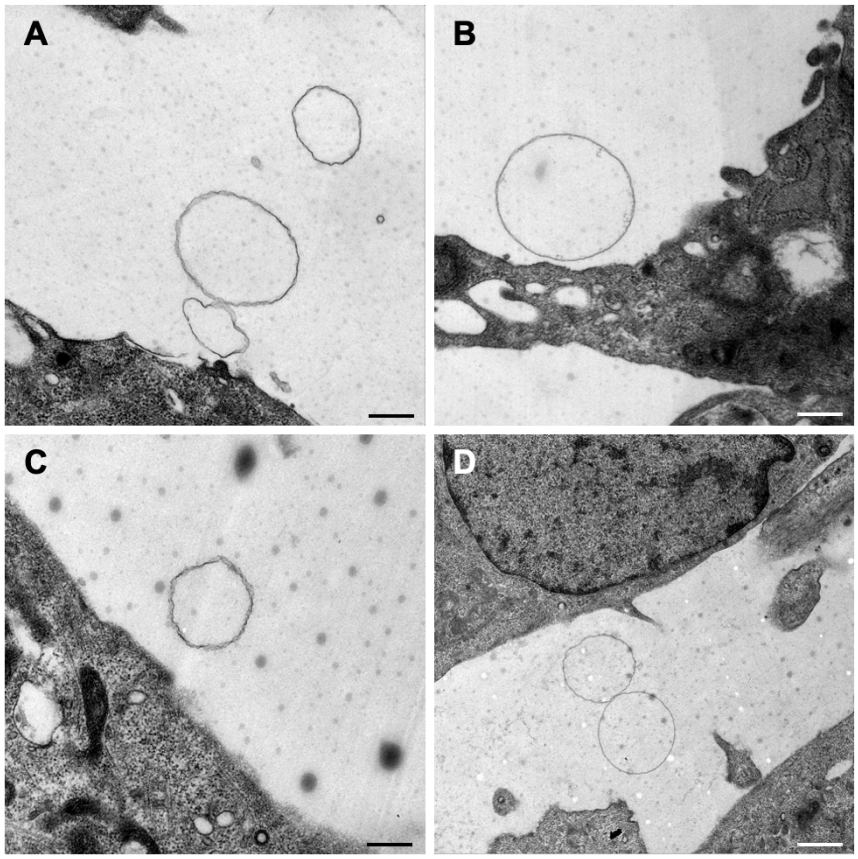

Fig. 27 Transmission electron micrographs of different steps of MV biogenesis: 3) Detachment of the MVs. Pictured is the completion of the budding process and the detachment of the MVs from the plasma membrane. The MVs are released into the extracellular environment. **Scale bars:** A-C: 250 nm, D: 1000 nm.

Similar to serum-starved MyEnd cells, the MV formation in serum-starved AoEnd cells was initiated by direct outward budding of the luminal plasma membrane (Fig. 25). This process could be observed all over the cells' surface; no preferred location of MV biogenesis could be detected. One striking observation was the clear delamination of the plasma membrane from the cortical cytoskeleton during the process of outward budding. The emerging MVs presented a lucent content and did not include any electron-dense cellular organelles. After the continuous narrowing of the vesicles' neck (Fig. 26), the round shaped MVs pinched off from the cells' plasma membrane and were released into the extracellular environment (Fig. 27).

Next, we studied the biogenesis of exosomes in detail. The beginning of the endosomal pathway, the endocytosis, will not be depicted again, as the findings

were exactly as described before (see Fig. 12). In the following, only the endosome maturation and the generation of MVBs will be illustrated (Fig. 28).

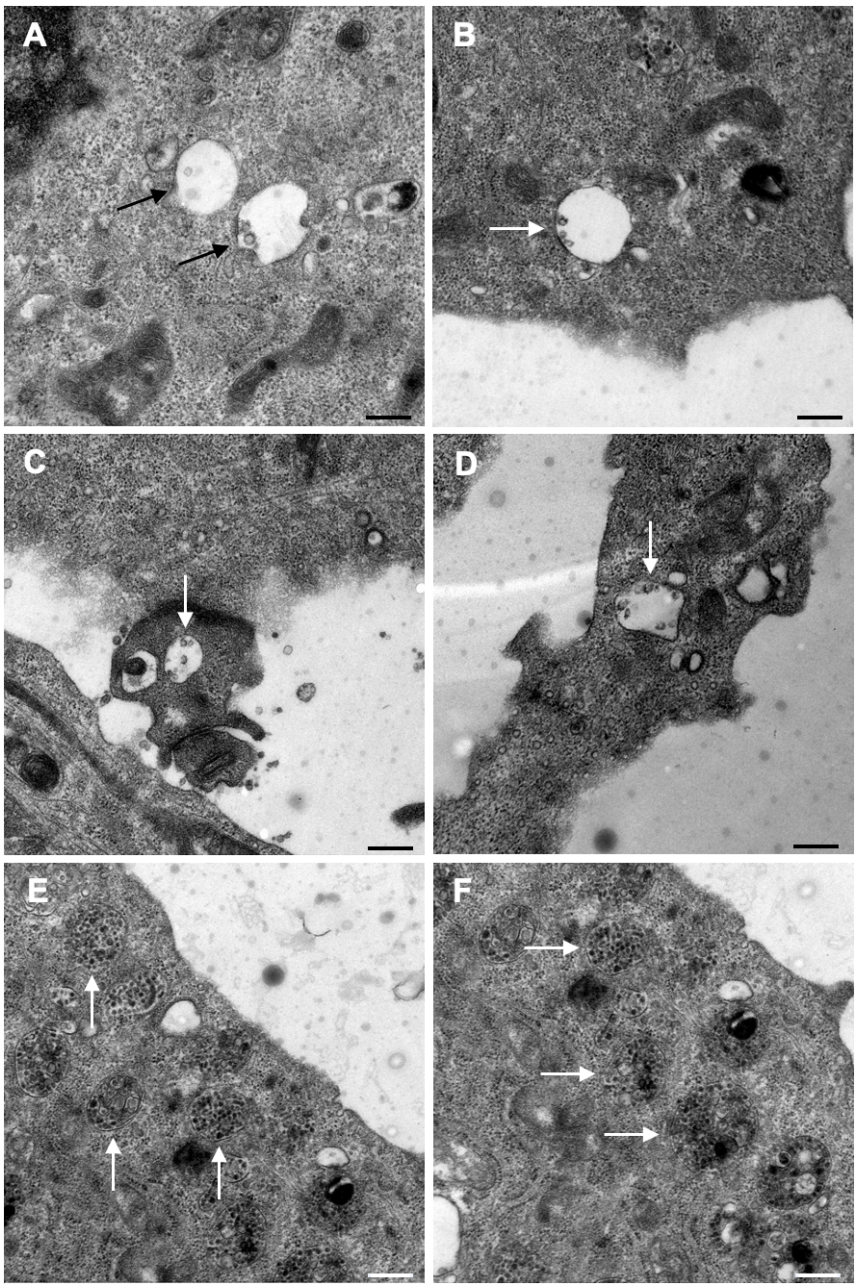

Fig. 28 Transmission electron micrographs of early endosome maturation to late endosomes/MVBs in serum-starved AoEnd cells. Pictured is the process of endosome maturation through ILV generation (A-D, arrows) and the generation of large MVBs (E-F, arrows). **Scale bars:** A-C: 250 nm, D: 100 nm, E-F: 250 nm.

Again, we screened the TEM-sections for the repeatedly described last steps of exosome biogenesis: MVBs traveling to the surface, fusing with the plasma

membrane and releasing the ILVs into the extracellular environment as exosomes (described and pictured in Akers et al., 2013 [16]). However, we found the afore-described novel occurrence: In serum-starved AoEnd cells, MVBs were incorporated into a new distinct cellular compartment first (Fig. 29). There, the MVB membrane dissolved and the exosomes were released within this compartment. Again, the fraction of the cell membrane at the apical end of this compartment facing the extracellular compartment consisted of fenestrated endothelium (Fig. 29, arrowheads). We could observe the characteristic properties of fenestrated endothelium: 60–80 nm diameter transcellular pores spanned by fenestral diaphragms (Fig. 29) [98].

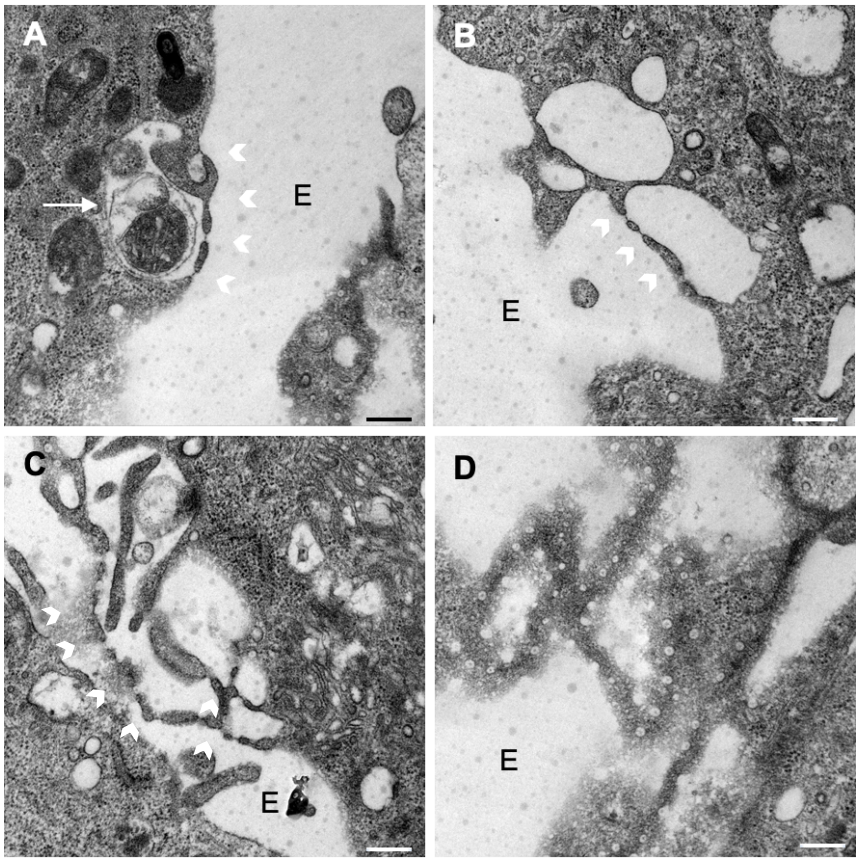

Fig. 29 Transmission electron micrographs of MVBs and exosomes in a "new cellular compartment". A: Pictured is a "new cellular compartment" containing the MVBs and their respective content, now free within this section. Also clearly visible is the fenestral endothelium with transcellular pores spanned by fenestral diagrams. **B-C:** "new cellular compartments" with fenestrated endothelium at their apical end. **D:** Fenestral endothelium "en face" to depict their characteristic radial diaphragm fibrils and a central knob. **Arrow:** "new cellular department". **Arrowheads:** fenestral endothelium. **E:** extracellular department **Scale bars:** A-D: 250 nm.

In some sections, we could identify the afore-described compartments lacking the apical membrane, possibly depicting the last step of exosome release (Fig. 30).

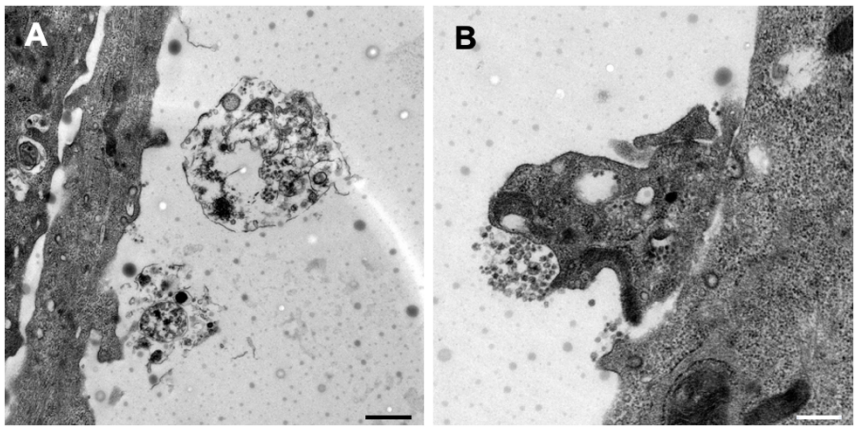

Fig. 30 Transmission electron micrographs of endothelial "compartments" and exosome release. Scale bars: A: 500 nm, B: 250 nm.

3.2 Detailed examination of the biogenesis of MVs produced under inflammatory stimuli using light and transmission electron microscopy

For all following experiments, we used cultured aortic endothelial cell (AoEnd) lines, as they stem from the macrovascular system and also showed better stability in terms of cell condition under serum starvation.

During cell cultivation under serum starvation, we additionally exposed one half of the cultured cells to LPS or TNF-α by injecting the respective stimulus into the cell medium; the other half was only subjected to serum starvation. TNF-α (tumor necrosis factor-α) is a proinflammatory cytokine that has been proven to induce both MV generation as well as endothelial activation and permeability during the development of atherosclerosis [16, 100].

The aim of this experiment was to analyse whether the inflammatory stimuli led to upregulated expression of vascular cell adhesion molecules on the endothelial cells' surface and more importantly, also on their produced MVs and exosomes. Vascular adhesion molecules play an important role in the development and

progression of atherosclerosis as they support the adhesion of activated lymphocytes to endothelium [101].

The experiment was conducted using ICAM-1, VCAM-1 and CD44 as primary antibodies, as it has been shown that their increased expression is a critical feature of atherosclerosis [101-103].

3.2.1 Light microscopic analysis of the abundance of vascular adhesion molecules on MVs produced under serum starvation and stimulation with TNF-α / LPS

The expression of vascular adhesion molecules was analysed in confluent AoEnd cells using WGATxRed-X and DAPI staining using CLSM. Expression of the respective molecules was shown as a green fluorescence.

ICAM-1

No substantial expression of ICAM-1 after 24h and 48h of cultivation under serum starvation or additional stimulation could be shown (Fig. 31, 32).

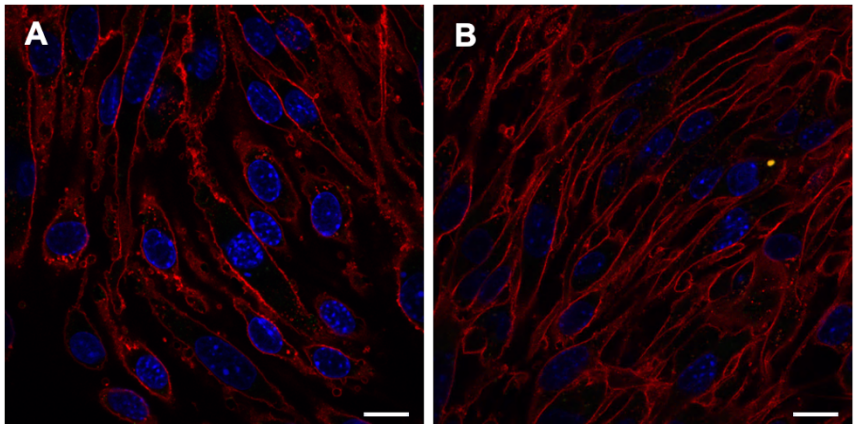

Fig. 31 AoEnd cells after 24 and 48 hours of serum starvation. Representative confocal images of AoEnd cells labelled with WGA-TxRed (red), DAPI (blue) and for ICAM-1 expression (green). A: AoEnd cells after 24h of serum starvation. **B:** AoEnd cells after 48h of serum starvation **Scale bar:** 10 µm.

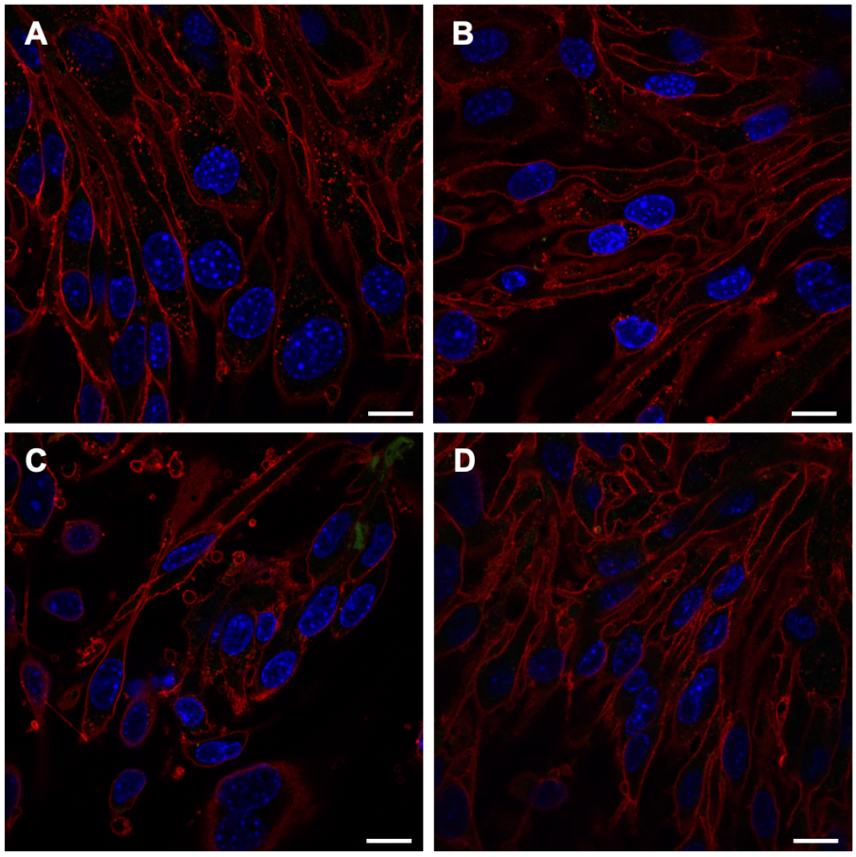

Fig. 32 AoEnd cells after 24 and 48 hours of serum starvation and stimulation with TNF-α / LPS. Representative confocal images of AoEnd cells labelled with WGA-TxRed (red), DAPI (blue) and for ICAM-1 expression (green). A: AoEnd cells after 24h of serum starvation and TNF-α stimulation. **B:** AoEnd cells after 24h of serum starvation and LPS stimulation. **C:** AoEnd cells after 48h of serum starvation and TNF-α stimulation. **D:** AoEnd cells after 48h of serum starvation and LPS stimulation. **Scale bar:** 10 µm.

VCAM-1

No substantial expression of VCAM-1 after 24h and 48h of cultivation under serum starvation or additional stimulation could be shown (Fig. 33, 34).

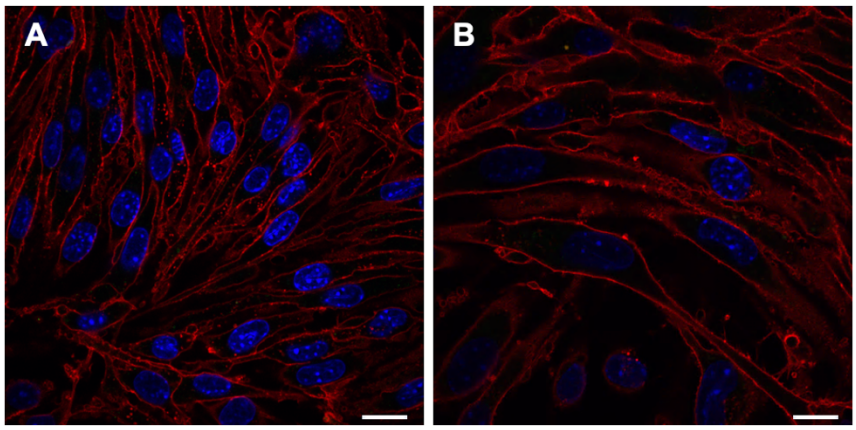

Fig. 33 AoEnd cells after 24 and 48 hours of serum starvation. Representative confocal images of AoEnd cells labelled with WGA-TxRed (red), DAPI (blue) and for VCAM-1 expression (green). A: AoEnd cells after 24h of serum starvation. **B:** AoEnd cells after 48h of serum starvation **Scale bar:** 10 µm.

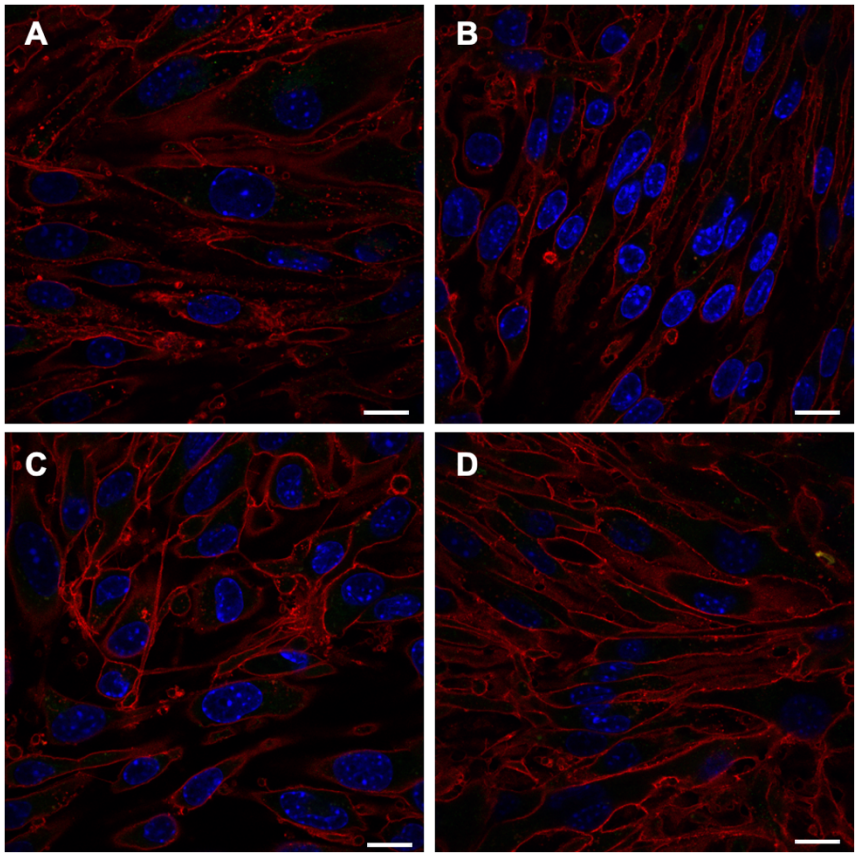

Fig. 34 AoEnd cells after 24 and 48 hours of serum starvation and stimulation with TNF-α / LPS. Representative confocal images of AoEnd cells labelled with WGA-TxRed (red), DAPI (blue) and for VCAM-1 expression (green). A: AoEnd cells after 24h of serum starvation and TNF-α stimulation. **B:** AoEnd cells after 24h of serum starvation and LPS stimulation. **C:** AoEnd cells after 48h of serum starvation and TNF-α stimulation. **D:** AoEnd cells after 48h of serum starvation and LPS stimulation. **Scale bar:** 10 µm.

CD44

No substantial expression of CD44 after 24h and 48h of cultivation under serum starvation or additional LPS stimulation could be shown (Fig. 35; Fig. 36, B+D).

However, after 24 and 48 hours of stimulation with TNF-α, the endothelial cells expressed the cell adhesion molecule CD44 in abundance, made visible by the bright green fluorescence signal all over the surface (Fig. 35, A+C).

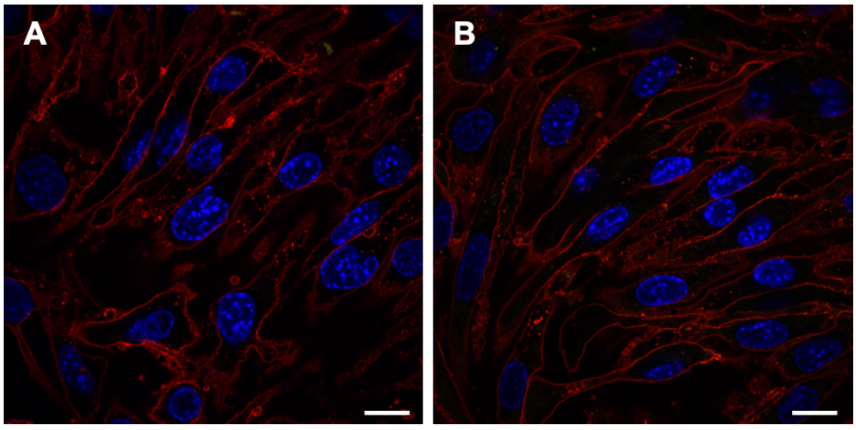

Fig. 35 AoEnd cells after 24 and 48 hours of serum starvation. Representative confocal images of AoEnd cells labelled with WGA-TxRed (red), DAPI (blue) and for CD44 expression (green). A: AoEnd cells after 24h of serum starvation. **B:** AoEnd cells after 48h of serum starvation **Scale bar:** 10 µm.

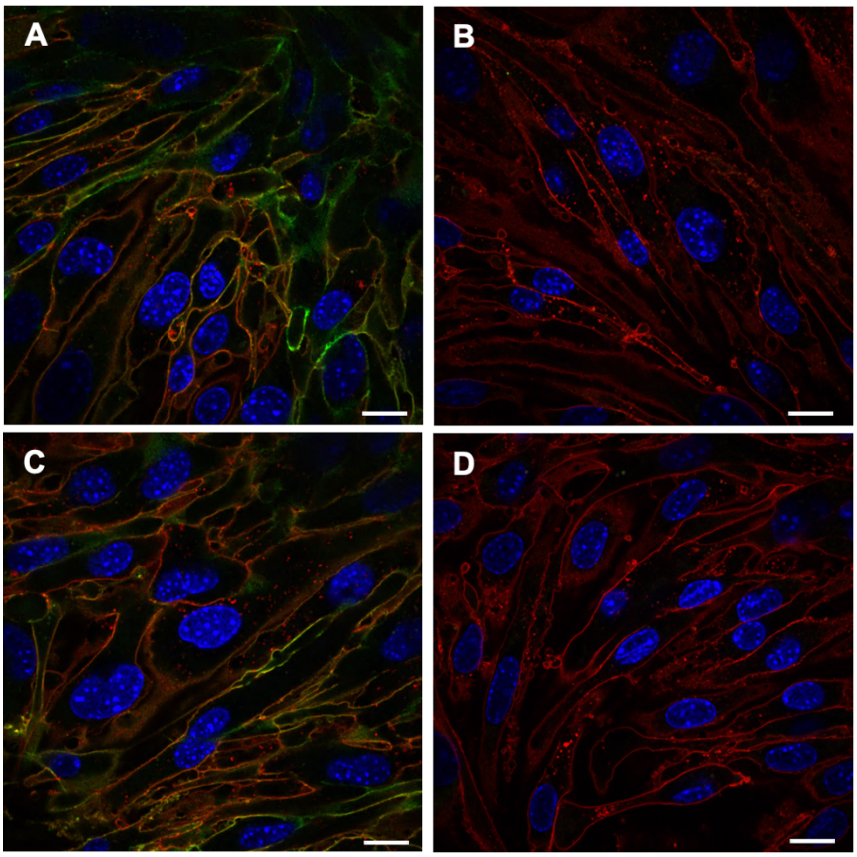

Fig. 36 AoEnd cells after 24 and 48 hours of serum starvation and stimulation with TNF-α / LPS. Representative confocal images of AoEnd cells labelled with WGA-TxRed (red), DAPI (blue) and for CD44 expression (green). A: AoEnd cells after 24h of serum starvation and TNF-α stimulation. **B:** AoEnd cells after 24h of serum starvation and LPS stimulation. **C:** AoEnd cells after 48h of serum starvation and TNF-α stimulation. **D:** AoEnd cells after 48h of serum starvation and LPS stimulation. **Scale bar:** 10 µm.

3.2.2 Light microscopic analysis of the abundance of vascular adhesion molecule CD44 on MVs produced under serum starvation and stimulation with TNF-α

To replicate and confirm the observation that after stimulation with TNF-α, the endothelial cells expressed and upregulated the adhesion molecule CD44, we repeated the experiment using TNF-α stimulation and CD44 staining only.

Indeed, as observed before, after a few hours of cultivation in the presence of the inflammatory stimulus TNF-α in the cell medium, the AoEnd cells universally

started to express and upregulate the adhesion molecule CD44 on their surface – visible as bright green fluorescence (Fig. 37, 38).

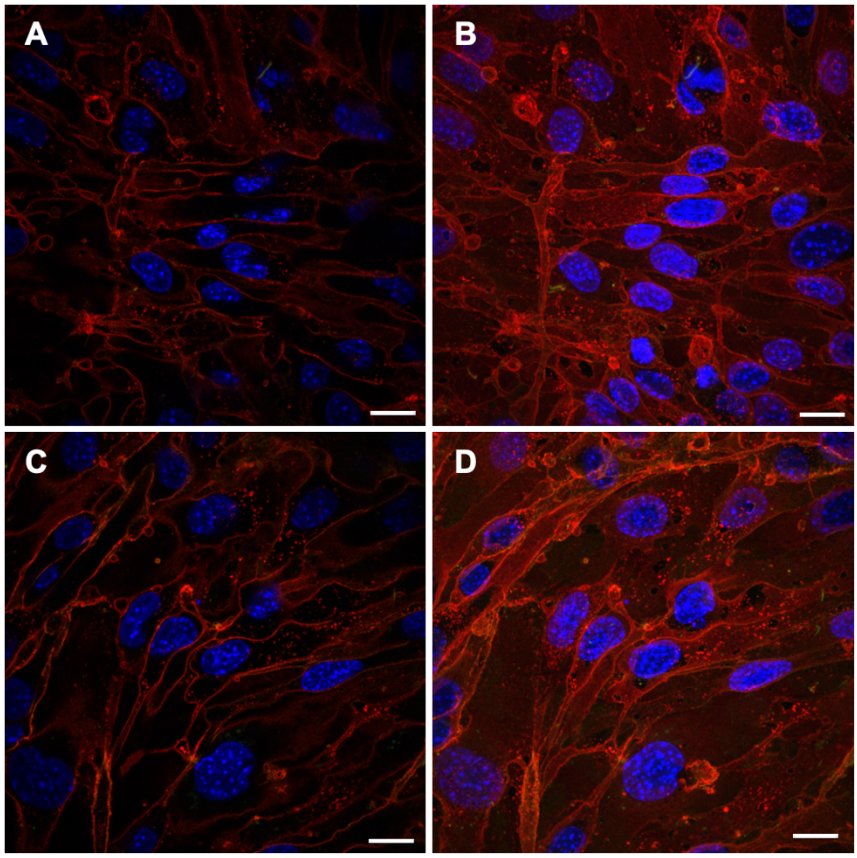

Fig. 37 AoEnd cells after 0 hours of serum starvation and stimulation with TNF-α. Representative confocal images of AoEnd cells labelled with WGA-TxRed (red), DAPI (blue) and for CD44 expression (green). A + C: WGATxRed-X, DAPI and staining for CD44. **B+D:** Maximum Intensity Projection. **Scale bar:** 10 µm.

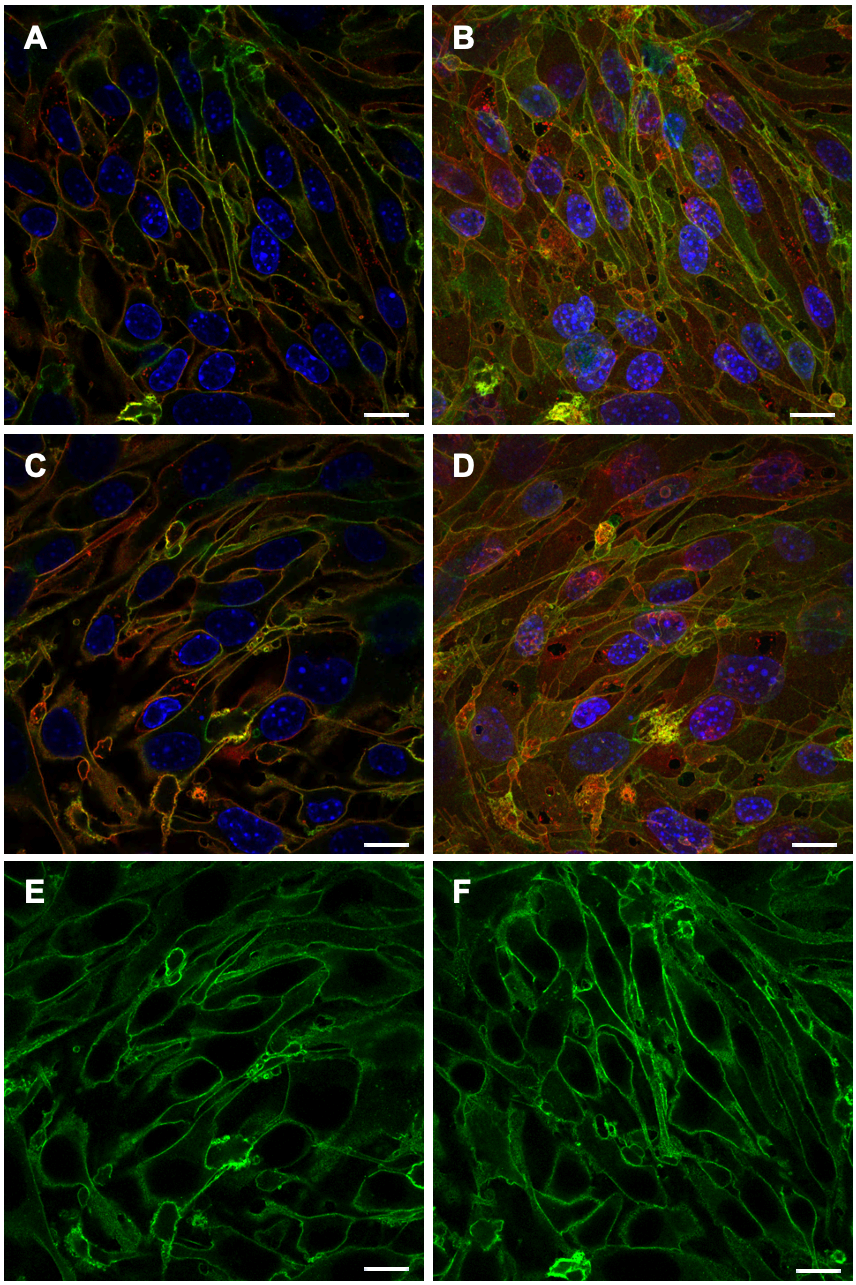

Fig. 38 AoEnd cells after 24 hours of serum starvation and stimulation with TNF-α. Representative confocal images of AoEnd cells labelled with WGA-TxRed (red), DAPI (blue) and for CD44 expression (green). A + C: WGATxRed-X, DAPI and staining for CD44. **B+D:** Maximum Intensity Projection. **E+F:** staining for CD44. **Scale bar:** 10 µm.

3.2.3 Immune electron microscopic analysis of CD44 abundance on MVs and exosomes after serum starvation and stimulation with TNF-α

After observing that TNF-α stimulation of serum-starved AoEnd cells caused them to significantly upregulate their CD44 expression on the cell surface, we turned to immunoelectron microscopy to analyse whether CD44 was transferred from the stimulated AoEnd cells to their produced MVs and/or exosomes. To visualize CD44 at the plasma membrane, we used pre-embedding Immunoperoxidase (DAB) staining with anti-CD44 as the primary antibody. CD44 abundance is visualized as dark electron-dense precipitates in the TEM images (Fig. 39, 40).

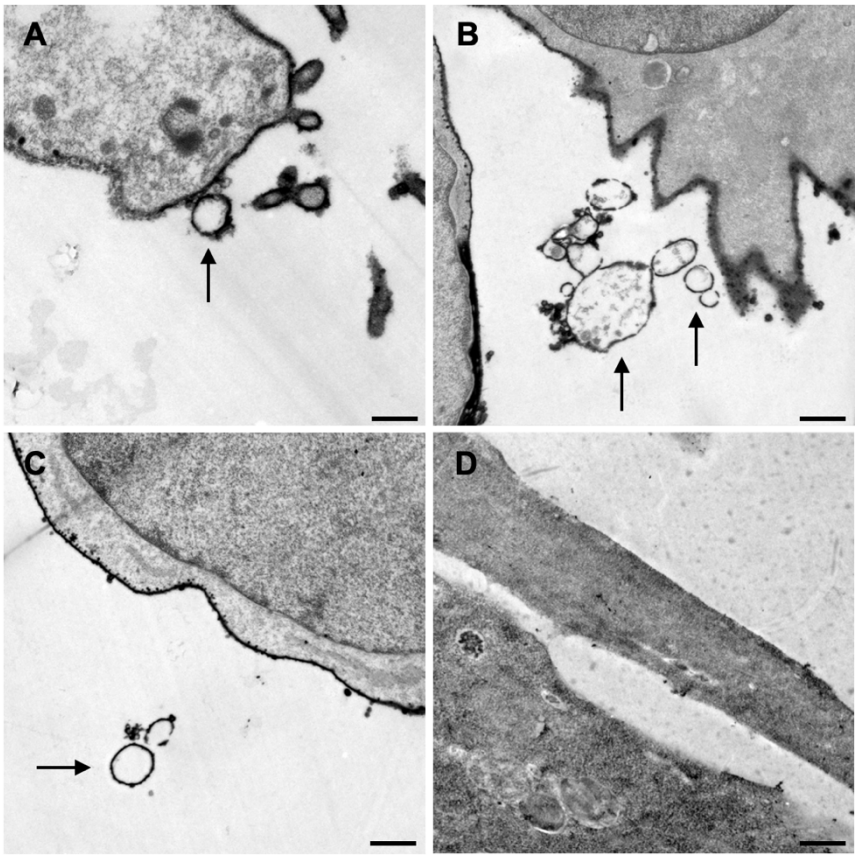

Fig. 39 Immune electron micrographs depicting the incorporation of CD44 into the plasma membrane of the AoEnd cells and their budding MVs (arrows). Immunoperoxidase (DAB) staining of 24 h serum-starved, TNF-α-stimulated AoEnd cells. D: Negative control. **Scale bars:** A: 250 nm, B-D: 1000 nm.

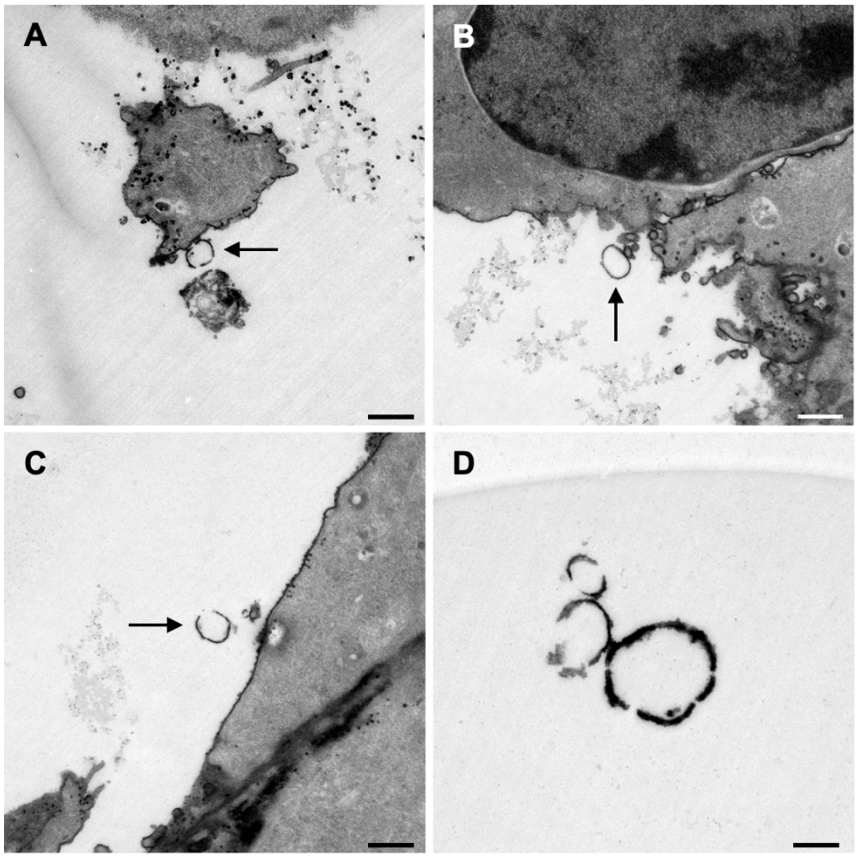

Fig. 40 Immune electron micrographs depicting the incorporation of CD44 into the plasma membrane of budding MVs (arrows). Immunoperoxidase (DAB) staining of 48 h serum-starved, TNF-α-stimulated AoEnd cells. Scale bars: A-C: 1000 nm, D: 250 nm.

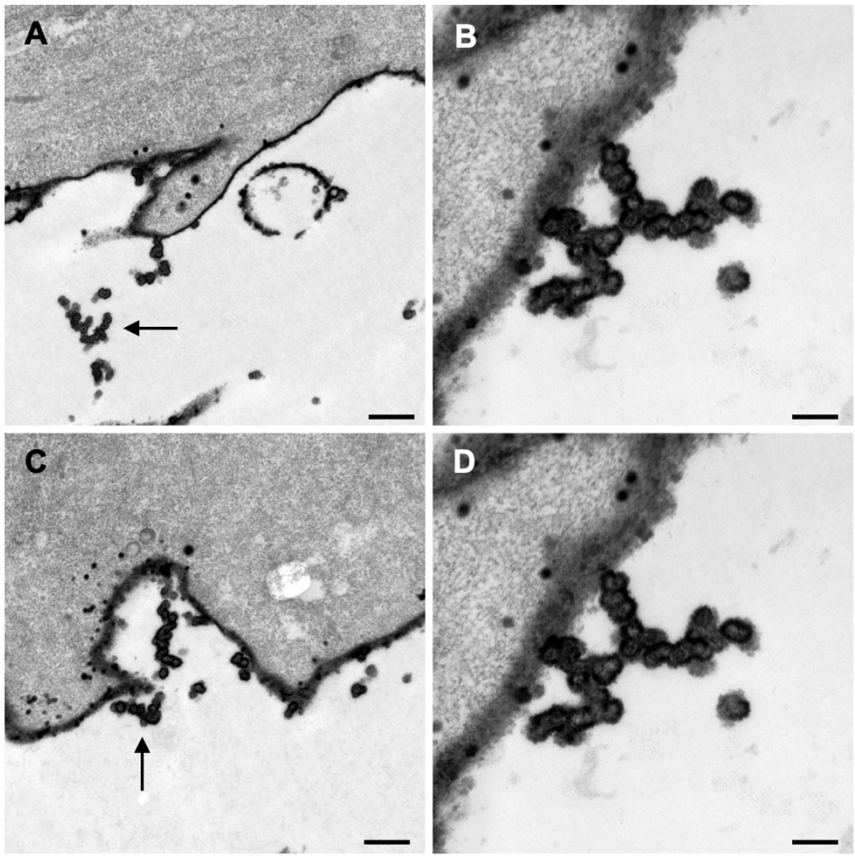

Fig. 41 Immune electron micrographs depicting the incorporation of CD44 into the plasma membrane of exosomes (arrows). Immunoperoxidase (DAB) staining of 24 h serum-starved, TNF-α-stimulated AoEnd cells. Scale bars: A: 250 nm, B: 100 nm, C: 250 nm, D: 100 nm.

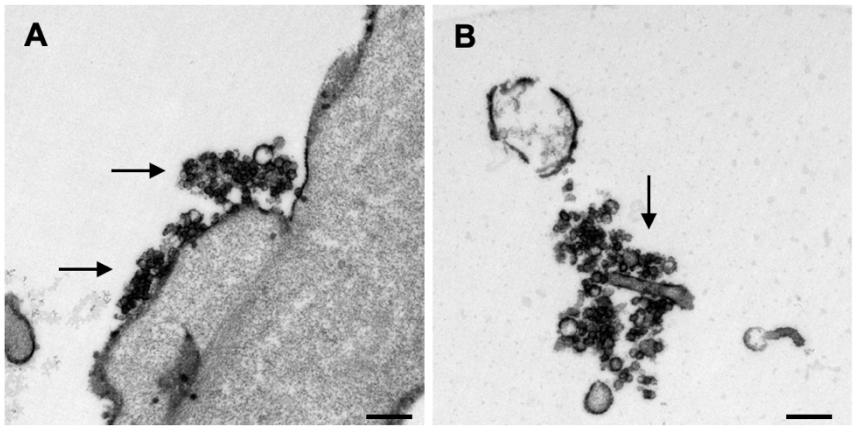

Fig. 42 Immune electron micrographs depicting the incorporation of CD44 into the plasma membrane of exosomes (arrows). Immunoperoxidase (DAB) staining of 48 h serum-starved, TNF-α-stimulated AoEnd cells. Scale bars: A-B: 250 nm.

As established before, we could identify the different EV classes best by their size and location: the MVs had an average size of 50–2,000 nm and were membrane-enclosed. They could be depicted in the extracellular environment, usually as a single vesicle, but at times together with a handful of other MVs, or during their budding process on the plasma membrane. Exosomes had an average size of 30–100 nm and were usually found densely concentrated in groups and close to the plasma membrane.

After identifying the EV classes, we focused on depicting all structures that were stained and therefore expressed the cell adhesion molecule CD44. As expected, the AoEnd cells showed the staining evenly all over their surface (Fig. 39, 40). The plasma membrane of all cells was stained, and we could not find any visible exceptions. The negative control ruled out a non-specific DAB signal and therefore false positive results (Fig. 39). Next, we examined the EVs and could observe that both MVs (Fig. 39, 40, arrows) and exosomes (Fig. 41, 42, arrows) showed the DAB staining at their plasma membrane, indicating that CD44 is incorporated into MVs and exosomes by serum starved, TNF-α-stimulated AoEnd cells – and could be transferred to target cells this way.

3.3 Examination of AoEnd cell- and EV-morphology by three-dimensional (3D) visualization with scanning electron microscopy (SEM) and serial block-face scanning electron microscopy (SBF-SEM)

To complete the detailed analysis of EV biogenesis, we applied SEM and SBF-SEM to allow its 3D visualization.

3.3.1 SBF-SEM of MV production by AoEnd cells under serum starvation and stimulation with TNF-α

Using SBF-SEM analysis (resolution of individual data sets: 10 nm x 10 nm x 30 nm), a 3D model of budding vesicles and their parental cells was created using the open-source platforms TrakEM2-ImageJ and Tomviz (Fig. 43). This technique allowed an exact morphological study of the budding process.

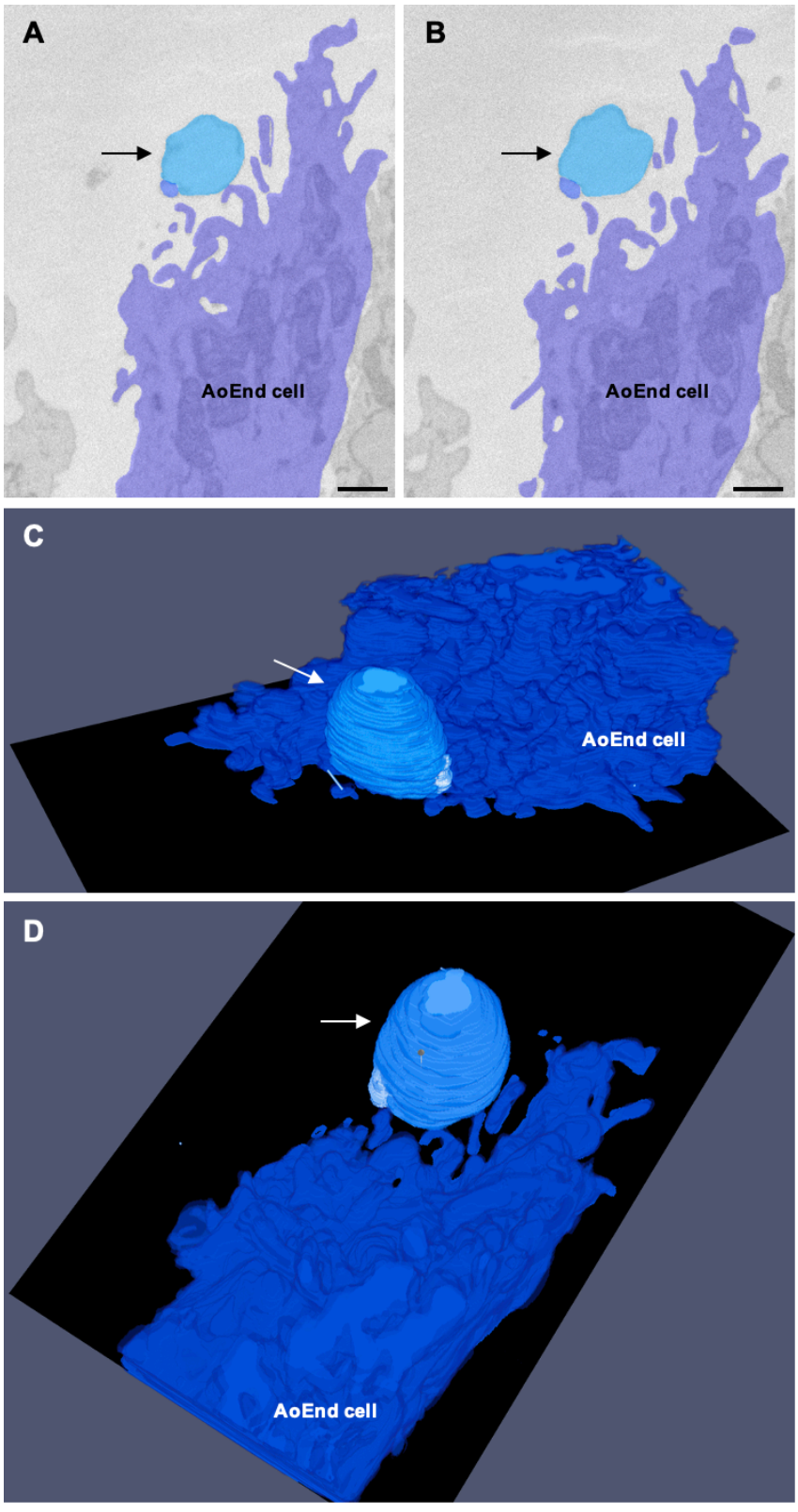

Fig. 43 Representative 3D rendering of budding MVs (arrows) by AoEnd cells under serum starvation and stimulation with TNF-α, depicted on 56 sections using TrakEM2-ImageJ (A-B) and Tomviz (C-D). Scale bar: A-B: 500 nm.

3.3.2 SEM of EV production by AoEnd cells under serum starvation and stimulation with TNF-α

We then turned to SEM to visualize processes taking place on the cells' surface. As SEM micrographs characteristically have a large depth of field providing a 3D appearance, this approach is very useful for understanding the surface structure of a sample and examining the processes occurring on the plasma membrane.

The scanning electron microscope's resolution limit of 1,0 nm also enabled us to clearly distinguish the three types of EVs produced by the AoEnd cells: the exosomes being the smallest vesicles with a size of 30–100 nm, MVs presenting as round blebs of 50–2,000 nm in size and the large apoptotic bodies being shed in various sizes ranging from 50–5,000 nm (Fig. 44).

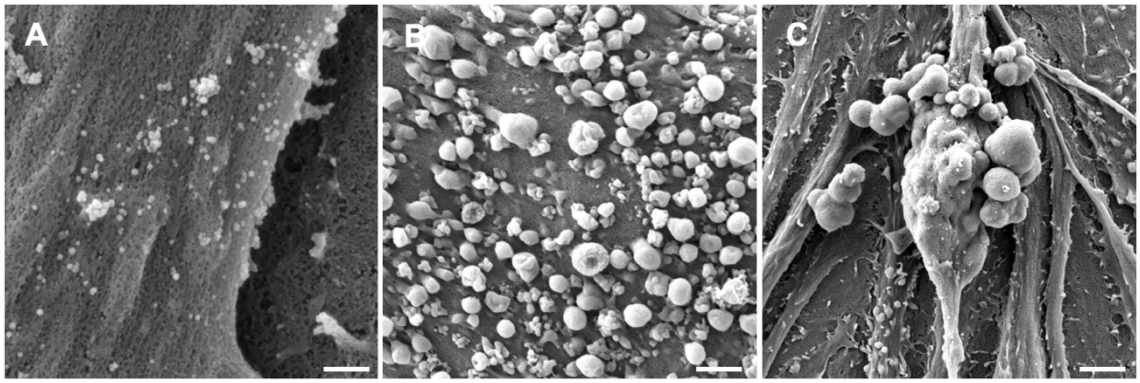

Fig. 44 Scanning electron micrographs depicting the three classes of EVs: Exosomes (A), Microvesicles (B) and Apoptotic bodies (C). Scale bars: A: 200 nm, B: 1 µm, C: 2 µm.

After identifying the three different EV classes, we analysed the different steps of EV biogenesis in AoEnd cells 0, 24 and 48 hours after cultivation under serum starvation and TNF-α stimulation.

In the CLSM images, individual serum-starved cells had shown small vesicular structures at the cell surface in a random distribution. These vesicular structures could have been interpreted as membrane-bound EVs that had pinched off from the MyEnds' plasma membrane, but likewise as simple cellular membrane protrusions that would also emit the red fluorescence signal. As a result of the

much higher resolution of the SEM, we could now determine the exact nature of these vesicular structures (Fig. 45). It became clear that the structures were not EVs, instead they rather represent either filopodium-like membrane protrusions expressed by active endothelial cells or endothelial cell primary cilia (sensory organelles that extend from the cell surface and sense extracellular signals such as blood flow-induced mechanical forces [100]) which can be promoted as a result of serum starvation [104].

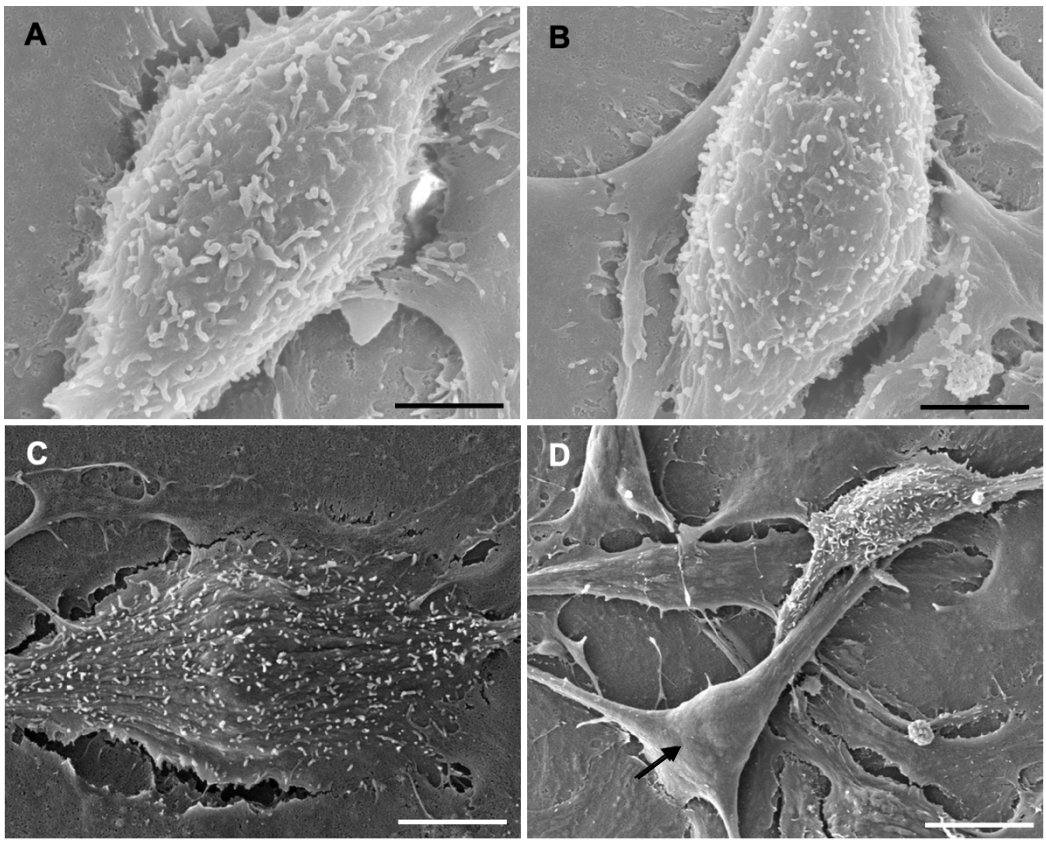

Fig. 45 Scanning electron micrographs depicting the membrane protrusions on AoEnd cells after 0 hours of serum starvation (A-C). D: "Inactive" AoEnd cell (arrow) not showing membrane protrusions**. Scale bars:** A-B: 2 µm, C: 2 µm, D: 5 µm.

Next, we focused on depicting MV biogenesis, especially the direct outward budding and vesicle formation of the plasma membrane (Fig. 46). The MVs, though each one unique looking, were recognizable by their generally round, plump vesicular shape and their size (ranging from around 100-1000 nm). As observed before, we could find the budding MVs on various parts all over the

cells' surface (Fig. 46, arrows); no preferred location of MV biogenesis could be detected. On some cells MVs could be found equally distributed all over the surface, on others they were found rather concentrated in one area. One interesting finding was that some cells – even though subjected to the same stimuli for the same time – were producing more vesicles than others.

We observed that MV production increased the longer the AoEnd cells were subjected to serum starvation and TNF-α stimulation (Fig. 47, 48). We later performed a statistical analysis corroborating this observation (Fig. 51). However, some cells remained completely inactive and did not produce any MVs over the entire time.

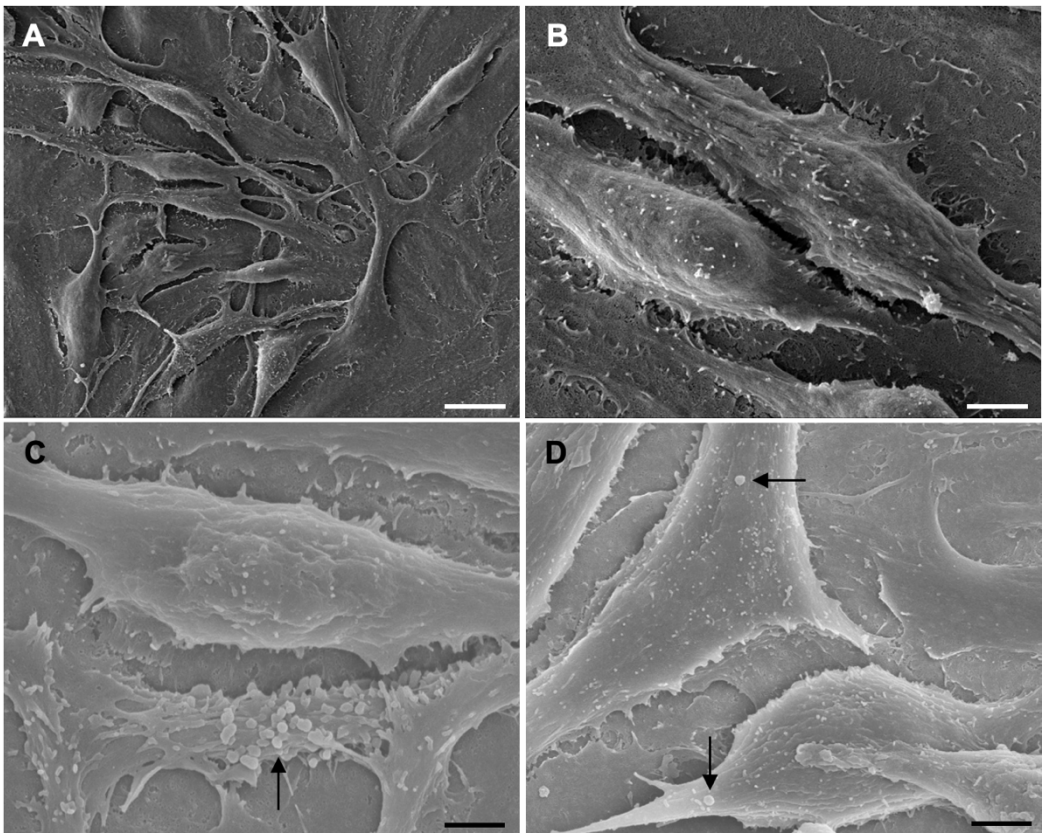

Fig. 46 Scanning electron micrographs of AoEnd cells after 0 hours of serum starvation. Arrows: Budding MVs on the surface. **Scale bars:** A: 10 µm, B-D: 2 µm.

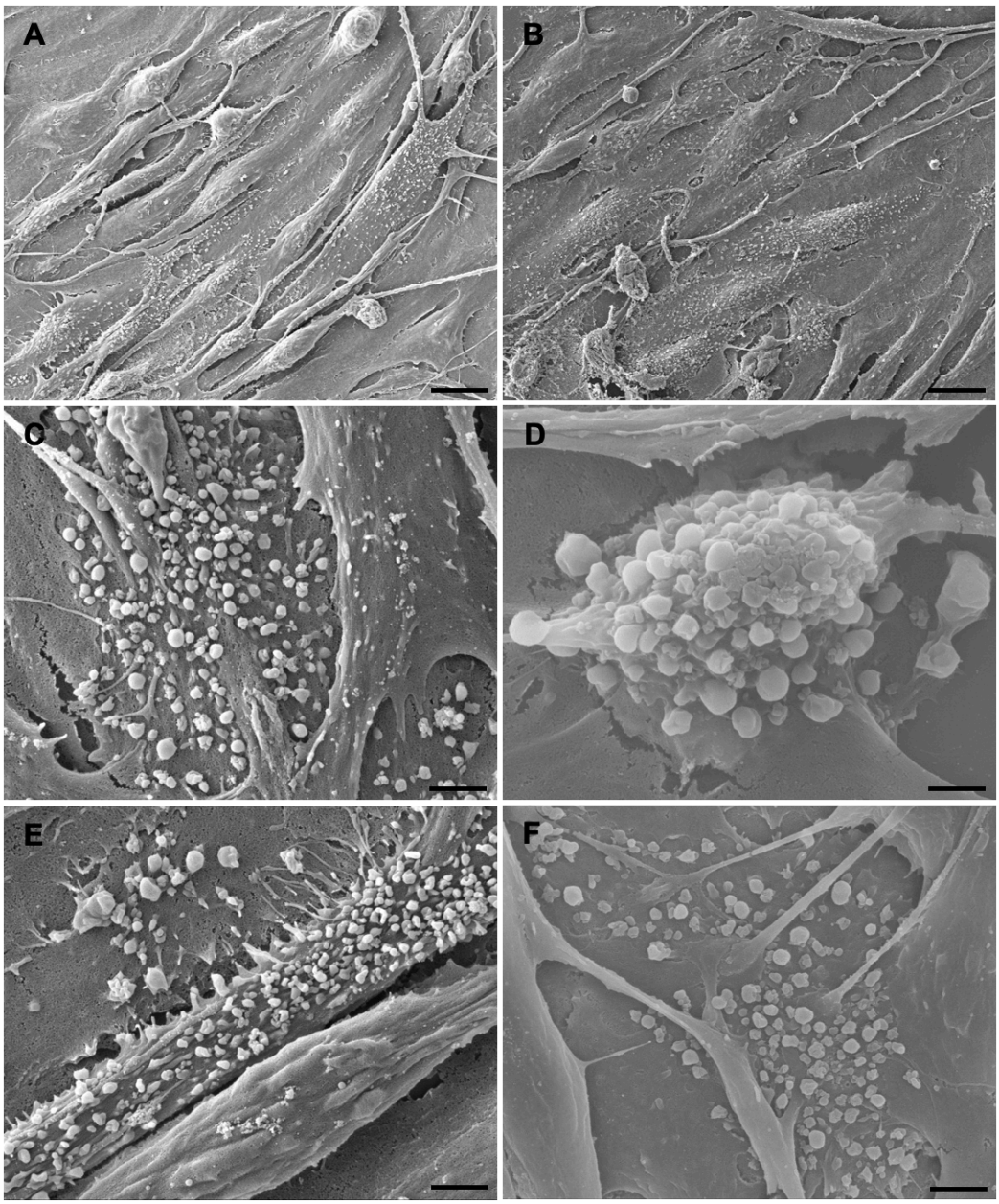

Fig. 47 Scanning electron micrographs of AoEnd cells after 24 hours of serum starvation and stimulation with TNF-α. MVs on the cell surface pictured as generally round, plump vesicles of 100-1000 nm in size. **Scale bars:** A-B: 10 µm, C: 2 µm, D: 1 µm, E: 2 µm, F: 2 µm.

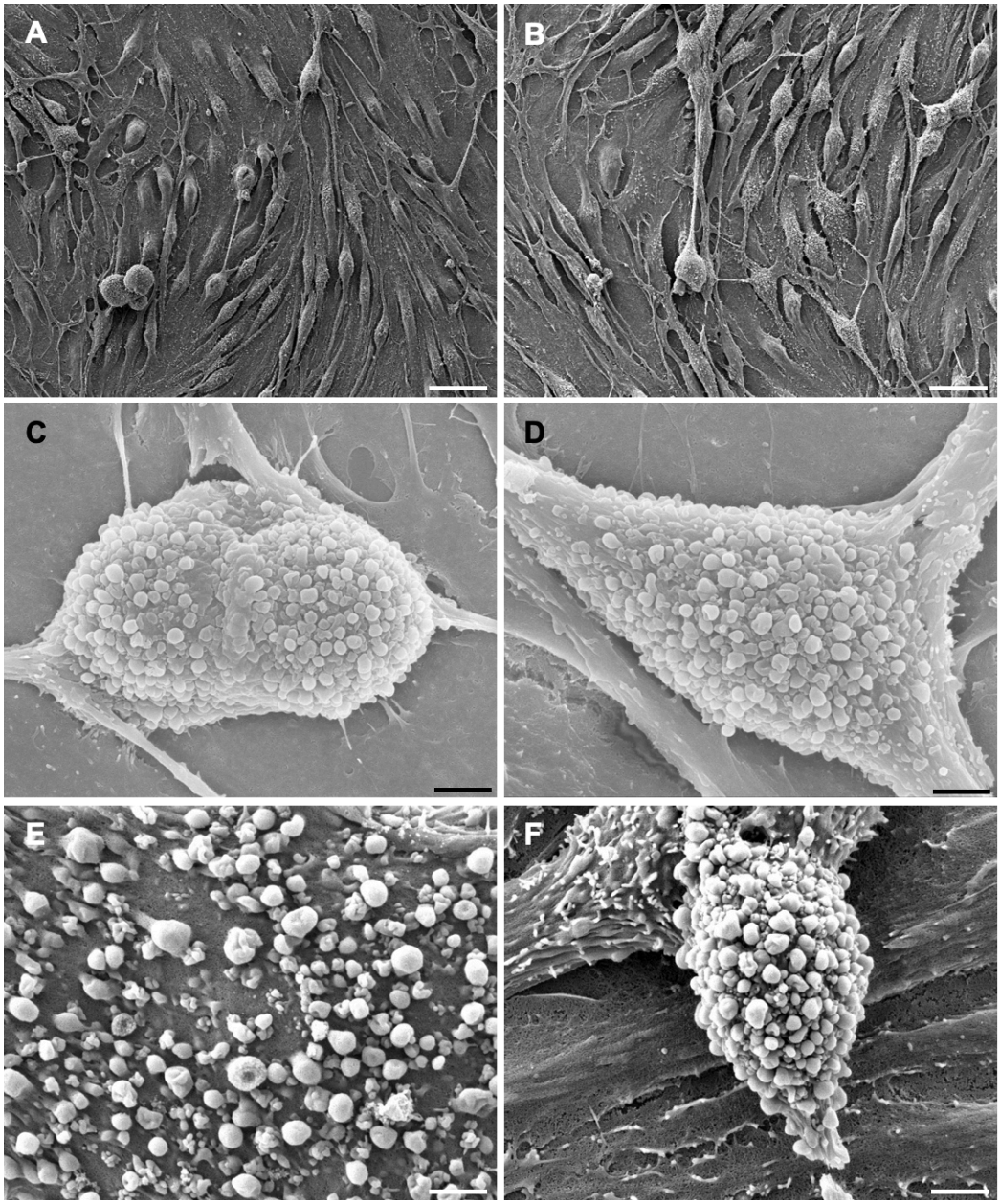

Fig. 48 Scanning electron micrographs of AoEnd cells after 48 hours of serum starvation and stimulation with TNF-α. MVs on the cell surface pictured as generally round, plump vesicles of 100-1000 nm in size. **Scale bars:** A-B: 10 µm, C-E: 2 µm, F: 2 µm.

Next, we analysed exosome biogenesis. As a big part of the exosome biogenesis – the formation of early endosomes through endocytosis, their maturation into late endosomes /MVBs [97] – happens intracellular, we could only observe the exosomes once they had been released by the cell. The round exosomes were

distinguishable by their small size of about 30–100 nm and were usually found densely concentrated in groups and close to the plasma membrane (Fig. 49).

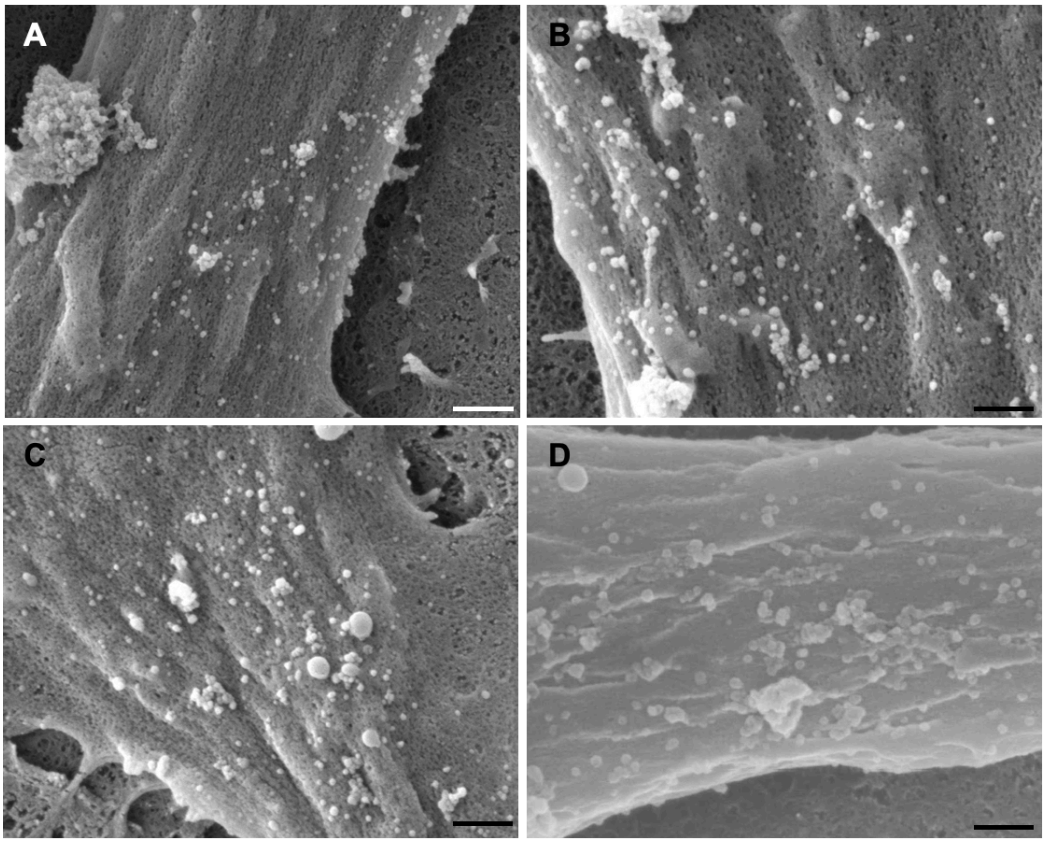

Fig. 49 Scanning electron micrographs of AoEnd cells after 24 hours of serum starvation and stimulation with TNF-α. Exosomes are visible on the plasma membrane as round vesicles of 30–100 nm in size, usually concentrated in groups. **Scale bars:** A: 1 µm, B-C: 200 nm, D: 1 µm.

We also tried to examine the exact mechanism of exosome release: According to literature, MVBs travel to the surface, fuse with the plasma membrane and then release the ILVs into the extracellular environment as exosomes [16]. We could find and depict recently released exosomes relatively easy (see above) – however, capturing the exact moment of the release proved to be difficult. On several locations, we could depict a small, crater like structure on the plasma membrane – which could be interpreted as the site, where the MVBs had fused with the membrane to release exosomes (Fig. 50, arrows). However, since all cell

probes were sputter coated with a 20 nm coating of gold during preparation for the SEM, it was not possible to depict any further details.

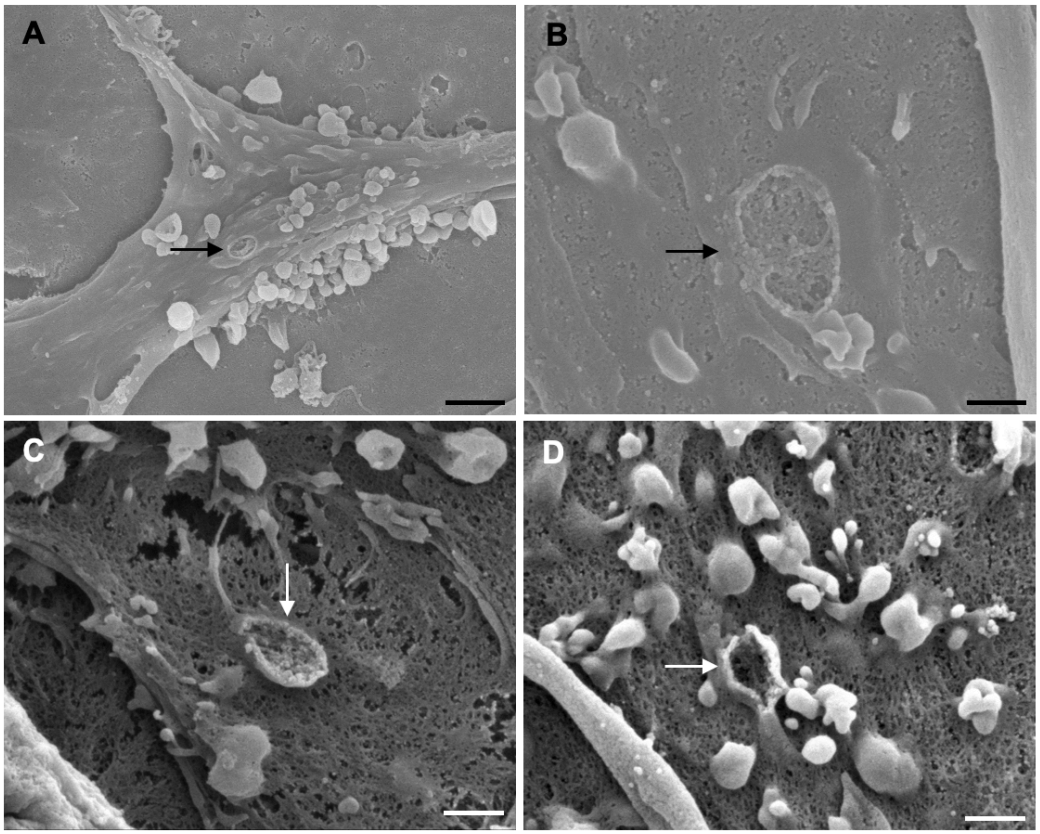

Fig. 50 Scanning electron micrographs of possible MVB-fusion with the plasma membrane on AoEnd cells after 24 (A) and 48 (B-D) hours of serum starvation and stimulation with TNF-α. Arrows: Crater-like structure on the plasma membrane – which could be interpreted as the site, where the MVBs had fused with the membrane to release exosomes. **Scale bars:** A: 1 µm, B: 200 nm, C: 300 nm, D: 200 nm.

Since SEM with its high resolution allowed such a detailed examination of AoEnd cells and the processes occurring on their surface, we decided to perform a statistical analysis to determine how serum starvation and TNF-α stimulation influenced the AoEnd regarding cell activation and MV production.

For the analysis, we divided the AoEnd cells between three groups: 1. Cells that were “inactive” and therefore did not show any activity or noticeable

morphological change on their surface, 2. Cells that were “active”, meaning they showed various membrane protrusions (as described under 3.3.2), but no remarkable EV production, and 3. Cells that were producing MVs and exosomes. We compared the number of these three groups with each other as well as in relation to the time under starvation and TNF-α stimulation.

To begin with, we performed the Shapiro-Wilk test [7], which showed that the data were not normally distributed. Therefore, Mann-Whitney U tests and the Kruskal-Wallis H-Test for one-way Analysis of Variance (ANOVA) were used for pairwise and global between-group comparisons, respectively. When multiple tests of one kind were performed within a single experiment, we corrected the observed p-values by a Bonferroni post hoc test.

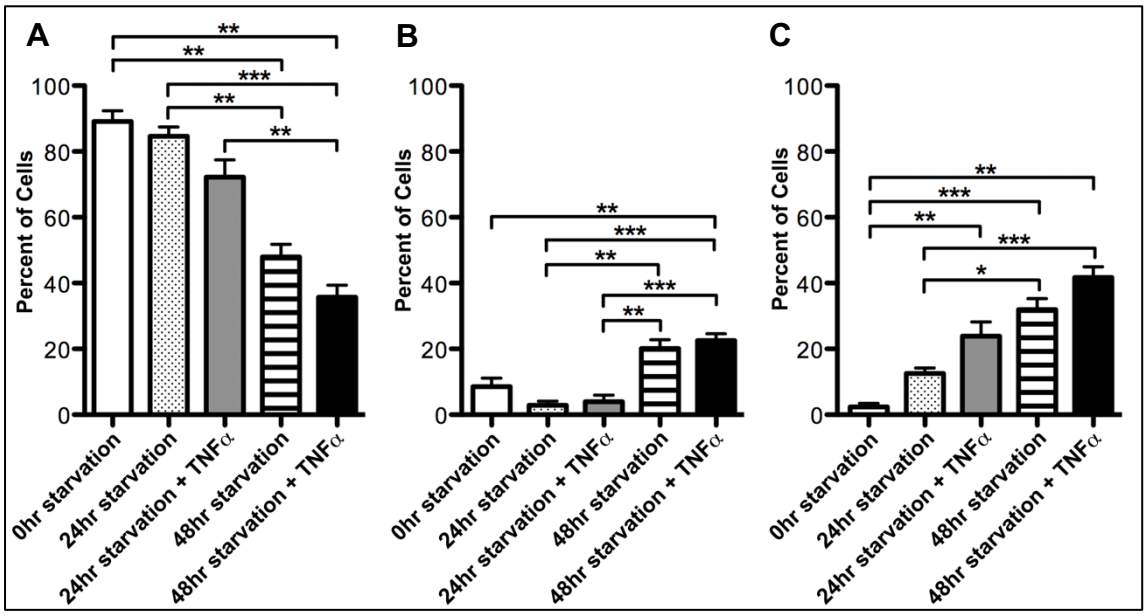

Fig. 51 Statistical analysis of the number of “inactive” AoEnd cells (A), “active” AoEnd cells (B) and EV-producing AoEnd cells (C) in relation to the time under starvation and/or TNF-α stimulation.

Data are reported as bar graphs including a standard error bar. P levels are indicated as *P<0.05, **P<0.01, or ***P<0.001. A value of P<0.05 was considered as statistically significant.

The statistical analysis showed that the more time the AoEnd cells spent in cultivation under starvation (with or without additional TNF-α stimulation), the higher the percentage of active and EV producing cells (Fig. 51).

However, additional TNF-α stimulation induced a significantly higher MV production in AoEnd cells than serum starvation alone (Fig. 51). It seemed to be the deciding factor in generating the highest number of MVs. However, in both serum starvation and serum starvation plus TNF-α stimulation, there was a number of inactive cells at all times.

4. Discussion

As described in the introduction, it is essential to establish standardised and reproducible techniques for the in vitro study of EVs. To do so, we compared different study methods and in the following give recommendations concerning their validity and usefulness – especially focusing on three topics: the microscopic approach for cell and EV examination, the conditions of cell cultivation and the best approach to generate EVs with a high quantity and quality for further functional studies.

4.1 Establishing test standards for the in vitro study of EVs

4.1.1 Direct comparison of light and electron microscopic methods for the morphological characterization of EVs

The in vitro imaging of EVs plays a highly important role in allowing an understanding of the procedure of EV biogenesis and release as well as its effects on the producing cell. To be able to draw reliable conclusions from the microscopic findings, it requires methods that successfully depict EVs, but do not disturb the vesicles' native morphology. With this study, we provide a detailed comparison of different microscopic approaches in the morphological

characterization of EVs and evaluate their respective strengths and disadvantages.

Light microscopy: Confocal Laser Scanning Microscopy (CLSM)

The commonly used light microscopic approach for the study of EVs is CLSM. CLSM is a widely used fluorescence microscopic tool for three-dimensional structural studies of biological cells and tissues [105]. Its primary value is its ability to produce a stack of optical sections through a three-dimensional specimen. While moving the focal plane of the instrument through the depth of the specimen (in defined steps of µm-range), the computer-controlled CLSM simultaneously produces digital images at near video rates [105]. These are immediately available for image analysis and processing, and can also be used to compute surface- or volume-rendered 3D reconstructions of the specimen [106]. The biggest advantage of the CLSM is therefore its depth-discriminating property and three-dimensional reconstruction function, enabling a quick and highly accurate analysis of the spatial structure of materials [105]. It indeed proved to be very effective in providing a first impression and overview of the MyEnd and AoEnd cells' morphological condition as well as a first assessment of a possible production of EVs.

Another advantage is that in comparison to electron microscopic approaches, only a few preparatory steps are necessary for viewing a specimen by CLSM. The specimen has to be fixed and the component of interest in the sample must be labelled with fluorescent dyes [106]. This does not require more than a few hours of preparation time, which is a big contrast to the lengthy embedding process needed for electron microscopy. The number of used materials and the methods of preparing the sample are also very manageable and do not require expertise in the field.

The big disadvantage of CLSM that we could observe was its limited resolution. The best available resolution is 180 nm in XY and 500 nm in Z [107]. As MVs with a size of 100 nm - 1 µm and exosomes with a size 30 - 100 nm are very close to

or mostly under the resolution limit [31], CLSM didn't allow us to make clear statements about the number or morphology of the EVs. Smaller MVs as well as all exosomes were simply not depictable. Due to the limited resolution, there was also confusion about how to interpret certain fluorescent vesicular structures on the cell surfaces – in the SEM images, some turned out to be cellular protrusions, not EVs, but we could not determine that with the CLSM images alone.

Overall, the CLSM is very useful for a quickly and easily preparable overview over the cultivated cell's condition – including the state of the cell-cell contacts, made visible by WGA-TxRed staining of the glycocalyx. Big apoptotic bodies (50 nm–2 µm [31]) are also visible and can give further hints about the cells' condition. However, to be able to measure the amount of produced EVs, depict their exact size, shape and morphology and divide them into the different classes, electron microscopy must be employed.

Electron microscopy

Electron microscopy has been established as a standard imaging method for examining nanosized samples, including EVs [108]. With a resolution typically around 1 nm (even less in high-resolution microscopes), it is able to provide detailed structural information of all classes of EVs [109]. Processes on the cell surface as well as the characterization of both size and morphology of individual vesicles are made possible through the high resolution. However, all samples need to be chemically fixed, dehydrated or otherwise processed prior to imaging, which often introduces artefacts such as precipitates [110].

There are different electron microscopic methods used for EV imaging that we will discuss in the following.

Transmission Electron Microscopy (TEM)

As the TEM uses electron beams that pass through the specimen (prepared as ultra-thin tissue slices), it allows a detailed analysis of cellular and subcellular components, which is one of its biggest advantages. The composition and

organization of the cell content (cytoplasm, cytoskeleton, cell organelles) could be visualized at the ultrastructural level. In addition, processes occurring on the plasma membrane including EV release could be visualized as such. The TEM is also widely valued for its capability to detect and characterize single EVs by their typical size, morphology and biogenesis – therefore allowing a clear allocation of the respective vesicles to their EV class [109]. In addition, Immuno-TEM is “one of the best methods for detecting and localizing proteins in cells and tissues”, as De Paul et al. state [111]. Proteins of interest are labelled with specific antibodies and at the site of the antigen-antibody reaction, an electron-dense mark is created which can subsequently be picked up by the TEM. This high-resolution technique allows the localization and visualization of the proteins at an ultrastructural level. In this study, Immuno-TEM was used to depict the transfer of cell adhesion molecule CD44 by MVs and exosomes.
However, next to a complex chemical preparation of samples for TEM imaging, the samples must be embedded, sliced into nanometre-thin sections, and mounted on a carbon coating grid for imaging [108]. The whole procedure, as described in the Material and Methods section, usually takes a minimum of four days. Also, the reagents used for fixation and contrasting procedures are highly toxic. In comparison to other approaches, TEM imaging therefore requires the longest and most complex preparation.

Serial block-face scanning electron microscopy (SBF-SEM)

Using SBF-SEM analysis enables the creation of a digital 3D model of examined specimen. We used a resolution of individual data sets of 10 nm x 10 nm x 30 nm. The serial sectioning technique of the SBF-SEM helps to understand the detailed 3D structure of EVs and allows a morphological study of the budding process and the parental cells. As the cell probes (embedded in resin) are securely mounted on aluminum pins directly inside the SEM, thousands of serial images can be obtained without folding, distortion, or loss of sections [112]. However, the alignment and subsequent segmentation of the numerous SBF-SEM images is a very meticulous and time-consuming work.

Scanning electron microscopy (SEM)

The SEM detects electron beams that are deflected by the surface of specimen that have been sputter-coated with a thin layer of conductive material such as gold. It is therefore used to scan the surface of specimen and to subsequently generate topography information [108]. Views of the cell content are not possible. As the SEM has a resolution limit of around 1,0 nm, it provides excellent 3D images of the surface structure of a sample. It captures all processes occurring on the plasma membrane due to its large depth of field, such as cellular protrusions or budding vesicles of all kinds. As opposed to the CLSM images, there is no confusion of the nature of certain processes on the surface. The images allow the classification of single EVs by their typical size and morphology. Additionally, as the cells are visible as a whole – as opposed to TEM – it enabled us to conduct statistical analyses of the behaviour of a big group of cells, for example regarding cell activation and MV production.

The preparation of samples for conventional SEM is relatively simple when compared to that of TEM, however, it too entails chemical fixation and dehydration, possibly causing artefacts. The sample preparation for SEM also requires the surface of the specimen being sputter coated with a thin conductive layer (we used 20 nm of gold). This thin layer usually does not affect the imaging result, however, as EVs are very small, it may actually affect their surface structure after all, as Chuo et al. report [108].

To summarise, our results show that there is no single specific microscopic approach that can provide a comprehensive analysis of cell and EV morphology. The limitations and disadvantages of one technique, however, can be compensated by the qualities of the respective other described techniques. This conclusion is congruent with the opinion of other research groups, that also compared imaging methods for EV visualization, such as Chuo et al. [108], Noble et al. [110] and Choi et al. [112].

We recommend to always combine several microscopic approaches for the best possible results. The CLSM is very useful in giving a quick overview over the cell's morphological condition but cannot be used for the study of EVs.

The optimal electron microscopic approach depends on the aim of the study:

TEM imaging is best for the examination of the composition and organization of the cell content and the visualization of processes occurring on the plasma membrane. It also allows an excellent study of EV biogenesis and the depiction of single EVs and their typical size and morphology. Furthermore, by using Immuno-TEM, specific proteins of interest can be located and visualized in their ultrastructural context. However, the study of a whole group of cells and/or statistical analyses are not possible.

The serial sectioning technique of the SBF-SEM provides the possibility to generate a digital 3D model of the EVs' budding process and the parental cells. However, a detailed visualization of single EVs (as provided by TEM or SEM) is not possible.

SEM imaging provides high-resolution 3D images of the surface structure of cells and allows the classification of single EVs by their typical size and morphology. Additionally, statistical analyses of the behaviour of a big group of cells are possible. However, it doesn't enable a view inside the cell.

4.1.2 The effect of serum starvation on the condition of cultivated endothelial cells and produced EVs

Serum starvation is performed by depleting the medium of cultivated cells in vitro of serum. Some authors also count a very low serum concentration (in relation to normal growth medium, typically 0.1 – 0.5%) as serum starvation [113]. The serum – one frequently used product is FBS, which we also used – contains certain nutritional and macromolecular growth factors that facilitate cell growth [51]. Serum starvation is one of the most frequently performed procedures in molecular biology and there is an abundant number of research papers reporting

its use [113]. It is also commonly used in tests with the aim of isolating EVs from cell culture supernatants – these isolated vesicles are then examined further. To make sure that the isolated vesicles actually derive from the cultured cells and are not contaminated by FBS exosomes, the medium has to be depleted of serum. Therefore, many authors, such as Théry et al., simply cultivate the cells in the absence of serum [114]. EVs are usually isolated after 48 - 72 hours of cultivation to ensure a decent quantity in the medium (for exemplary protocols see [115, 116]).

However, even though this method is so frequently used, it has not been fully examined in which ways serum starvation really influences endothelial cells during cultivation. Furthermore, it is unclear if and how the quality and quantity of the cell derived EVs changes in 72 hours under serum starvation. To answer these questions, we cultivated both MyEnd and AoEnd cells under serum starvation and examined their morphology at different time points with CLSM and TEM.

Serum starvation and cell condition during cultivation

Our CLSM results show that after 48 hours under serum starvation, the condition of the MyEnd cells notably changed for the worse. The cells not only began to look frail and damaged, they also started to lose their cell-cell contacts. This was proven by the usually straight-lined WGA-TxRed staining now meandering with gaps. Noticeable too was the presence of a large number of apoptotic bodies.

After 72 hours of serum starvation, the cells were evidently deteriorating and had completely lost their cell-cell-contacts. Gaping holes in between the cells and in the cells' cytoplasm were clearly visible. The number of cells producing apoptotic bodies had further increased after 72 hours under serum starvation.

However, the AoEnd cells remained in a physiological and healthy state throughout the whole cultivation period.

The TEM results corroborated our first observations. After 72 hours of cultivation under serum starvation, the MyEnd cells were indeed visibly deteriorating – the cytoplasm displayed gaping holes and the cell content had lost its physiological composition. Furthermore, the cells showed a great abundance of big MVBs and unusually large cisterns of the rER. Both observations could be indicators of an impaired endosomal-lysosomal degradation pathway. Additionally, we couldn't detect any caveolae on the cell's luminal surface. As endothelial cells are among the richest in caveolae, a lack thereof was a striking find adding to the appearance of a cell losing its physiological function.

Regarding the state of the AoEnd cells, we could not observe any morphological abnormalities with the TEM either.

All in all, it was evident that the MyEnd cells cultivated under serum starvation for at least 48 hours were not in a physiological and healthy state anymore. This can be explained by several reasons. Pirkmajer et al. state that serum starvation reduces basal cellular activity and induces apoptosis in various cells [113]. The latter phenomenon has been studied by several other authors who all come to the same conclusion – that serum starvation is one of the major stimulants of apoptosis [117-119]. One of our observations was that the cells were producing high numbers of apoptotic bodies (its numbers started to rise after 48 hours of serum starvation): per definition, apoptotic bodies are released specifically by cells undergoing apoptosis [40]. All things considered, we conclude that after 48 hours of cultivation under serum starvation, the MyEnd cells began to go through apoptosis.

Now the question arises whether EVs that are produced by these apoptotic cells should really be considered for further examinations and functional tests. As Pirkmajer et al. put it: "Serum starvation clearly represents a major event that triggers a plethora of divergent responses and has therefore great potential to interfere with the experimental results and affect subsequent conclusions" [113]. Endothelial cells that, due to apoptotic processes, show the unhealthy features that we observed – gaping holes in the cytoplasm, no cell-cell-contacts, abundant MVBs, unusually large rER cisterns and no caveolae – have a completely

different cell homeostasis than the cells at the beginning of cultivation. It is logical that the apoptotic cells express different mechanisms and signaling pathways than healthy, physiological cells. As Yáñez-Mó et al. state, the EV content reflects the type and functional state of parental cells and determines their different effects on the target cells depending on the composition [120]. Therefore, it is doubtful that conclusions drawn from these isolated EVs can be applied to studies of, for instance, physiological circumstances in the human body. They only have validity if the purpose of the study is to research the behavior of EVs under cell stress or cell apoptosis.

We therefore give novel recommendations when cultivating cells under serum starvation for the purpose of later isolating and examining their produced EVs:

Before extracting EVs for functional studies, the morphological condition of the cultivated cells should be assessed. For gaining the most reliable information, this should be carried out by using TEM. If this approach is not available, we recommend using CLSM and staining the specimen for apoptotic markers. The assessment should happen in regular intervals (we used 0 hours – 24 hours – 48 hours – 72 hours), and, most importantly, at the planned EV extraction time. This way, conclusions about the mother cells' state and therefore the validity of the isolated EVs can be drawn.

4.1.3 Examination of the production of EVs over time regarding the number of produced vesicles and the fraction of different EV classes in comparison

Microvesicles

Our results show that MV production increased the longer AoEnd cells were subjected to serum starvation and TNF-α stimulation. This was clear by simply observing the high-resolution SEM images, but we also corroborated this finding by a statistical analysis of the SEM images. The increase of MV-producing cells was roughly linear to the hours of cultivation:

0 hours of serum starvation – 2,4%; 24 hours – 12,5%; 48 hours – 32%.

0 hours of serum starvation and additional TNF-α stimulation – 2,4%; 24 hours – 23,9%, 48 hours – 41,7%.

As evident through the calculated percentages, TNF-α stimulation seemed to be the deciding factor in generating the highest number of MVs. Serum starvation did increase MV production as well, but clearly stimulated the cells less than serum starvation with additional TNF-α stimulation. These results agree with the observation of the research group of Jimenez et al., who proved that treatment with TNF-α at a relatively low concentration (10 ng TNF-α /mL medium – we used 50 ng/ml) achieved significant activation of endothelial cells and formation of endothelial MVs in vitro [121]. This approach has since been used in several studies to characterize the generation and content of EMVs [122, 123].

Apoptotic bodies

During the first 24 hours of cultivation, there were virtually no apoptotic bodies to be found. Their number only began to rise after about 48 hours of cultivation, which we took as a sign that the cells started to undergo apoptosis (see 4.1.2). The fraction of apoptotic bodies then also started to overtake the other EV fractions. This observation is corroborated by Paone et al. and Atkin-Smith et al. who state that “although apoptotic cells can generate MVs, apoptotic bodies represent the major type of EV released during apoptosis” [122, 124].

4.1.4 Generating EVs high in quantity and quality

With this thesis, we wanted to provide recommendations on how to generate EVs with a high quantity and quality for further functional studies.

Quantity

Our results show that the quantity of EVs in the medium rises roughly linear with the time that cells spend in cultivation under serum starvation. A significant

stimulant for high EV production was the application of TNF-α additionally to serum starvation.

Quality

However, we could also establish that after 48 hours of cultivation under serum starvation, MyEnd cells began to deteriorate and go through apoptosis, which assumedly negatively influenced the quality of their produced EVs.

We therefore recommend the following:
To generate as many EVs as possible, the cells should be cultivated in a serum-free medium and additionally be stimulated with TNF-α. We can recommend a stimulation with 50 ng/ml TNF-α to see significant results, however as afore mentioned, other authors also work with a relatively low concentration such as 10 ng/mL [121].
To make sure that the EVs are furthermore of good quality, the extraction point for EVs should not be any later than 48 hours under serum starvation, preferably earlier. To generate as many EVs as possible, the best approach should not be to cultivate cells for a longer amount of time, but to cultivate more cells simultaneously.
However, should our recommended morphological analysis of the mother cells not show any abnormalities after 48 hours (like we observed with AoEnd cells), the extraction could happen at a later point.

The second aim of this thesis was to provide a detailed ultrastructural analysis of the biogenesis and release of endothelial EVs using light and electron microscopy.
Furthermore, we intended to present if and how the EV production and composition changes in cells that are cultivated under inflammatory conditions. Based on the results of these tests, more conclusions about the role of EVs in inflammatory diseases such as atherosclerosis can be drawn.

4.2 Ultrastructural analysis of the biogenesis and release of endothelial EVs

4.2.1 Analysis of MV and exosome biogenesis by endothelial cells cultivated under serum starvation and TNF-α stimulation

Our results entail a detailed ultrastructural analysis of the biogenesis and release of endothelial EVs using light and electron microscopy. Our aim was to depict every single step of EV biogenesis that is described in the literature.

MV biogenesis

Using different microscopic approaches, we were able to depict every described step of MV biogenesis – the direct outward budding of the plasma membrane, the subsequent development of a vesicle, the formation of a vesicle neck and finally, the scission of the plasma membrane [16].

There were two interesting finds:
Firstly, we tried to answer the question whether MVs were released evenly across the cell surface or if there were specific, preferred locations for MV release. In our analysis, we could observe the process of MV biogenesis all over the cells' surface. Regardless of the cell line (MyEnd cells / AoEnd cells) or the stage of cultivation, no preferred location of release could be detected. Pollet et al. stated in a 2018 published review that there is only few reliable data in the literature, with conflicting information [123]: Some studies show that MVs exhibit a similar lipid composition to the plasma membrane, while others show a very specific lipid enrichment or depletion, leading to the suggestion that MVs can indeed shed from specific plasma membrane locations [123, 125]. The discrepancies between results, so Pollet et al., could be related to the cell origin and the pathophysiological context, but also to the methods of MV isolation, purification and characterization [123].

Furthermore, Colombo et al. analysed whether the quantity of released EVs and their respective protein composition was influenced by cell polarity – a trait endothelial cells possess too [126, 127]. They could show that there was indeed

a significant “asymmetry in the number and [biochemical] composition of EVs produced and released from the apical membrane of epithelial cells as compared to the basolateral membrane” [127]. This was linked to the “polarized distribution of two phosphoinositide species between the two cell surfaces” [127]. It was not possible for us to corroborate or contradict this finding during our study, as due to the technical preparation transverse sections were cut and analysis was restricted to the apical cell side. Therefore, further studies are needed to investigate this topic.

Secondly, we investigated whether EV secretion was a homogenous process in the cell population. We first analysed the images – especially informative were overview images with a low magnification factor, captured with CLSM and SEM. It was clear that regardless of the time cultivated under starvation or additional TNF-α stimulation, there was always a significant fraction of cells that did not produce any MVs (or exosomes) at all. To provide further reliable data, we conducted a statistical analysis of the inactive cells using SEM images. The exact percentage of these cells in relation to cultivation time and respective stimulus was the following:

> 0 hours of serum starvation – 97,7%; 24 hours – 87,5%; 48 hours – 68%.
>
> 0 hours of serum starvation and additional TNF-α stimulation – 97,7%; 24 hours – 76,1%; 48 hours – 58,3%.

It is evident that the number of inactive cells decreased with cultivation time under serum starvation and especially TNF-α stimulation. However, at all times, more than half of the evaluated cells did not produce MVs.

At the same time, there were also some cells producing a lot more MVs than the average. To summarise, the production of MVs was a highly heterogeneous process in the cell population, even though all cells stemmed from the same cell line and had received the exact same treatment. Ji et al. addressed the same observation in their 2019 publication: by conducting multiplexed single-cell profiling, they revealed there is a “complex heterogeneity underlying EV

secretion” [128]. Ji et al. found that not all cells were able to secrete EVs; but at the same time, a very small number of cells could secrete ~10 times more than the average secretion – indicating the presence of “super EV secretors” within the cell population [128]. As described, we can corroborate this finding with our results – EV secretion is dominated by certain cell subgroups within the population. What exactly defines this subgroup is yet to be determined. An appropriate way to research this could be to conduct single cell analysis and RNA profiling of “super EV secretors” and non-secreting cells and compare them. An understanding of this difference would be very useful regarding functional studies of EVs. Based on those results, it could be possible to isolate and cultivate only “super EV secretors” and therefore make EV generation much more efficient.

Exosome biogenesis

Using TEM, we were able to depict the following steps of exosome biogenesis: Endocytosis – the beginning of the endosomal pathway, leading to the formation of early endosomes, and their maturation to MVBs due to the generation of ILVs by inward invagination of the MVB membrane [35]. During the last steps of exosome biogenesis, MVBs travel to the surface, fuse with the plasma membrane and release the ILVs into the extracellular environment as exosomes (described and pictured in Akers et al., 2013 [16]). However, as we screened the TEM-sections for morphological correlates, we discovered a striking occurrence. We did not find any morphological evidence of the MVBs' direct fusion with the plasma membrane, instead we found morphological evidence that in serum-starved MyEnd cells, MVBs were incorporated into a new distinct cellular compartment first. There, the MVB membrane dissolved and the exosomes were released within this compartment. The content of the compartments was inhomogeneous and consisted of the former MVBs – some still possessing their endosomal membrane – and the ILVs within as well as various other particles. The most striking observation was that the fraction of the cell membrane at the apical end of this compartment facing the extracellular compartment did not show the typical continuous endothelium, but instead consisted of fenestrated

endothelium. In an “en face” view, its characteristic properties were clearly observable: 60–80 nm diameter transcellular pores spanned by fenestral diaphragms (FDs). In some sections, we could identify the afore-described compartments in the extracellular department – lacking the apical membrane. This might therefore possibly depict the last step of exosome release.

To our knowledge, this phenomenon has not yet been described. In general, there is still a knowledge gap concerning the exact mechanisms of MVB fusion with the plasma membrane. This is partly due to “the lack of methods that can monitor direct, real-time […] MVB biogenesis and MVB–PM fusion. Instead, indirect, post-secretion-based types of examination are typically used, […] [which] are not well suited to study factors that influence the dynamics of secretion” [129].

It is known that the subdivision of a cell into separate compartments enables it to create specialized environments for specific functions. The compartments allow the existence of different environments within a single cell, each for instance with its own pH, ionic composition or distinct physical characteristics and proportions [130]. This permits the cell to carry out specific functions more efficiently than if they were all in the same environment [130]. It is therefore of great interest to further study the specific function of this new cell compartment regarding its role in exosome biogenesis.

4.2.2 Analysis of the influence of inflammatory stimulus TNF-α on the expression of cell surface proteins and their possible transfer by EVs

It is known that inflammation – particularly vascular inflammatory processes – plays an essential role in CVD [131]. It was the aim of this thesis to create such inflammatory, pathological conditions during cell cultivation and then study the EVs derived from this environment. Of particular interest was the question whether TNF-α stimulated endothelial cells would express certain adhesion molecules (which are required for the recruitment of inflammatory cells to the

vessel wall). If so, we aimed to study whether these molecules could be transferred to other target cells by MVs and exosomes.

We chose the inflammatory cytokine TNF-α as a stimulant, because its role in endothelial dysfunction and CVDs such as acute myocardial infarction, chronic heart failure or atherosclerosis is well appreciated [132]. Kleinbongard et al. describe that TNF-α is crucially involved in the pathogenesis and progression of atherosclerosis as it can alter endothelial and vascular smooth muscle cell function as well as endothelial cell–blood cell interaction [133]. TNF-α, amongst other inflammatory cytokines, activates endothelial cells and causes them to express the adhesion molecules VCAM-1 and ICAM-1 [132]. They facilitate the adhesion of circulating leukocytes to the endothelium, which presents one of the first steps in the initiation of atherosclerosis [134]. Another important adhesion molecule with the ability of mediating T-lymphocyte and monocyte adhesion to the endothelium is CD44 [103].

We therefore tested the expression of those three adhesion molecules on the cell surface after stimulation with TNF-α. This was done by analysing confluent AoEnd cells using WGATxRed-X and DAPI staining using CLSM. Expression of the respective molecules was shown as a green fluorescence.

Our results show that there was no substantial expression of ICAM-1 or VCAM-1 after 24h and 48h of cultivation under serum starvation and TNF-α stimulation. This was an unexpected outcome and we assume that these results could also be due to a malfunctioned staining, faulty antibodies or other errors in the experiment. For further clarity on this, the experiments must be repeated. However, after 8 and 24 hours of stimulation with TNF-α, we could observe an abundant expression of CD44 on the surface of the AoEnd cells. A repetition of the test with the exact same results led us to the conclusion that TNF-α stimulation leads to the upregulation of CD44 on AoEnd cells in vitro.

We then worked on the question whether MVs and exosomes could mediate the transfer of CD44 to other endothelial cells. Rautou et al. has already demonstrated that MVs isolated from human atherosclerotic plaques can transfer

ICAM-1 to endothelial cells to recruit inflammatory cells [135]. They conclude that this might be one way that plaque MVs promote atherosclerotic plaque progression [135]. We turned to immunoelectron microscopy to analyse whether CD44 was transferred from the TNF-α stimulated AoEnd cells to their produced MVs and/or exosomes. To visualize CD44 at the plasma membrane, we used pre-embedding Immunoperoxidase (DAB) staining with anti-CD44 as the primary antibody. As expected, all AoEnd cells showed an abundance of CD44 – visualized as dark electron-dense precipitates in the TEM images – evenly all over their surface. Furthermore, we could observe that both MVs and exosomes also showed the DAB staining on their plasma membrane. This demonstrates that in vitro, CD44 is indeed incorporated into the MVs and exosomes by serum starved, TNF-α stimulated AoEnd cells. We concluded that, similarly as already described for ICAM-1 [135], the transfer of CD44 from endothelial cells to target cells can be EV-mediated. The target cells can therefore potentially be modulated in their cell functions and phenotype. Our results therefore describe a novel mechanism by which MVs contribute to the development and progression of atherosclerotic disease.

5. Summary / Zusammenfassung

Extracellular vesicle (EV)-mediated intercellular communication through exosomes, microvesicles (MVs) and apoptotic bodies has been shown to be implicated in various physiological as well as pathological processes such as the development and progression of atherosclerosis. While the cellular machinery controlling EV formation and composition has been studied extensively, little is known about the underlying morphological processes. This study focuses on a detailed ultrastructural analysis of the different steps of EV formation and release in Myocardial Endothelial (MyEnd) and Aortic Endothelial (AoEnd) cells cultured under serum starvation and inflammatory stimulation with TNF-α. Detailed morphological analyses were conducted applying and comparing different high-resolution light and electron microscopic methods. In this study, we could depict all steps of MV biogenesis named in literature. However, during the study of exosome biogenesis, we discovered a yet undescribed process: Instead of a direct fusion with the plasma membrane, multivesicular bodies were incorporated into a new distinct cellular compartment bound by fenestrated endothelium first. This may present a novel step in exosome biogenesis and warrants further study. Regarding the conditions of cell cultivation, we observed that the commonly used serum starvation causes MyEnd cells, but not AoEnd cells, to enter apoptosis after 48 hours. When preparing functional EV studies, we therefore recommend assessing the morphological condition of the serum-starved cells at different cultivation points first. When evaluating MV production, a statistical analysis showed that the more time AoEnd cells spent in cultivation under serum starvation, the higher the percentage of MV producing cells. However, additional TNF-α stimulation induced a significantly higher MV production than serum starvation alone. Lastly, our results show that TNF-α stimulation of AoEnd cells in vitro leads to the upregulation of CD44, an adhesion molecule critical in the early stages of atherosclerosis. CD44 was then depicted on the surface of generated MVs and exosomes. We conclude that under inflammatory conditions, EVs can mediate the transfer of CD44 from endothelial cells to target cells. This could be a novel mechanism by which MVs contribute to the development and progression of atherosclerotic disease and should be clarified by further studies.

Extrazelluläre Vesikel (EV), darunter Exosomen, Mikrovesikel (MV) und apoptotische Körperchen, werden von fast allen Zellen des Körpers freigesetzt, transportieren zellspezifische Informationen und sind von großer Bedeutung in der Zell-Zell-Kommunikation. Sie spielen eine zentrale Rolle in verschiedensten physiologischen sowie pathologischen Vorgängen, wie etwa der Atherosklerose. Während die zellulären Mechanismen hinter der Entstehung und Komposition der EV bereits intensiv erforscht wurden, ist noch wenig über die zugrundeliegenden morphologischen Prozesse bekannt. Diese Arbeit präsentiert eine detaillierte ultrastrukturelle Analyse der Bildung und Freisetzung von EV in myokardialen (MyEnd) und aortalen Endothelzellen (AoEnd), die unter Serumentzug sowie inflammatorischer Stimulation mit TNF-α kultiviert wurden. Dazu wendeten wir verschiedene hochauflösende licht- und elektronenmikroskopische Techniken an. Wir konnten alle in der Literatur beschriebenen Schritte der MV-Biogenese darstellen. Bei der Untersuchung der exosomalen Biogenese entdeckten wir jedoch einen bisher unbekannten Prozess: Anstelle einer direkten Fusion der multivesikulären Körperchen mit der Plasmamembran, wurden diese zunächst in ein neues, von fenestriertem Endothel begrenztes, zelluläres Kompartiment integriert. Ferner stellten wir fest, dass der häufig durchgeführte Serumentzug während der Kultivierung bei MyEnd- – allerdings nicht AoEnd- – Zellen nach 48 Stunden zur Apoptose führte. Daher empfehlen wir, bei funktionellen Studien von EV zunächst eine morphologische Untersuchung der unter Serumentzug kultivierten Zellen zu verschiedenen Zeitpunkten durchzuführen. Eine statistische Analyse der MV-Produktion zeigte, dass die Zellen umso mehr MV produzierten, je länger sie sich unter Serumentzug befanden. Jedoch induzierte eine zusätzliche Stimulation mit TNF-α eine signifikant höhere MV-Produktion als der alleinige Serumentzug. Wir konnten zeigen, dass eine TNF-α Stimulation von AoEnd Zellen in vitro zu einer vermehrten Expression von CD44 führte – einem vor allem in der Frühphase der Atherosklerose bedeutendem Adhäsionsmolekül. CD44 konnte ebenso auf der Oberfläche von produzierten MV und Exosomen nachgewiesen werden. Wir schließen daraus, dass MV unter inflammatorischen Bedingungen den Transfer von CD44 von Endothelzellen zu Zielzellen vermitteln und so zur Entstehung und Progression von Atherosklerose beitragen können.

6. References

1. https://www.destatis.de/DE/Themen/Gesellschaft-Umwelt/Gesundheit/Todesursachen/todesfaelle.html.

2. https://www.destatis.de/DE/Themen/Gesellschaft-Umwelt/Gesundheit/Krankheitskosten/Tabellen/krankheitsklassen-alter.html.

3. Lusis, A.J., *Atherosclerosis.* Nature, 2000. **407**(6801): p. 233-41.

4. Libby, P., P.M. Ridker, and A. Maseri, *Inflammation and atherosclerosis.* Circulation, 2002. **105**(9): p. 1135-43.

5. Goligorsky, M.S., *Endothelial cell dysfunction and nitric oxide synthase.* Kidney Int, 2000. **58**(3): p. 1360-76.

6. Chistiakov, D.A., A.N. Orekhov, and Y.V. Bobryshev, *Endothelial Barrier and Its Abnormalities in Cardiovascular Disease.* Front Physiol, 2015. **6**: p. 365.

7. Kawashima, S. and M. Yokoyama, *Dysfunction of endothelial nitric oxide synthase and atherosclerosis.* Arterioscler Thromb Vasc Biol, 2004. **24**(6): p. 998-1005.

8. Cines, D.B., et al., *Endothelial cells in physiology and in the pathophysiology of vascular disorders.* Blood, 1998. **91**(10): p. 3527-61.

9. BioRender.com, https://app.biorender.com.

10. Nguyen, D.B., et al., *Characterization of Microvesicles Released from Human Red Blood Cells.* Cell Physiol Biochem, 2016. **38**(3): p. 1085-99.

11. Andre, F., et al., *Malignant effusions and immunogenic tumour-derived exosomes.* Lancet, 2002. **360**(9329): p. 295-305.

12. Keller, S., et al., *CD24 is a marker of exosomes secreted into urine and amniotic fluid.* Kidney International, 2007. **72**(9): p. 1095-1102.

13. Mrvar-Brecko, A., et al., *Isolated microvesicles from peripheral blood and body fluids as observed by scanning electron microscope.* Blood Cells Mol Dis, 2010. **44**(4): p. 307-12.

14. Turturici, G., et al., *Extracellular membrane vesicles as a mechanism of cell-to-cell communication: advantages and disadvantages.* Am J Physiol Cell Physiol, 2014. **306**(7): p. C621-33.

15. Jansen, F., G. Nickenig, and N. Werner, *Extracellular Vesicles in Cardiovascular Disease: Potential Applications in Diagnosis, Prognosis, and Epidemiology.* Circ Res, 2017. **120**(10): p. 1649-1657.

16. Akers, J.C., et al., *Biogenesis of extracellular vesicles (EV): exosomes, microvesicles, retrovirus-like vesicles, and apoptotic bodies.* J Neurooncol, 2013. **113**(1): p. 1-11.

17. Gyorgy, B., et al., *Membrane vesicles, current state-of-the-art: emerging role of extracellular vesicles.* Cell Mol Life Sci, 2011. **68**(16): p. 2667-88.

18. Amabile, N., et al., *Microparticles: key protagonists in cardiovascular disorders.* Semin Thromb Hemost, 2010. **36**(8): p. 907-16.

19. Fleury, A., M.C. Martinez, and S. Le Lay, *Extracellular vesicles as therapeutic tools in cardiovascular diseases.* Front Immunol, 2014. **5**: p. 370.

20. Amabile, N., et al., *Association of circulating endothelial microparticles with cardiometabolic risk factors in the Framingham Heart Study.* Eur Heart J, 2014. **35**(42): p. 2972-9.

21. Konkoth, A., et al., *Multifaceted role of extracellular vesicles in atherosclerosis.* Atherosclerosis, 2021. **319**: p. 121-131.

22. Deng, W., et al., *Extracellular vesicles in atherosclerosis.* Clin Chim Acta, 2019. **495**: p. 109-117.

23. Peng, M., X. Liu, and G. Xu, *Extracellular Vesicles as Messengers in Atherosclerosis.* J Cardiovasc Transl Res, 2020. **13**(2): p. 121-130.

24. Rautou, P.E., et al., *Microparticles, vascular function, and atherothrombosis.* Circ Res, 2011. **109**(5): p. 593-606.

25. Esposito, K., et al., *Endothelial microparticles correlate with endothelial dysfunction in obese women.* J Clin Endocrinol Metab, 2006. **91**(9): p. 3676-9.

26. Boulanger, C.M., et al., *Extracellular vesicles in coronary artery disease.* Nat Rev Cardiol, 2017. **14**(5): p. 259-272.

27. Tsuda, K., *Plasma Homocysteine Levels and Endothelial Dysfunction in Cerebro- and Cardiovascular Diseases in the Metabolic Syndrome.* American Journal of Hypertension, 2015. **28**(12): p. 1489-1489.

28. Zhan, R., et al., *Heat shock protein 70 is secreted from endothelial cells by a non-classical pathway involving exosomes.* Biochem Biophys Res Commun, 2009. **387**(2): p. 229-33.

29. Zakharova, L., M. Svetlova, and A.F. Fomina, *T cell exosomes induce cholesterol accumulation in human monocytes via phosphatidylserine receptor.* J Cell Physiol, 2007. **212**(1): p. 174-81.

30. Gao, W., et al., *Exosomes derived from mature dendritic cells increase endothelial inflammation and atherosclerosis via membrane TNF-alpha mediated NF-kappaB pathway.* J Cell Mol Med, 2016. **20**(12): p. 2318-2327.

31. Zaborowski, M.P., et al., *Extracellular Vesicles: Composition, Biological Relevance, and Methods of Study.* Bioscience, 2015. **65**(8): p. 783-797.

32. Heijnen, H.F., et al., *Activated platelets release two types of membrane vesicles: microvesicles by surface shedding and exosomes derived from exocytosis of multivesicular bodies and alpha-granules.* Blood, 1999. **94**(11): p. 3791-9.

33. Borges, F.T., L.A. Reis, and N. Schor, *Extracellular vesicles: structure, function, and potential clinical uses in renal diseases.* Braz J Med Biol Res, 2013. **46**(10): p. 824-30.

34. Leroyer, A.S., et al., *Endothelial-derived microparticles: Biological conveyors at the crossroad of inflammation, thrombosis and angiogenesis.* Thromb Haemost, 2010. **104**(3): p. 456-63.

35. Bang, C. and T. Thum, *Exosomes: new players in cell-cell communication.* Int J Biochem Cell Biol, 2012. **44**(11): p. 2060-4.

36. Lee, Y., S. El Andaloussi, and M.J. Wood, *Exosomes and microvesicles: extracellular vesicles for genetic information transfer and gene therapy.* Hum Mol Genet, 2012. **21**(R1): p. R125-34.

37. Vlassov, A.V., et al., *Exosomes: current knowledge of their composition, biological functions, and diagnostic and therapeutic potentials.* Biochim Biophys Acta, 2012. **1820**(7): p. 940-8.

38. Conde-Vancells, J., et al., *Characterization and comprehensive proteome profiling of exosomes secreted by hepatocytes.* J Proteome Res, 2008. **7**(12): p. 5157-66.

39. Wubbolts, R., et al., *Proteomic and biochemical analyses of human B cell-derived exosomes. Potential implications for their function and multivesicular body formation.* J Biol Chem, 2003. **278**(13): p. 10963-72.

40. Tricarico, C., J. Clancy, and C. D'Souza-Schorey, *Biology and biogenesis of shed microvesicles.* Small GTPases, 2017. **8**(4): p. 220-232.

41. van der Pol, E., et al., *Classification, functions, and clinical relevance of extracellular vesicles.* Pharmacol Rev, 2012. **64**(3): p. 676-705.

42. Chargaff, E. and R. West, *The biological significance of the thromboplastic protein of blood.* J Biol Chem, 1946. **166**(1): p. 189-97.

43. Wolf, P., *The nature and significance of platelet products in human plasma.* Br J Haematol, 1967. **13**(3): p. 269-88.

44. Cocucci, E. and J. Meldolesi, *Ectosomes and exosomes: shedding the confusion between extracellular vesicles.* Trends Cell Biol, 2015. **25**(6): p. 364-72.

45. Pap, E., et al., *Highlights of a new type of intercellular communication: microvesicle-based information transfer.* Inflamm Res, 2009. **58**(1): p. 1-8.

46. Muralidharan-Chari, V., et al., *Microvesicles: mediators of extracellular communication during cancer progression.* J Cell Sci, 2010. **123**(Pt 10): p. 1603-11.

47. Zwaal, R.F. and A.J. Schroit, *Pathophysiologic implications of membrane phospholipid asymmetry in blood cells.* Blood, 1997. **89**(4): p. 1121-32.

48. Boulanger, C.M., N. Amabile, and A. Tedgui, *Circulating microparticles: a potential prognostic marker for atherosclerotic vascular disease.* Hypertension, 2006. **48**(2): p. 180-6.

49. Cocucci, E., G. Racchetti, and J. Meldolesi, *Shedding microvesicles: artefacts no more.* Trends Cell Biol, 2009. **19**(2): p. 43-51.

50. Abels, E.R. and X.O. Breakefield, *Introduction to Extracellular Vesicles: Biogenesis, RNA Cargo Selection, Content, Release, and Uptake.* Cell Mol Neurobiol, 2016. **36**(3): p. 301-12.

51. Sun, L., et al., *Serum deprivation elevates the levels of microvesicles with different size distributions and selectively enriched proteins in human myeloma cells in vitro.* Acta Pharmacol Sin, 2014. **35**(3): p. 381-93.

52. Tetta, C., et al., *Extracellular vesicles as an emerging mechanism of cell-to-cell communication.* Endocrine, 2013. **44**(1): p. 11-9.

53. Combes, V., et al., *In vitro generation of endothelial microparticles and possible prothrombotic activity in patients with lupus anticoagulant.* J Clin Invest, 1999. **104**(1): p. 93-102.

54. Chironi, G.N., et al., *Endothelial microparticles in diseases.* Cell Tissue Res, 2009. **335**(1): p. 143-51.

55. Sapet, C., et al., *Thrombin-induced endothelial microparticle generation: identification of a novel pathway involving ROCK-II activation by caspase-2.* Blood, 2006. **108**(6): p. 1868-76.

56. Simak, J., K. Holada, and J.G. Vostal, *Release of annexin V-binding membrane microparticles from cultured human umbilical vein endothelial cells after treatment with camptothecin.* BMC Cell Biol, 2002. **3**: p. 11.

57. Wang, J.M., et al., *C-Reactive protein-induced endothelial microparticle generation in HUVECs is related to BH4-dependent NO formation.* J Vasc Res, 2007. **44**(3): p. 241-8.

58. Vion, A.C., et al., *Shear stress regulates endothelial microparticle release.* Circ Res, 2013. **112**(10): p. 1323-33.

59. MacKenzie, A., et al., *Rapid secretion of interleukin-1beta by microvesicle shedding.* Immunity, 2001. **15**(5): p. 825-35.

60. Obregon, C., et al., *Exovesicles from human activated dendritic cells fuse with resting dendritic cells, allowing them to present alloantigens.* Am J Pathol, 2006. **169**(6): p. 2127-36.

61. Trams, E.G., et al., *Exfoliation of membrane ecto-enzymes in the form of micro-vesicles.* Biochim Biophys Acta, 1981. **645**(1): p. 63-70.

62. Harding, C., J. Heuser, and P. Stahl, *Receptor-mediated endocytosis of transferrin and recycling of the transferrin receptor in rat reticulocytes.* J Cell Biol, 1983. **97**(2): p. 329-39.

63. Pan, B.T. and R.M. Johnstone, *Fate of the transferrin receptor during maturation of sheep reticulocytes in vitro: selective externalization of the receptor.* Cell, 1983. **33**(3): p. 967-78.

64. Johnstone, R.M., et al., *Vesicle formation during reticulocyte maturation. Association of plasma membrane activities with released vesicles (exosomes).* J Biol Chem, 1987. **262**(19): p. 9412-20.

65. Pan, B.T., et al., *Electron microscopic evidence for externalization of the transferrin receptor in vesicular form in sheep reticulocytes.* J Cell Biol, 1985. **101**(3): p. 942-8.

66. Johnstone, R.M., *Revisiting the road to the discovery of exosomes.* Blood Cells Mol Dis, 2005. **34**(3): p. 214-9.

67. Kourembanas, S., *Exosomes: vehicles of intercellular signaling, biomarkers, and vectors of cell therapy.* Annu Rev Physiol, 2015. **77**: p. 13-27.

68. Sotelo, J.R. and K.R. Porter, *An electron microscope study of the rat ovum.* J Biophys Biochem Cytol, 1959. **5**(2): p. 327-42.

69. Raiborg, C. and H. Stenmark, *The ESCRT machinery in endosomal sorting of ubiquitylated membrane proteins.* Nature, 2009. **458**(7237): p. 445-52.

70. Minciacchi, V.R., M.R. Freeman, and D. Di Vizio, *Extracellular vesicles in cancer: exosomes, microvesicles and the emerging role of large oncosomes.* Semin Cell Dev Biol, 2015. **40**: p. 41-51.

71. Kleijmeer, M., et al., *Reorganization of multivesicular bodies regulates MHC class II antigen presentation by dendritic cells.* J Cell Biol, 2001. **155**(1): p. 53-63.

72. Wollert, T. and J.H. Hurley, *Molecular mechanism of multivesicular body biogenesis by ESCRT complexes.* Nature, 2010. **464**(7290): p. 864-9.

73. Babst, M., *MVB vesicle formation: ESCRT-dependent, ESCRT-independent and everything in between.* Curr Opin Cell Biol, 2011. **23**(4): p. 452-7.

74. Schmidt, O. and D. Teis, *The ESCRT machinery.* Curr Biol, 2012. **22**(4): p. R116-20.

75. Colombo, M., G. Raposo, and C. Thery, *Biogenesis, secretion, and intercellular interactions of exosomes and other extracellular vesicles.* Annu Rev Cell Dev Biol, 2014. **30**: p. 255-89.

76. Stuffers, S., et al., *Multivesicular endosome biogenesis in the absence of ESCRTs.* Traffic, 2009. **10**(7): p. 925-37.

77. Trajkovic, K., et al., *Ceramide triggers budding of exosome vesicles into multivesicular endosomes.* Science, 2008. **319**(5867): p. 1244-7.

78. Ghossoub, R., et al., *Syntenin-ALIX exosome biogenesis and budding into multivesicular bodies are controlled by ARF6 and PLD2.* Nat Commun, 2014. **5**: p. 3477.

79. Thery, C., M. Ostrowski, and E. Segura, *Membrane vesicles as conveyors of immune responses.* Nat Rev Immunol, 2009. **9**(8): p. 581-93.

80. Blanchard, N., et al., *TCR activation of human T cells induces the production of exosomes bearing the TCR/CD3/zeta complex.* J Immunol, 2002. **168**(7): p. 3235-41.

81. Raposo, G., et al., *Accumulation of major histocompatibility complex class II molecules in mast cell secretory granules and their release upon degranulation.* Mol Biol Cell, 1997. **8**(12): p. 2631-45.

82. Arita, S., et al., *B cell activation regulates exosomal HLA production.* Eur J Immunol, 2008. **38**(5): p. 1423-34.

83. Raposo, G., et al., *B lymphocytes secrete antigen-presenting vesicles.* J Exp Med, 1996. **183**(3): p. 1161-72.

84. Zitvogel, L., et al., *Eradication of established murine tumors using a novel cell-free vaccine: dendritic cell-derived exosomes.* Nat Med, 1998. **4**(5): p. 594-600.

85. Bhatnagar, S., et al., *Exosomes released from macrophages infected with intracellular pathogens stimulate a proinflammatory response in vitro and in vivo.* Blood, 2007. **110**(9): p. 3234-44.

86. Lespagnol, A., et al., *Exosome secretion, including the DNA damage-induced p53-dependent secretory pathway, is severely compromised in TSAP6/Steap3-null mice.* Cell Death Differ, 2008. **15**(11): p. 1723-33.

87. Alonso, R., et al., *Diacylglycerol kinase alpha regulates the secretion of lethal exosomes bearing Fas ligand during activation-induced cell death of T lymphocytes.* J Biol Chem, 2005. **280**(31): p. 28439-50.

88. Golenhofen, N., et al., *Expression and induction of the stress protein alpha-B-crystallin in vascular endothelial cells.* Histochem Cell Biol, 2002. **117**(3): p. 203-9.

89. Joseph Sambrook, E.F.F., Tom Maniatis, *Molecular Cloning: A Laboratory Manual*. 2nd Edition ed. Vol. 3. 1989, Cold Spring Harbor, New York: Cold Spring Harbor Laboratory Press.

90. Reynolds, E.S., *The use of lead citrate at high pH as an electron-opaque stain in electron microscopy.* J Cell Biol, 1963. **17**: p. 208-12.

91. Walton, J., *Lead aspartate, an en bloc contrast stain particularly useful for ultrastructural enzymology.* J Histochem Cytochem, 1979. **27**(10): p. 1337-42.

92. Ellis, E.A. and D.W. Anthony, *A method for removing precipitate from ultrathin sections resulting from glutaraldehyde-osmium tetroxide fixation.* Stain Technol, 1979. **54**(5): p. 282-5.

93. Z´aborszky, L., Heimer, L., *Combinations of tracer techniques, especially HRP and PHA-L, with transmitter identification for correlated light and electron microscopic studies.* Neuroanatomical Tract-Tracing Methods 2, 1989: p. p. 49–96.

94. Fischer, E.R., et al., *Scanning electron microscopy.* Curr Protoc Microbiol, 2012. **Chapter 2**: p. Unit 2B 2.

95. Schindelin, J., et al., *Fiji: an open-source platform for biological-image analysis.* Nat Methods, 2012. **9**(7): p. 676-82.

96. Mettlen, M., et al., *Regulation of Clathrin-Mediated Endocytosis.* Annu Rev Biochem, 2018. **87**: p. 871-896.

97. Hessvik, N.P. and A. Llorente, *Current knowledge on exosome biogenesis and release.* Cell Mol Life Sci, 2018. **75**(2): p. 193-208.

98. Stan, R.V., et al., *The diaphragms of fenestrated endothelia: gatekeepers of vascular permeability and blood composition.* Dev Cell, 2012. **23**(6): p. 1203-18.

99. Stan, R.V., *Structure and function of endothelial caveolae.* Microsc Res Tech, 2002. **57**(5): p. 350-64.

100. Mohieldin, A.M., et al., *Vascular Endothelial Primary Cilia: Mechanosensation and Hypertension.* Curr Hypertens Rev, 2016. **12**(1): p. 57-67.

101. Galkina, E. and K. Ley, *Vascular adhesion molecules in atherosclerosis.* Arterioscler Thromb Vasc Biol, 2007. **27**(11): p. 2292-301.

102. McEver, R.P., *Selectins: initiators of leucocyte adhesion and signalling at the vascular wall.* Cardiovasc Res, 2015. **107**(3): p. 331-9.

103. Cuff, C.A., et al., *The adhesion receptor CD44 promotes atherosclerosis by mediating inflammatory cell recruitment and vascular cell activation.* J Clin Invest, 2001. **108**(7): p. 1031-40.

104. Lim, Y.C., et al., *Culture and detection of primary cilia in endothelial cell models.* Cilia, 2015. **4**: p. 11.

105. Teng, X., F. Li, and C. Lu, *Visualization of materials using the confocal laser scanning microscopy technique.* Chem Soc Rev, 2020.

106. Dürrenberger, M.B., et al., *Visualization of Food Structure by Confocal Laser Scanning Microscopy (CLSM).* Lebensmittel Wissenschaft and Technologie 2000. **34**(1): p. 11-17.

107. Heintzmann, R. and G. Ficz, *Breaking the resolution limit in light microscopy.* Brief Funct Genomic Proteomic, 2006. **5**(4): p. 289-301.

108. Chuo, S.T., J.C. Chien, and C.P. Lai, *Imaging extracellular vesicles: current and emerging methods.* J Biomed Sci, 2018. **25**(1): p. 91.

109. Cizmar, P. and Y. Yuana, *Detection and Characterization of Extracellular Vesicles by Transmission and Cryo-Transmission Electron Microscopy.* Methods Mol Biol, 2017. **1660**: p. 221-232.

110. Noble, J.M., et al., *Direct comparison of optical and electron microscopy methods for structural characterization of extracellular vesicles.* J Struct Biol, 2020. **210**(1): p. 107474.

111. Ana L. De Paul, J.H.M., Juan P. Petiti, Silvina Gutiérrez, Amado A. Quintar, Cristina A. Maldonado and Alicia I. Torres (March 9th 2012). Immunoelectron Microscopy: A Reliable Tool for the Analysis of Cellular Processes, Applications of Immunocytochemistry, Hesam Dehghani, IntechOpen, DOI: 10.5772/33108. Available from: https://www.intechopen.com/books/applications-of-immunocytochemistry/immunoelectron-microscopy-a-reliable-tool-for-the-analysis-of-biological-processes.

112. Choi, H. and J.Y. Mun, *Structural Analysis of Exosomes Using Different Types of Electron Microscopy.* Applied Microscopy, 2017. **47**(3): p. 171-175.

113. Pirkmajer, S. and A.V. Chibalin, *Serum starvation: caveat emptor.* Am J Physiol Cell Physiol, 2011. **301**(2): p. C272-9.

114. Thery, C., et al., *Isolation and characterization of exosomes from cell culture supernatants and biological fluids.* Curr Protoc Cell Biol, 2006. **Chapter 3**: p. Unit 3 22.

115. https://www.miltenyibiotec.com/upload/assets/IM0021617.PDF.

116. https://www.takarabio.com/learning-centers/cell-biology-assays/exosome-isolation-from-cell-culture.

117. Huang, Y., et al., *Serum starvation-induces down-regulation of Bcl-2/Bax confers apoptosis in tongue coating-related cells in vitro.* Mol Med Rep, 2018. **17**(4): p. 5057-5064.

118. Terra, L.F., et al., *Recombinant human prolactin promotes human beta cell survival via inhibition of extrinsic and intrinsic apoptosis pathways.* Diabetologia, 2011. **54**(6): p. 1388-97.

119. Hogg, N., et al., *Apoptosis in vascular endothelial cells caused by serum deprivation, oxidative stress and transforming growth factor-beta.* Endothelium, 1999. **7**(1): p. 35-49.

120. Yanez-Mo, M., et al., *Biological properties of extracellular vesicles and their physiological functions.* J Extracell Vesicles, 2015. **4**: p. 27066.

121. Jimenez, J.J., et al., *Elevated endothelial microparticles in thrombotic thrombocytopenic purpura: findings from brain and renal microvascular cell culture and patients with active disease.* Br J Haematol, 2001. **112**(1): p. 81-90.

122. Paone, S., et al., *Endothelial cell apoptosis and the role of endothelial cell-derived extracellular vesicles in the progression of atherosclerosis.* Cell Mol Life Sci, 2019. **76**(6): p. 1093-1106.

123. Pollet, H., et al., *Plasma Membrane Lipid Domains as Platforms for Vesicle Biogenesis and Shedding?* Biomolecules, 2018. **8**(3).

124. Atkin-Smith, G.K. and I.K.H. Poon, *Disassembly of the Dying: Mechanisms and Functions.* Trends Cell Biol, 2017. **27**(2): p. 151-162.

125. Haraszti, R.A., et al., *High-resolution proteomic and lipidomic analysis of exosomes and microvesicles from different cell sources.* J Extracell Vesicles, 2016. **5**: p. 32570.

126. Coradini, D., et al., *Adipokines expression and epithelial cell polarity in normal and cancerous breast tissue.* Carcinogenesis, 2020. **41**(10): p. 1402-1408.

127. Colombo, F., et al., *Polarized cells display asymmetric release of extracellular vesicles.* Traffic, 2020.

128. Ji, Y., et al., *Multiplexed profiling of single-cell extracellular vesicles secretion.* Proc Natl Acad Sci U S A, 2019. **116**(13): p. 5979-5984.

129. Bebelman, M.P., et al., *Real-time imaging of multivesicular body-plasma membrane fusion to quantify exosome release from single cells.* Nat Protoc, 2020. **15**(1): p. 102-121.

130. https://www.nature.com/scitable/topic/subcellular-compartments-14122679/.

131. Jansen, F., et al., *Endothelial- and Immune Cell-Derived Extracellular Vesicles in the Regulation of Cardiovascular Health and Disease.* JACC Basic Transl Sci, 2017. **2**(6): p. 790-807.

132. Mudau, M., et al., *Endothelial dysfunction: the early predictor of atherosclerosis.* Cardiovasc J Afr, 2012. **23**(4): p. 222-31.

133. Kleinbongard, P., G. Heusch, and R. Schulz, *TNFalpha in atherosclerosis, myocardial ischemia/reperfusion and heart failure.* Pharmacol Ther, 2010. **127**(3): p. 295-314.

134. Libby, P., et al., *Inflammation in atherosclerosis: from pathophysiology to practice.* J Am Coll Cardiol, 2009. **54**(23): p. 2129-38.

135. Rautou, P.E., et al., *Microparticles from human atherosclerotic plaques promote endothelial ICAM-1-dependent monocyte adhesion and transendothelial migration.* Circ Res, 2011. **108**(3): p. 335-43.

Appendix

I List of Abbreviations

°C	degree Celsius
3D	three-dimensional
AB complex	Avidin-biotin complex
AoEnd cell	Aortic Endothelial cell
ATP	Adenosine triphosphate
BSA	bovine serum albumin
CCP	clathrin-coated pit
CCV	clathrin-coated vesicle
CD44	cluster of differentiation 44
CLSM	Confocal Laser Scanning Microscopy
CVD	cardiovascular disease
DAB	3,3′-Diaminobenzidinetetrahydrochloride
DAPI	4′,6-diamidino-2-phenylindole
ddH_2O	double-distilled water
DNA	deoxyribonucleic acid
ESCRT	endosomal sorting complex required for transport
et al.	et alia = and others
EV	extracellular vesicle

FBS	fetal bovine serum
FD	fenestral diaphragm
Fig.	figure
g	gram
HSP70	Heat Shock Protein 70
ICAM-1	intercellular adhesion molecule-1
intraluminal vesicle	ILV
L	liter
LDL	low-density lipoprotein
LPS	lipopolysaccharide
M	Molar
mg	milligram
MHC class II	major histocompatibility complex class II
ml	milliliter
MV	microvesicle
MVBs	multivesicular bodies
MyEnd cell	Myocardial Endothelial cell
ng	nanogram
nm	nanometer
NO	nitric oxide
PB	phosphate buffer

PBS	phosphate buffered saline
PFA	paraformaldehyde
PO	propylene oxide
PS	phosphatidylserine
rER	rough endoplasmatic reticulum
RNA	ribonucleic acid
SBF-SEM	Serial Block Face Scanning Electron Microscopy
SEM	Scanning Electron Microscopy
Tab.	table
TCH	thiocarbohydrazide
TEM	Transmission Electron Microscopy
TNF-α	tumor necrosis factor α
TSB	Tris-saline-buffer
UA	uranyl acetate
VCAM-1	vascular cell adhesion molecule-1
VLDL	very low-density lipoprotein
WGATxRed-X	Wheat Germ Agglutinin, Texas Red-X conjugate
WT C57BL/6 mouse	Wild-Type C57 black 6 (laboratory) mouse
µm	micrometer

II List of Figures

III List of Tables

IV Acknowledgments

An dieser Stelle möchte ich allen Personen meinen großen Dank aussprechen, die mich bei der Anfertigung meiner Dissertation unterstützt haben und ohne deren Mithilfe sie nicht zustande gekommen wäre.

Ich danke zunächst meiner Doktormutter Frau Dr. Nicole Wagner für die tolle Betreuung dieser Dissertation und die Hilfe und Unterstützung sowohl im Labor als auch beim schriftlichen Teil meiner Arbeit. Die zahlreichen Gespräche auf professioneller und persönlicher Ebene (meist bei einem gemeinsamen Kaffee) werden mir immer als bereichernder und konstruktiver Austausch in Erinnerung bleiben. Danke für die gute Zusammenarbeit, es hat mir Spaß gemacht!

Des Weiteren möchte ich mich bei Herrn Professor Dr. Süleyman Ergün, Vorstand des Instituts für Anatomie und Zellbiologie, bedanken, der mir die Möglichkeit gegeben hat, diese Arbeit unter seiner Leitung durchzuführen.

Ich bedanke mich außerdem bei Karin Reinfurt-Gehm und Sieglinde Schenk für ihre großartige technische und moralische Unterstützung meiner experimentellen Arbeit im Labor. Ohne Eure Hilfe und Eure langjährige Erfahrung wären die Versuche niemals so gut gelaufen. Vielen lieben Dank!

Ebenfalls ein herzliches Dankeschön an Nadja Höhn, die sich so gut um die Kultivierung der Endothelzellen für meine Arbeit gekümmert hat.

Mein besonderer Dank gilt schließlich meinen lieben Eltern, die mir schon mein ganzes Studium lang unterstützend und liebevoll zur Seite gestanden haben und mir in jeder Lebenslage mit ihrem Rat und ihrer Ruhe weitergeholfen haben. Ihnen ist diese Dissertation gewidmet.

VI List of publications and conference presentations

The data on which the present work is based were presented in a poster session at the 113th Annual Meeting of the Anatomical Society:

Elsner C., Ergün S., Wagner N.: *Ultrastructural analysis of biogenesis and release of endothelial extracellular vesicles*.
Poster presentation as part of the Annual Meeting of the Anatomical Society, Rostock, Germany, 25.09. - 28.09.2018.

Furthermore, the data will be published.
The paper "Biogenesis and release of endothelial extracellular vesicles: morphological aspects" based on the present work has been accepted for publication in Volume 244 of the journal Annals of Anatomy, to be released in October 2022:
Elsner C., Ergün S., Wagner N. (2022): *Biogenesis and release of endothelial extracellular vesicles: morphological aspects.*